STUDY OF COUPLED TRANSPORT AND ITS EFFECT ON DIFFERENT ELECTROCHEMICAL SYSTEMS: IMPLICATIONS IN HIGH TEMPERATURE ENERGY STORAGE BATTERIES AND PROTON EXCHANGE MEMBRANE FUEL CELLS

by

Preethy Parthasarathy

A dissertation submitted to the faculty of
The University of Utah
in partial fulfillment of the requirements for the degree of

Doctor of Philosophy

Department of Materials Science and Engineering

The University of Utah

May 2013

The University of Utah Graduate School

STATEMENT OF DISSERTATION APPROVAL

The dissertation of **Preethy Parthasarathy**

has been approved by the following supervisory committee members:

Anil V. Virkar	, Chair	**10/29/2012** Date Approved
Dinesh K. Shetty	, Member	**10/29/2012** Date Approved
Feng Liu	, Member	**10/29/2012** Date Approved
Jules J. Magda	, Member	**10/29/2012** Date Approved
Florian Solzbacher	, Member	**10/29/2012** Date Approved

and by **Feng Liu**, Chair of the Department of **Materials Science and Engineering**

and by Charles A. Wight, Dean of The Graduate School.

ABSTRACT

Coupled transport is studied on two electrochemical systems: Na-$ZnCl_2$ batteries and Proton Exchange Membrane Fuel Cells (PEMFC). The energy storage system of interest here is based on sodium β"-alumina solid electrolyte (BASE): Na/BASE/$ZnCl_2$. BASE is an excellent Na^+ conductor with a very high conductivity at 300°C. Its high Na^+ ion conductivity and high stability are the principal reasons for its application in electrochemical storage systems. A novel vapor phase process was invented facilitating the fabrication of high strength and moisture/CO_2 resistant BASE. A two-phase composite of alumina+YSZ is formed by sintering and exposed to Na_2O vapor, keeping the activity of Na_2O lower than that in $NaAlO_2$. This prevents the formation of hygroscopic $NaAlO_2$ at the grain boundaries. A thin layer of β"-alumina is formed on the surface upon exposure. Further reaction occurs by transporting Na^+ ions through the formed β"-alumina and a parallel transport of O^{2-} ions through YSZ. This occurs by a coupled transport of Na^+ through β"-alumina and O^{2-} ions through YSZ, thus expediting the process.

The second electrochemical system of interest is PEMFC. The degradation mechanism of catalysts is studied using inexpensive copper particles. The mechanism of growth involves a coupled transport of Cu^{2+} through the aqueous medium and an electron transport through the direct particle-to-particle contact. Effect of applied stress on coarsening of platinum was also investigated. Two platinum wires/foils were immersed in a $PtCl_4$+DMSO (Dimethyl sulfoxide) solution. A tensile load was applied to one wire/foil

and the other one was left load-free. The wire/foil subjected to a tensile load became cathodic with respect to the unstressed wire/foil. Thus, under a tensile stress, the chemical potential of Pt decreases. This result suggests design strategies for core–shell catalysts used in PEMFCs: stable core–shell catalysts for PEMFC with Pt shell should be designed such that the shell is under a tensile stress.

Specific surface energies (γ) of f.c.c. metals as a function of shape and size were investigated using the broken-bond model. γ decreased with increasing particle size and approached asymptotic values beyond an equivalent diameter of ~5 nm. Octahedral-shaped particles were the most stable.

For my Amma, Appa, Akka, Athimber, and Nannu

TABLE OF CONTENTS

LIST OF TABLES

LIST OF FIGURES

ACKNOWLEDGEMENTS

I would like to thank Dr. Anil Virkar for his mentoring, support, enthusiasm, and belief in hard work. The work presented in this dissertation is as much a result of many interesting and instructive discussions with him as it is of hours spent in the lab.

I would also like to thank my thesis advisory committee: Dr. Dinesh Shetty, Dr. Feng Liu, Dr. Jules J. Magda, and Dr. Florian Solzbacher. Their time and effort in guiding my research and being a part of my committee is greatly appreciated.

This work was made possible through the financial support from the U.S. Department of Energy under Grant Number DE-FG02-03ER46086, and the National Science Foundation under Grant Number CBET-0931080, and the Department of Energy-EFRC under Grant Number DE-SC0001061 as a flow through from the University of South Carolina.

I would like to express a special word of thanks to Dr. Neill Weber, who was abundantly helpful and offered invaluable assistance, support, and guidance throughout my Ph.D. research. Thanks to all my friends and colleagues in the research lab and at the University of Utah, both past and present, for their support and friendship.

Finally, I would like to thank my family for their constant support and love. Thank you!

CHAPTER 1

INTRODUCTION

1.1 Sodium β"-Alumina Solid Electrolyte

Sodium β and β"-alumina are known for their excellent conductivity of sodium ions. Both are highly refractory compounds of stoichiometry $Na_2O.11Al_2O_3$ and $Na_2O.\sim6.2\ Al_2O_3$ in the Na_2O-Al_2O_3 system [1]. The crystal structure of Na β-alumina is hexagonal and that of Na β"-alumina is rhombohedral, which can be indexed as hexagonal. Figure 1.1 shows the schematic of 2-block and 3-block structures of β-alumina and β"-alumina, respectively. Crystal structures of β and β"-alumina consist of Al-O spinel blocks, separated by conduction planes perpendicular to the c-axis of the unit cell. Mobility of sodium ions in the conduction plane is very high, whereas the mobility along the c-axis is negligible. In a polycrystalline body, Na^+ ion conduction is isotropic due to its random orientation of grains. At 300°C, resistivity of β is ~15Ωcm and resistivity of β" is ~3Ωcm. Due to the exceptional conductivity of Na^+ ions, Na β"-alumina is used as a solid electrolyte (otherwise known as BASE) in several electrochemical storage devices. Some of the major applications of BASE are in sodium sulfur batteries, Zebra batteries, and alkali-metal thermal-to-electric converters (AMTECs). BASE was first developed by researchers at the Ford Motor Company while conducting a study on energy storage devices for electric vehicles. They developed the concept of a sodium sulfur battery, which consists of sulfur at the positive electrode and

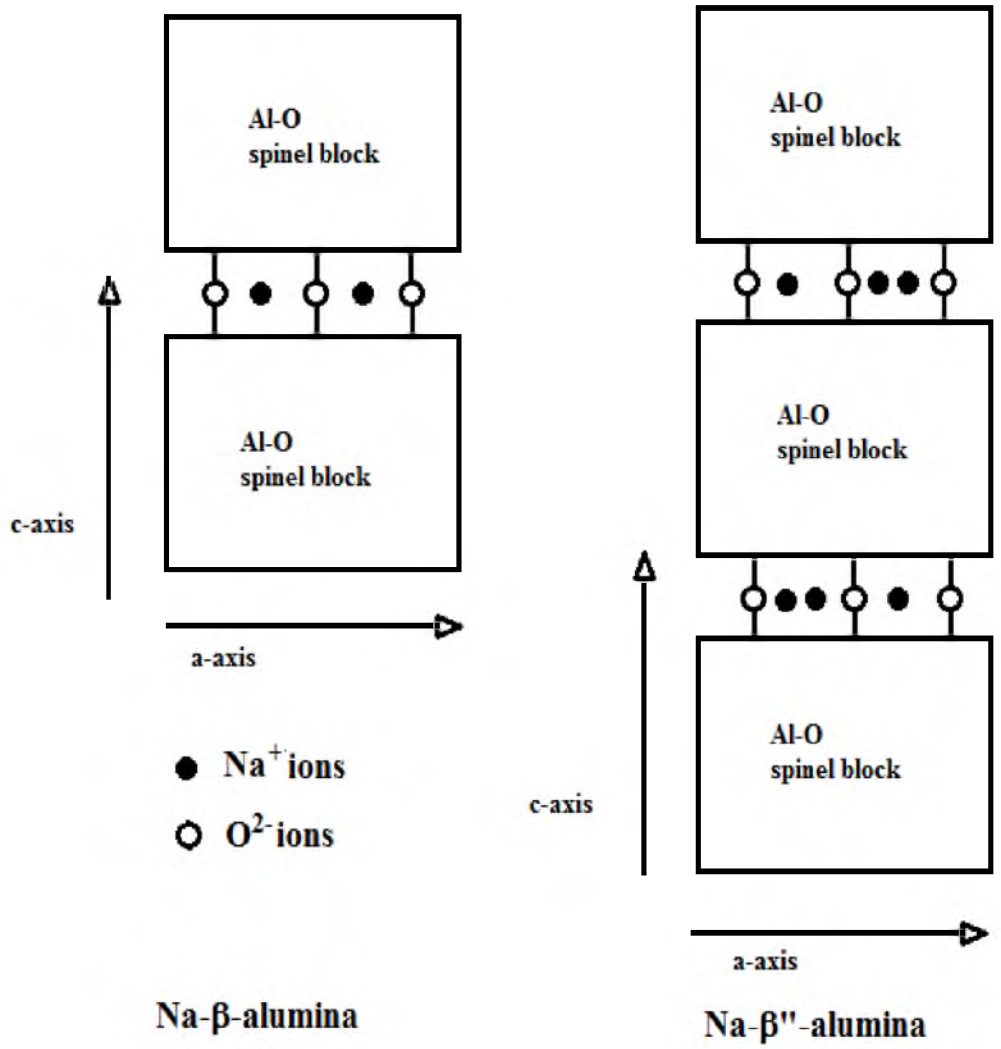

Figure 1.1 Schematic of 2-block and 3-block structures of β and β”-alumina, respectively

sodium at the negative electrode as active materials, and sodium-conducting beta-alumina ceramic as the electrolyte. At 300^{o}C, both electrodes are liquid, which leads to a faster reaction kinetics. While discharging, Na^{+} ions transport through BASE into the sulfur electrode with electrons transporting in the external circuit to form sodium polysulfides. During the charging part of the cycle, Na^{+} ions transport from the sulfur electrode through the BASE to the Na anode, with electrons transporting in the external circuit. The batteries use one end closed BASE tubes, and stainless steel or Ebrite containers with a

protective chromium coating to prevent corrosion induced by sulfur and sodium polysulfides. Several cells are configured in a module with series and parallel connections for optimum performance and reliability. Sodium sulfur batteries are commercialized by NGK Insulators, Ltd., in Japan mainly for stationary applications such as a load leveling, integrated system with a wind generator and DC power source. Several other companies like American Electric Power (AEP) and Xcel Energy started utilizing sodium sulfur batteries for stationary applications. These are no longer used for mobile applications due to the safety issues concerning the accidental reaction between sodium and sulfur in the event of a short circuit, which produces highly corrosive sodium polysulfides.

Another important application of BASE is in ZEBRA batteries (Zeolite Battery Research Africa Project or Zero Emissions Batteries Research Activity) [2]. ZEBRA batteries use sodium as anode and $NiCl_2$ as cathode, the electrolyte/ separator being BASE [3]. The operational temperature of ZEBRA batteries has been chosen in the range of 270 to 350^{o}C. During charging, sodium is ionized. Na^{+} ions conduct through solid electrolyte and electrons through the outer circuit to the higher potential of the anode, where it recombines with the sodium ions. While discharging, sodium ions conduct back through the electrolyte to the cathode and electrons via the outer circuit.

BASE is also used in alkali-metal thermal-to-electric converters (AMTECs). An AMTEC is a highly efficient device with efficiency up to 40% (typical efficiency of thermoelectrics are in the range of 15 – 20%) for directly converting heat to electricity. An AMTEC operates as a thermally regenerative electrochemical cell by expanding sodium through the pressure differential across the (BASE) membrane. It is characterized by high potential efficiencies and no moving parts, which make it a candidate for space

power applications. In this device, sodium is cycled around a closed thermodynamic cycle between two heat reservoirs at different temperatures. It is a sodium concentration cell, which uses BASE as a separator between a high pressure region containing sodium vapor at 600 – 1000^{o}C and a low pressure region containing a condenser for liquid sodium at 120–420^{o}C. BASE electrolytes have also been used in some molten-carbonate fuel cells, as well as other liquid electrode/solid electrolyte fuel cell designs. BASE has demonstrated outstanding stability under high pressure, high temperature, or corrosive environments far superior than other solid electrolytes currently available, making it an ideal candidate for electrochemical storage devices.

BASE is conventionally processed by the calcination of a mixture of Na_2CO_3, Al_2O_3 and $LiNO_3$ in air, at ~1250^{o}C, followed by sintering at a temperature of ~1550^{o}C [4, 5]. Finally, the sintered samples are annealed to ensure the complete conversion of α - alumina to sodium beta”-alumina. There are several limitations to the traditional method of fabrication. High sintering temperature enhances soda loss from the samples, which could be avoided only by using an expensive encapsulation of samples using Pt bags or MgO crucibles. Remnant sodium aluminate ($NaAlO_2$) is present at the grain boundaries, which is hygroscopic in nature. Thus, beta”-alumina formed by this process is prone to moisture and CO_2 attack from the atmosphere and is stored in vacuum chambers in order to avoid degradation. In addition, the strength of conventional beta”-alumina is low, typically on the order of 200 MPa or less due to exaggerated grain growth. A novel patented vapor phase process is used for the conversion of sodium beta”-alumina in order to eliminate the limitations mentioned above [6]. In the vapor phase process, α- alumina is exposed to a source of Na_2O, forming a thin layer of sodium β”-alumina on the surface of the exposed α- alumina. Since β”-alumina is a good conductor of Na^{+} ions, the

diffusion of sodium ions through the same will be fast. Once the surface layer is formed, further conversion of alumina to β"-Al_2O_3 practically shuts off due to the sluggish diffusion of O^{2-} ions through sodium beta"-alumina. The rate of diffusion of Na_2O (formation of β"-alumina) will be dictated by the rate of diffusion of O^{2-} ions through β"-alumina. In fact, Nicholson et al. [7, 8] used the same approach as described above to form a thin layer of β"-alumina on sapphire crystals and the rate of film growth was very slow due to the low diffusion rate of oxygen ions. The phenomenon of coupled transport is utilized to enhance the rate of the conversion process. An alternate rapid path is provided for the diffusion of O^{2-}ions [6] by incorporating an oxygen ion conductor, yttria stabilized zirconia (YSZ), in the starting material. Thus, a coupled diffusion of Na^+ and O^{2-} ions will occur, leading to a faster conversion of alumina to sodium beta"-alumina. Once the thin layer of beta"-alumina is formed on the surface, Na^+ ions will diffuse through the formed beta"-alumina and O^{2-} ions through the YSZ present in the material. This process leads to the formation of a two-phase composite of BASE and zirconia. By choosing the composition of YSZ with low yttria content, typically 3 mol.%, a two-phase composite can be fabricated with strength of the order of ~900 MPa, which is more than four times that of the conventional BASE. In the vapor phase process, no encapsulation is needed as the conversion temperature is relatively low (1450°C), resulting in negligible soda loss. Moreover, the process is carried out in such a way that the thermodynamic activity of Na_2O is significantly lower than the activity of $NaAlO_2$, preventing the formation of hygroscopic $NaAlO_2$ at the grain boundaries. This is achieved by controlling the conversion temperature and the composition of Na2O in the mixture. The BASE thus formed will be resistant to atmospheric moisture and CO_2, and can even be boiled in water without any degradation. The first part of this work studies the role of coupled

transport in the fabrication of Na β"-alumina by vapor phase conversion.

1.2 Catalyst Degradation in PEM Fuel Cells

A proton exchange membrane fuel cell is a low temperature fuel cell that transforms chemical energy liberated during the electrochemical reaction of hydrogen and oxygen to electrical energy. Proton Exchange Membrane Fuel Cells (PEMFCs) have applications in transportation, distributed power, and portable power. Considerable progress has been made over the past two decades in PEMFC. However, it is well known that degradation in performance occurs over time, which in part has limited the commercialization of PEMFC. There are many factors which influence PEMFC degradation, which include the materials used in PEMFC and the operating conditions. Much of the current research is on catalyst degradation for PEM fuel cells with additional objectives of either obtaining higher catalytic activity than the standard carbon-supported platinum particle catalysts used in current PEM fuel cells or reducing the poisoning of PEM fuel cell catalysts by impurity gases. Typical catalysts used in PEM fuel cells are platinum/ platinum alloy nanoparticles embedded in carbon support. One of the reasons for alloying Pt with non-noble metals is to reduce the Pt loading and thus lower the cost [9-13]. Catalyst degradation occurs on both cathode and anode sides of PEMFC. Anode catalyst degradation is low because of the reducing atmosphere due to the presence of hydrogen. Several mechanisms of cathode degradation have been reported [14-20] including: (a) detachment of catalyst particles from carbon support, thus rendering them electro-catalytically inactive; (b) Ostwald ripening of particles; (c) agglomeration and associated growth (sintering) of particles; (d) dissolution of the catalyst at the cathode, its transport and precipitation into the membrane. All of these phenomena lead to a decrease

in the catalyst surface area, decrease in catalytic activity, and thus loss in performance. Studies have shown that greater degradation occurs at open circuit than when the fuel cell is under load. It is also known that negligible degradation occurs at the anode even when its composition is substantially the same as the cathode.

In the second part of the dissertation, the main focus is to study the role of coupled transport in catalyst/ nanoparticle degradation mechanisms. Out of the different degradation mechanisms mentioned above, this work studies mainly the effect of Ostwald ripening or agglomeration in nanoparticles. Ostwald ripening or coarsening is a process in which larger particles grow at the expense of smaller particles. Numerous theoretical and experimental studies on Ostwald ripening have been conducted over the past several decades [21-25]. Electrochemical Ostwald ripening is a process in which larger particles grow at the expense of the smaller ones as ion transport occurs through the ionomer/ion conducting medium and electron transport occurs via a conductive support. A few reports on electrochemical Ostwald ripening are also available in the literature [26-31]. In conventional solid state Ostwald ripening, metal particles grow by bulk or grain boundary diffusion. In electrochemical Ostwald ripening, growth occurs by a coupled transport of electrically charged species, for example, metal ions and electrons via parallel paths: metal ions through the liquid/ionomer and electrons through the metal or supporting carbon in PEMFC. Coarsening of ionic compounds dissolved in a solvent also occurs by electrochemical Ostwald ripening. An example is a super-saturated solution of NaCl in water; coarsening of particles occurs by a coupled transport of Na^+ and Cl^- through the solution. If two metal particles are isolated in an ion conducting medium, initially the smaller particles will tend to dissolve and precipitate on larger particles as the chemical potential of smaller particles is higher than that of the larger particles. Thus, for isolated

metal particles in an ion conducting medium (no or negligible electron concentration), particle growth is not expected. However, this process will occur if the particles are soluble as neutral species in the conducting medium. Assuming the presence of only ions in the ion conducting medium (little electronic conduction), ions will be transported through the conducting medium from smaller to larger particles leaving behind electrons. Thus, smaller particles will become negatively charged and the larger particles become positively charged. Once the electrochemical potential of ions in the particles is equilibrated, further ion transport will be shut down. However, the coarsening will occur if there is an alternate path for electrons. Coarsening will thus occur by a coupled transport of ions and electrons.

When two metal particles are in contact with each other in an ion conducting medium, the ions transport through the ion conducting medium and electrons through the metal particles in contact. This process is known as coalescence/agglomeration. The driving force is the same as for Ostwald ripening, and bulk diffusion and/or grain boundary diffusion determines the kinetics of growth in the solid state. The kinetics of this process is expected to be much faster compared to the typical solid state diffusion when the ion conducting medium is a liquid (such as an aqueous solution). In order to investigate the role of coupled transport in particle coarsening, initial research was conducted with copper particles treated under various test conditions. Copper powder was placed in DI water and in different solutions containing various concentrations of $Cu(NO_3)_2$. Copper particles in contact with each other are expected to grow at the expense of smaller particles while isolated copper particles should not grow. Analysis of the results obtained from these experiments gave insight into the mechanisms of particle coarsening by electrochemical Ostwald ripening/agglomeration.

The study of the mechanism of copper particle coarsening has direct implications to the cathode catalyst degradation in PEM fuel cells. The thermodynamic driving force for agglomeration/sintering and Ostwald ripening is the reduction in surface energy accompanying particle growth, which leads to dissolution of smaller particles and growth of larger particles. In PEMFC, transport of electrically neutral Pt occurs via a coupled process involving the transport of ions (Pt^{2+} and/or Pt^{4+}) through an ionomer or aqueous medium and a parallel (coupled) transport of electrons through the carbon support [31]. In agglomeration/sintering, a similar process occurs where ions transport through ionomer/aqueous medium and electrons transport through a direct particle-to-particle contact. The fundamental physical parameter which dictates degradation kinetics is the electrochemical potential of Pt ions, which depends upon the chemical potential of Pt. All those factors which lower the chemical potential of Pt should generally decrease the kinetics of degradation, and all those factors which increase the chemical potential of Pt should increase the kinetics of degradation.

The chemical potential of a species depends on composition, temperature, and pressure. Alloying Pt with other metals lowers the chemical potential of Pt. Hydrostatic stress (pressure) also affects the chemical potential, which is the basis of the Gibbs-Kelvin equation and is the reason for the occurrence of Ostwald ripening/agglomeration [32]. The dependence of chemical potential of Pt, μ_{Pt}, on temperature, composition, and on pressure is given by [32]

$$\mu_{Pt} = \mu_{Pt}^{o} + RT \ln a_{Pt} + pV_m \tag{1.1}$$

where μ_{Pt}^{o} is the standard state chemical potential of Pt, a_{Pt} is the activity of Pt, V_m

is the partial molar volume of Pt, and p is the pressure. If the material is pure Pt, then a_{Pt} is unity. For nanosize particles, the pressure is given by $2\gamma/r$ where r is the particle radius and γ is the surface energy. Thus, the smaller the particle size, the higher is the pressure inside the particle, the higher is the chemical potential, and the greater is the tendency for its dissolution and deposition on larger particles.

Equation (1.1) shows that the sign of pressure determines whether it will increase or decrease the chemical potential. Thus, if the pressure is positive (compressive), the chemical potential will be higher compared to a stress-free material. If the pressure is negative (tensile), however, the chemical potential should be lower compared to a stress-free material. Flood [33] demonstrated that the dominant term in chemical potential is linearly related to pressure (consistent with equation (1.1)), and thus electrode potential is expected to exhibit a reversal in sign upon a reversal in the sign of stress (tensile or compressive), in accord with the general thermodynamic theory of Gibbs. This analysis is important in the role of surface stress on catalyst stability and specifically on the design of core-shell catalysts. Core-shell catalysts typically consist of a core and a shell of different materials but generally of the same crystal structure, and with an epitaxially matched interface. The lattice parameters of the core and the shell determine the magnitude (and possibly the sign) of the stress in the shell of a core-shell catalyst. If the Pt shell is under greater compression than a pure Pt catalyst particle of the same diameter, the chemical potential of Pt will be higher in the shell of the core-shell catalyst than the monolithic Pt catalyst. Such a catalyst may exhibit increased tendency for dissolution. If the Pt shell is under reduced compression (or even possibly in tension) than a pure Pt catalyst of the same diameter, the chemical potential of Pt in the shell will be lower in the

core-shell catalyst than the monolithic Pt catalyst. Such a catalyst should exhibit decreased tendency for dissolution and thus should exhibit increased stability. An example is a core-shell catalyst with Pt shell and Ag or Au core. Such core-shell catalysts should be inherently more stable compared to pure Pt catalysts of the same outer diameter. This work studies the role of stress on the chemical potential of Pt using an electrochemical technique. Implications of the results for the design of core-shell catalysts for PEMFC are discussed. The implications for core-shell catalysts are further compared with recent literature atomistic level (DFT) calculations.

1.3 Specific Surface Energy and Shape Stability of Crystals

In order to successfully characterize nanoparticles and their coarsening, it is very important to analyze the properties of the surfaces or interfaces of the materials in use, rather than rely on bulk properties. One such aspect of materials is the specific surface energy. Surface energy quantifies the disruption of intermolecular bonds that occurs when a surface is created. Thus, it depends on the number of unsatisfied bonds on the surface of a particle. Specific surface energy is generally considered as a physical property of a material and is defined as a constant, specific to the material. Specific surface energy of a solid can be thought of as the work required to create a new surface of unit area at constant temperature, volume, and composition. The surface energy of a metal can be calculated from the bond energy, and the lattice constants of the metal. This approach is known as the broken-bond model or the cleaved–bond model of surface energy [34]. This method has been successfully used for many years to calculate the surface energies of solids from atomization energies, which takes into account only the nearest neighbor interactions. In order to determine the surface energies of solids, the

experiments are conducted at high temperature where the surface tension of the liquid is measured and is extrapolated to 0 K [35, 36]. Both theoretical and experimental works have been conducted to calculate the surface energy of solids [37-41].

In the case of bulk particles, the specific surface energy can be considered constant as the change in number of surface atoms (unsatisfied bonds)/ unit area with surface area is negligible with increasing size. When particle size is in the nano range, the number of unsatisfied bonds per unit surface area can be very high. For instance, consider a cubic crystal of the size of a unit cell has 14 atoms arranged in a face centered cubic structure. In this case, all of the atoms are on the surface, which leads to a very high specific surface energy for the particle. Samsonov et al. [42] studied the size dependence of the surface tension in nano-crystals using a thermodynamic perturbation method for Al and Xe. They found that surface tension decreases with increase in particle size and reaches a constant value for bulk materials. In this work, we are using a mathematical model to study the effect of particle size on specific surface energy and its shape stability in the case of nano and sub-nano particles of different shapes: cube, cubo-octahedron, tetrahedron, octahedron, and truncated octahedron.

1.4 Scope of the Thesis

The work presented in this thesis is the result of six years of research on different projects, which comes under the broad area of the role of coupled transport in materials and its effect in different applications – high temperature batteries and PEM fuel cells. The research was mainly focused on the effect of coupled transport in the fabrication of Na β”-alumina solid electrolyte used in electrochemical storage devices and catalyst degradation in proton exchange membrane fuel cells.

Chapter 2 presents the design, fabrication, and testing of sodium zinc chloride batteries. Electrochemical tubular and planar cells of configuration, Na/BASE/$ZnCl_2$, were constructed and tested. The analyses of the results implied that zinc chloride is a viable cathode. Several freeze-thaw cycles were conducted on the planar cell with a stable performance output. A three-cell stack was designed, constructed, and electrochemically tested. A five-cell stack was designed and constructed. In Chapter 3, the kinetics of fabrication of β"-alumina was studied using a novel patented vapor phase method [6] for

the conversion of α-alumina to β"-alumina. A rapid parallel path was provided for O^{2-} ions by incorporating yttria-stabilized zirconia (YSZ) to the starting material, thus making the diffusivities of both Na^{+} ions and O^{2-} ions comparable. Several α-alumina+YSZ discs were fabricated with different grain sizes ranging from 0.52μm to 4.1μm. The effect of grain size on the rate of conversion was studied by converting these discs to Na β"-alumina+YSZ and the results were analyzed.

Chapter 4 deals with the study of the role of coupled transport in copper particle coarsening. Experiments on the growth of copper particles in aqueous media containing various concentrations of copper ions (by dissolving copper nitrate) were conducted at room temperature and at 80°C. In order to obtain as low a concentration of copper ions as possible, experiments were also conducted in DI water with hydrogen bubbling. For determining the kinetics of particle growth, experiments were conducted for different time periods varying between 12 h and 144 h at room temperature in DI water, in DI water with hydrogen bubbling, and in 0.01 M $Cu(NO_3)_2$ solution. Analyses were done on the results obtained in this work which has direct implications to the catalyst degradation in fuel cells.

In Chapter 5, the effect of applied stress on the chemical potential of Pt was measured using an electrochemical cell. Two platinum wires/foils were immersed in a $PtCl_4$+DMSO solution. One of the wires/foils was subjected to a tensile stress while the other one was left load-free. It was observed that the wire/foil subjected to a tensile stress developed a positive electric potential compared to the unstressed one, indicating that the application of a tensile stress decreases the chemical potential of platinum. When the wires/foils were connected externally, the diameter/thickness of the one under tensile stress grew while the diameter/thickness of the unstressed one shrank. These results thus suggest an approach for the development of stable cathode catalysts for PEMFC. The present work shows that core-shell catalysts consisting of a core and Pt shell having the same crystal structures, the Pt shell having a smaller lattice parameter than the core, and the Pt shell epitaxially matched to the core will result in a tensile stress (or reduced compression) in the Pt shell. Such core-shell catalysts should be inherently more stable as the tensile stress in the Pt shell will lower its chemical potential and decrease its tendency for dissolution. These results thus also show the usefulness of continuum thermodynamic modeling in the design of nanoscale materials. Chapter 6 presents the simple broken-bond model that was used to investigate the specific surface energy of f.c.c. metals as a function of shape and size. It also discusses the results of continuum thermodynamic modeling that is comparable to DFT calculations in the literature for determining the surface energy and shape stability of nano particles. Higher specific surface energy of small particles is due to a greater proportion of atoms at the edges and corners, which exhibit greater number of unsatisfied bonds. Beyond an equivalent diameter of ~5 nm, the specific surface energy was nearly constant for each shape investigated. Thus, specific surface energy may be considered independent of size beyond ~5 nm. Beyond

this critical size, octahedral and tetrahedral shapes were the most stable, truncated octahedron was the second most stable, cubo-octahedron was the third most stable, and cube was the least stable. A summary of important conclusions and recommendations for future research in high temperature energy storage devices and efficient cathode catalysts for PEM fuel cells is presented at the end of this thesis.

1.5 References

1. P.T. Mosley, *The solid electrolyte: properties and characteristics*, p. 19, in *The sodium-sulfur battery*, J. L. Sudworth and A. R. Tilley, Editors, Chapman and Hall, London (1985).

2. J. Coetzer, *J. Power Sources*, **18,** 377 (1986).

3. C-H. Dustmann, *J. Power Sources*, **127**, 85 (2004).

4. G. E. Youngblood, A. V. Virkar, W. R. Cannon and R. S. Gordon, *Bull. Amer. Ceram. Soc.*, **56** (2), 206 (1977).

5. A. V. Virkar, M. L. Miller, J. B. Cutler and R. S. Gordon, *U.S. Patent*, 3 113 928 (1978)

6. A. V. Virkar, J-F. Jue, and K-Z Fung, *U.S. Patent No. 6,117,807*. (2000).

7. C. K. Kuo and P.S. Nicholson, *Solid State Ionics*, **67**, 157 (1993).

8. C. K. Kuo and P.S. Nicholson, *Solid State Ionics*, **82**, 173 (1995).

9. M. S. Wilson, F. H. Garzon, K. E. Sickhaus and S. Gottesfeld, *J. Electrochem. Soc.*, **140**, 2872 (1993).

10. R. Ornelas, A. Stassi, E. Modica, A. S. Arico, and V. Antonucci, *ECS Trans.*, **3**(1) 633 (2006).

11. X. Wang, R. Kumar, and D. Meyers, *Electrochem. Solid State Lett.* **9**, A225 (2006).

12. J. Xie, D. L. Wood, III, K. L. More, P. Atanassov, and R. L. Borup, *J. Electrochem. Soc.*, **152**, A1011 (2005).

13. P. J. Ferreira, G. J. Lao, Y. Shao-Horn, D. Morgan, R. Makharia, S. Kocha and H. A. Gasteiger, *J. Electrochem. Soc.*, **152**, A2256 (2005).

14. W. Bi, G. E. Gray and T. F. Fuller, *Electrochem. Solid-State Lett.*, **10**, B101 (2007).

15. K. Yasuda, A. Taniguchi, T. Akita, and Z. Siroma, *Phys. Chem. Chem. Phys.*, **8**, 746 (2006).

16. A. Ohma, S. Suga, S. Yamamoto, and K. Shinohara, *ECS Trans.*, **3**(1), 519 (2006).

17. H. Liu, J. Zhang, F. D. Coms, W. Gu, B. Litteer, and H. A. Gasteiger, *ECS Trans.*, **3**(1), 493 (2006).

18. A. Laconti, H. Liu, C. Mittelsteadt, and R. McDonald, *ECS Trans.*, **1**(8), 199 (2005).

19. B. Merzougui and S. Swathirajan, *J. Electrochem. Soc.*, **153**(12), A2220 (2006).

20. K. L. More, R. Borup, and K. S. Reeves, *ECS Trans.*, **3**(1), 717 (2006).

21. P. W. Voorhees, *J. Stat. Phys.*, **38**, 231 (1985).

22. S. P. Marsh, M. E. Glicksman, *Acta Materialia,* **44,** 3761 (1996).

23. H. Gratz, *J. Mater. Sci. Lett.*, **18**, 1637 (1999).

24. P. Streitenberger, *Scripta Mater.*, **39**, 1719 (1998).

25. G. Madras, B. J. McCoy, *Powder Tech.*, **143**, 297 (2004).

26. W.H. Mulder, J.H. Sluyters, *J. Electroanal. Chem.*, **468**, 127 (1999).

27. P. L. Redmond, A. J. Hallock, L. E. Brus, *Nano Lett.*, **5**, 131 (2005).

28. A. Schroeder, J. Fleig, D. Gryaznov, J. Maier, W. Sitte, *J. Phys. Chem. B,* **110**, 12274 (2006).

29. A. Schroeder, J. Fleig, H. Drings, R. Wuerschum, J. Maier, W. Sitte, *Solid State Ionics*, **173**, 95 (2004).

30. A. Schroeder, J. Fleig, J. Maier, W. Sitte, *Electrochimica Acta*, **51**, 4176 (2006).

31. A.V. Virkar, Y. Zhou, *J. Electrochem. Soc.*, **154**, B540 (2007).

32. O.F. Devereux, *Topics in Metallurgical Thermodynamics* , John Wiley-Interscience, New York (1983).

33. E. A. Flood, *Can J. Chem.*, **36**, 1332 (1958).

34. G.A. Somorjai, *Introduction to Surface Chemistry and Catalysis*, John Wiley & Sons, New York (1994).

35. L.E. Murr, *Interfacial Phenomena in Metals and Alloys*, p. 122, Addison – Wesley Publishing Co., Pennsylvania (1975)

36. I.S. Grigoriev, E.Z. Meilikhov, Editors. *Handbook of Physical Quantities*, p. 417, CRC Press, Florida (1997).

37. J.M. Blakely, *Introduction to the properties of Crystal Surfaces*, Pergamon, (1973).

38. R.G. Linford, *Quart. Rev. Chem. Soc.*, **1**, 445 (1972).

39. H. Mykura, *Solid Surfaces and Interfaces*, Dover, New York (1966).

40. J.G. Eberhart, S. Horner, *J. Chem. Ed.*, **87**, 6 (2010).

41. W. R. Tyson, W. A. Miller, *Surf Sci.* **62**, 267 (1977).

42. V.M. Samsonov, N.Y. Sdobnyakov, A.N. Bazulev, *Colloids and Surfaces A: Physicochem. Eng. Aspects* **239**, 113 (2004).

CHAPTER 2

HIGH TEMPERATURE SODIUM – ZINC CHLORIDE BATTERIES WITH SODIUM BETA"- ALUMINA SOLID ELECTROLYTE (BASE)

2.1 Introduction

In the present day scenario, electricity is one of the most important forms of energy that needs to be conserved. It is well known that the demand for electricity varies depending upon the time of day; low demand during night and high demand during day. Figure 2.1 shows a typical load curve over the time of day [1]. Since virtually all power plants are designed for peak power, there is excess capacity during off-peak periods, which is underutilized. This was one of the main reasons for the emergence of electrochemical energy storage devices such as batteries. Thus, power plants can be designed for average demand with the excess energy during off-peak periods stored for use during high peak demands. This will considerably augment the capacity of power plants and lower the capital cost. Considerable research is going on in producing electricity from nonconventional energy resources like tapping tidal, wind, or solar energies. The main disadvantage of such renewable resources is their inconsistency in availability as it depends on the geographical locations, climatic conditions etc. Consequently, the electrochemical energy storage devices can be used to store the energy produced while the resources are available and use the stored energy while they are not.

The methodology of storing the excess energy produced during night can be

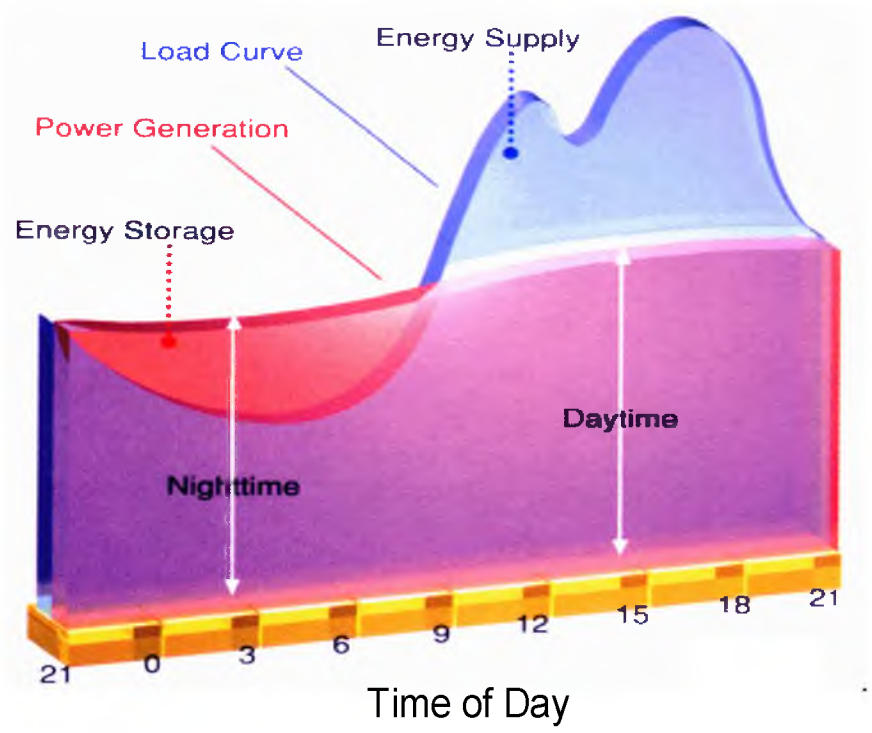

Figure 2.1 Power demand as a function of time of day

effectively materialized if the energy storage system has a round-trip efficiency above 90%. While R & D on many of the storage battery concepts have not been actively pursued in the United States for the past decade or so, a major effort is underway around the world, with commercialization of load leveling batteries well on its way in Japan. The fundamental concept and early developments of such electrochemical energy storage systems, nevertheless, have their origins in the United States. One such technology is based on a solid electrolyte, much in the same manner as SOFC. [2-4] The most advanced concept is the Na-S battery, which has now been developed to a point where it can be subjected to over 4500 cycles (at 80% Depth of Discharge), has a demonstrated life of greater than 13 years in a 500 kW size, and 9 years in a 8MW size and projected life of over 15 years [5, 6]. The principal developer of Na-S battery is NGK in Nagoya, Japan, with a factory at Kamacki, near Nagoya, built jointly by NGK and Tokyo Electric

Power Company (TEPCO). Currently, sodium sulfur batteries are being used for energy storage by NGK in Nagoya, Japan. In the US, American Electric Power (AEP) and Xcel Energy have started utilizing sodium sulfur batteries for large-scale energy storage. In 2010, a small city in West Texas installed a medium sized sodium sulfur battery that can power the entire town and serve as emergency backup.

The Na-S battery comprises liquid sodium anode, solid BASE, and liquid sulfur cathode impregnated in graphite felt [1, 4, 7, 8]. The discharge part of the cycle comprises passing Na^+ ions through BASE into the sulfur electrode with electrons transporting in the external circuit to form sodium polysulfides. During the charging part of the cycle, Na^+ ions transport from the sulfur electrode through the BASE to the Na anode, with electrons transporting in the external circuit. The batteries use one end closed BASE tubes, and stainless steel or Ebrite containers with a protective chromium coating to prevent corrosion induced by sulfur and sodium polysulfides. Several cells are configured in a module with series and parallel connections for optimum performance and reliability.

The cell reaction is

$$Na + xS \rightarrow Na_2S_x \text{ (EMF: 2.08 ~ 1.78V) } T = 300^oC \quad (2.1)$$

A sodium sulfur battery has demonstrated a round trip efficiency of > 90% and has five times peak power capacity and thermal cycling. Moreover, it has a potential for projected low cost. However, the sodium sulfur batteries have low volumetric power density due to their tubular design and the module size cannot be made sufficiently compact. In these batteries, it is necessary to use graphite felt in the cathode since sulfur or polysulfides are electrical insulators. The use of graphite increases cost and volume.

The use of stainless steels or other inexpensive materials is not possible due to corrosion. When a Na–S battery fails, its resistance increases, thereby rendering the entire series leg inoperative – it becomes open circuit. To minimize the probability of failure, the charging current density is maintained lower than desired. Also, due to corrosion-related issues, a protective coating is required on the cathode side of the container.

Another approach is to use a Zebra battery which uses $NiCl_2$ + NaCl as the cathode, wherein during the discharge cycle, Na reacts with $NiCl_2$ to form NaCl, releasing metallic Ni [9, 10]. The cell reaction is

$$2Na + NiCl_2 \rightarrow 2NaCl + Ni \text{ (EMF}\sim 2.57V, 300^{o}C) \quad (2.2)$$

One of the advantages of the Zebra batteries as compared to Na-S batteries is that the battery fails with a low resistance. That is if one cell in the series leg fails, it acts as a short, and the other cells can be used with this failed cell in series. The lowest melting liquid in the NaCl-$NiCl_2$ system occurs at ~575^{o}C. Thus, to impart sufficient sodium ion conductivity to the cathode, some low melting $NaAlCl_4$ is also added to the cathode. Due to corrosion-related problems, an inverted design is used with the cathode placed inside the BASE tube. Unfortunately, this design is not preferred since it increases the volume and lowers the specific energy and specific power. In order to overcome the above-mentioned limitations of both Na-S and Zebra batteries, an alternative battery concept is investigated here: sodium zinc chloride batteries.

2.1.1 Sodium Zinc Chloride Battery

Sodium zinc chloride batteries have liquid sodium as anode and zinc chloride as cathode with sodium β”-alumina solid electrolyte. Compared to Na-S batteries and Zebra

batteries, sodium zinc chloride batteries have some positive attributes. Zinc chloride does not corrode any of the materials of construction, such as steels, which makes it possible to use inexpensive materials. Hence, graphite is not required in the cathode. Instead, steel wool can be used to help enhance the cathode conductivity. Unlike Na-S batteries, the cathode of sodium zinc chloride batteries has high electrical conductivity due to the formation of metallic Zn, which implies that a low resistance shunt forms if a cell fails. Thus, if one cell fails, the rest of the cells in a series leg continue to function normally and deliver power. The cathode is liquid over a wide temperature range as zinc chloride is a low melting salt.

The cell reaction is

$$2Na + ZnCl_2 \rightarrow 2NaCl + Zn \text{ (EMF} \sim 2.4V, 350^oC) \quad (2.3)$$

During discharge, Na^+ ions pass through Na β"-alumina electrolyte to the cathode, forming NaCl and Zn metal and the electrons pass through the external circuit. During charge, metallic sodium is formed in the anode side with electrons passing through the external circuit. Sodium β"-alumina is the common candidate for these high temperature energy storage systems. Figure 2.2 shows the crystal structure of sodium β"-alumina [1]. It has a rhombohedral structure which can be indexed as hexagonal. It is very refractory with melting temperatures well above 1650°C. It exhibits excellent sodium ion conductivity at relatively low temperatures (300°C) in the basal plane of the hexagonal structure. By virtue of the presence of Al_2O_3 as the main constituent in Na β"-alumina, its stability in oxidizing and reducing environments is far superior to that for other known ion conductors. Thus, devices based on Na β"-alumina can withstand well over 4.0V without electrolyte reduction or decomposition.

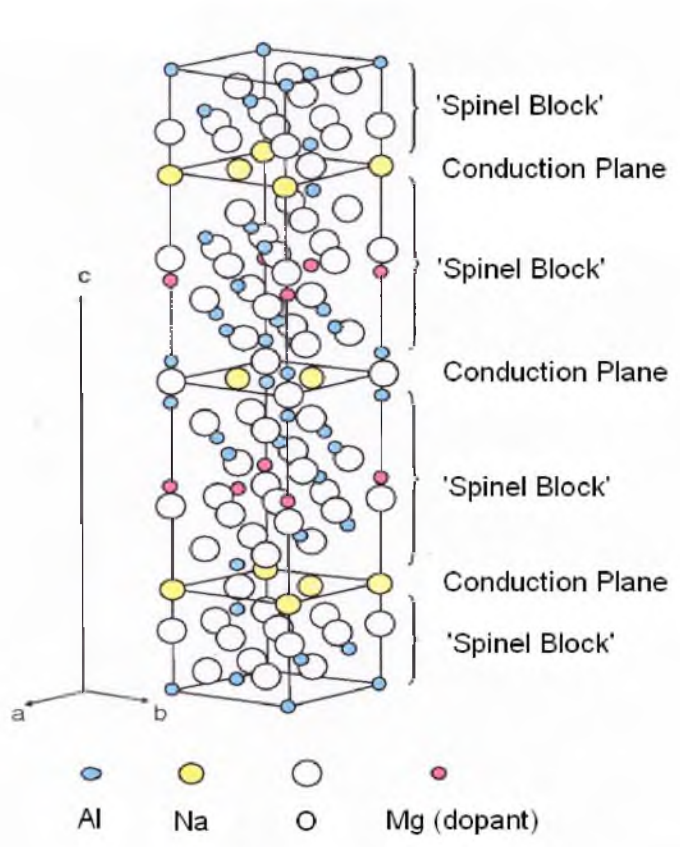

Figure 2.2 Crystal structure of Na β"-alumina

There are two types of fabrication methods: conventional method and vapor phase method. In the conventional process, a mixture of Na_2CO_3, Al_2O_3, and $LiNO_3$ is calcined at 1250°C. Tubes are formed and encapsulated in MgO crucibles or platinum bags for liquid phase sintering at 1550°C. It is then followed by annealing for complete conversion to β". There are some limitations for the conventional process. As sintering is done at relatively high temperature, soda loss can occur. To prevent soda loss, expensive encapsulation of the samples is required. Moreover, sintering occurs by a transient liquid phase containing $NaAlO_2$.

Even after annealing, there is remnant $NaAlO_2$ along the grain boundaries rendering the sample moisture sensitive. In the case of the vapor phase process, the

conversion temperature is lower than the conventional process. Thus, it does not require expensive encapsulation, unlike the conventional method. Also, the process never produces $NaAlO_2$ at the grain boundaries, which makes the β"-alumina fully resistant to moisture attack and it can be boiled in water without any degradation [11].

2.2 Experimental Procedure

2.2.1 Fabrication of Na β"-alumina Discs and Tubes

In order to fabricate β"-alumina discs by the vapor phase process, the starting materials used were CR 30 (Baikowski International Corporation, high purity $\alpha - Al_2O_3$) and TZ – 3Y (Tosoh corporation, 3 mol.% Y_2O_3- partially stabilized tetragonal zirconia). Seventy percent by volume of CR 30 and thirty percent by volume of TZ – 3Y were dispersed in the pH 10 solution and dried. It was then ball milled with ethanol for 8 hours. The dried powder was ground, sieved, and compacted to form circular discs by die – pressing uniaxially at 10,000 psi. The discs were then isostatically pressed at 30,000 psi. The samples were heated at 4^oC/min in air to 1600^oC and maintained at temperature for 1 hour and subsequently cooled at the same rate. The density of the sintered samples was > 99% of the theoretical density. In order to convert the α-Al_2O_3+TZ–3Y discs to β"-alumina (BASE), the samples were packed in a BASE packing powder in a ceramic 4-YSZ crucible and heat treated at elevated temperatures, typically 1450^oC. XRD was conducted on the samples to make sure the conversion occurred from α-alumina to β"-alumina. Na β"-alumina one end closed tubes were also made for electrochemical tests. These tubes were subsequently used for electrochemical tests on symmetric (same both electrodes) and asymmetric Na/BASE/$ZnCl_2$ cells. The tubular samples were further analyzed after conducting several electrochemical tests.

2.2.2 Conductivity Measurement of β"-alumina Tubes

The first experiment performed was to determine the conductivity of the BASE tube. For this experiment, a symmetric cell was used. From the phase diagram of NaCl – $ZnCl_2$, it is found that a eutectic is present at 262°C with 71 mol. % $ZnCl_2$ [12]. The experimental set up was placed inside an argon filled glove box with the configuration given below.

$$Zn \mid ZnCl_2 + NaCl \text{ (eutectic)} \mid BASE \mid ZnCl_2 + NaCl \text{ (eutectic)} \mid Zn \qquad (2.4)$$

The BASE tube was placed in a glass test tube. A eutectic mixture of NaCl and $ZnCl_2$ with Zn metal turnings was melted. Since the melting point of zinc is 419.6°C, it will remain solid in the mixture. The inside and outside of the BASE tube were filled with a eutectic mixture of NaCl and $ZnCl_2$ (eutectic temperature ~ 252°C) and zinc electrodes were placed in the molten salt. The cell was placed within a small tube furnace and heated to 350°C. The temperature was controlled using a thermocouple placed outside the glass tube. Voltage and current leads were connected to the Zn electrodes, the negative terminal to the electrode inside the BASE tube. The cell was then cycled at constant current mode supplying 500 mA for 50 hours. The test was terminated after the contact to the outer zinc electrode accidentally broke.

2.2.3 Planar Cell Design and Construction

To construct a planar cell, a tape cast BASE disc of diameter 2" and thickness 1.1mm was used. The first planar cell was assembled in the partially charged state at eutectic composition. The advantage of this method is that the eutectic composition melts at the lowest possible temperature (262°C). It is easy to melt and there is no problem of

segregation. However, in this construction, both metallic sodium and zinc need to be incorporated in the cell. Steel end plates with cavities were used for containing cathode and anode. On the lower end plate, a mixture of sodium chloride and zinc chloride (1:3 by weight) was added with a small amount of zinc metal. This is the positive electrode side. On the upper end plate, sodium metal was added, which is the anode side. This was done by impregnating the salt mixture in a '0' grade steel wool. The BASE disc was placed inbetween the two end plates. The anode and cathode compartments were sealed with the help of copper gaskets. The steel end plates have a groove with knife edges to form a good seal. Thin stainless steel sheets were attached by spot welding on both ends of the steel plates, which act as positive and negative electrode contacts. The author wishes to express her gratitude to her mentor, Dr. Neill Weber, who was abundantly helpful and offered invaluable assistance, support, and guidance while doing this project, especially with the design and construction of cells and cell stacks.

2.2.4 Electrochemical Testing of Tubular and Planar Cells

The tubular cell was assembled in the fully charged state. The electrochemical cell was constructed by placing a cylindrical electrode of stainless steel into a glass test tube of outer diameter 25 mm. Zinc sheet rolled into a cylinder was placed inside and in contact with the cylindrical steel electrode. An aluminum pin of approximately the same dimensions (slightly smaller) as that of the BASE tube was inserted and "0" grade steel wool was wedged into the annulus. This steel wool was degreased and cleaned before inserting into the tube. After removing the metal pin, the required quantities of salts of previously fused and ground salt of sodium chloride and zinc chloride (eutectic composition) was added to the glass tube. The bottom of the tube was heated in a furnace

after evacuation and back filling with Argon. The temperature was raised to ~420^{o}C. The sealed tube was then cooled, transferred to the glove box, and reheated up to 375^{o}C to insert the BASE tube sealed to the alumina tube through the hole in the steel wool and into the molten salt. A safety tube made of steel was filled with molten sodium and inserted into the BASE tube. This safety tube was made in such a way that there was a little hole on the bottom to facilitate flow of sodium in and out of the tube. Copper wire was inserted into the safety tube as the negative electrode. The open end of the alumina tube was sealed with a silicone rubber cork. Voltage and current leads were connected to the electrodes with negative terminal connected to the copper wire and the cell was operated in the constant current mode.

A planar cell was assembled in the partially charged state at eutectic composition. This setup was then placed in a tube furnace inside a glove box. The effective cell area was about 11.3 cm^{2}. The amount of sodium in the anode compartment was 2ml. Voltage and current leads were connected to the stainless steel electrodes with negative terminal connected to the end plate containing metallic sodium. The cell was operated in the constant current mode at a temperature of 400^{o}C. After several charging and discharging cycles, the testing was stopped and the furnace was turned off. The test setup was allowed to freeze. Then, it was heated and tested again to determine the differences in performance of the planar cell. This freeze – thawing was done five times followed by several charge-discharge cycles under the same test conditions as above.

2.2.5 Cell Stack Design and Construction

Three planar cells were assembled in the completely discharged state. Each cell was assembled separately and connected in series with the help of a stainless steel

cylindrical block of diameter 1.5" and length about 1 inch. If these spacers were not used, the area of contact between the cells would have been lower, resulting in an increase in resistance, thereby increasing the voltage loss associated with it. The three–cell stack was then placed in a tube furnace inside a glove box. The effective cell area of each cell was about 11.3 cm^2. The cathode of each cell contained 5.85g NaCl, 6.82g $ZnCl_2$, and 2g Zn. The choice of the proportion of NaCl to $ZnCl_2$ was based on the available information on the phase diagram [12]. Voltage and current leads were connected to the stainless steel electrodes with negative terminal connected to the upper end plate of the top cell and positive terminal connected to the lower end plate of the bottom cell. The cell stack was charged in a constant current mode at a temperature of 400°C.

2.3 Results and Discussion

X-ray diffraction patterns of the as-sintered and converted samples were analyzed. Figure 2.3 shows the identified peaks of the as-sintered α-alumina/YSZ sample and the converted β"-alumina/YSZ sample. In the second XRD pattern, all the YSZ peaks remain the same as that in the first XRD pattern while the α-alumina peaks in the as-sintered sample were fully converted to β"-alumina peaks.

2.3.1 Conductivity of the BASE Tube

There was no evidence of increase in resistance with time. From the values of voltage and current obtained from the experiment, the resistance of the overall cell was calculated to be 0.15 Ω with effective cell area 25 cm^2. This includes the resistance of the BASE tube, molten salts, and the polarization resistances. The estimation of resistivity of the BASE tube from this test requires knowledge of the resistivity of the eutectic salt. Analysis of the beta"-alumina tube was done using a Scanning Electron Microscope

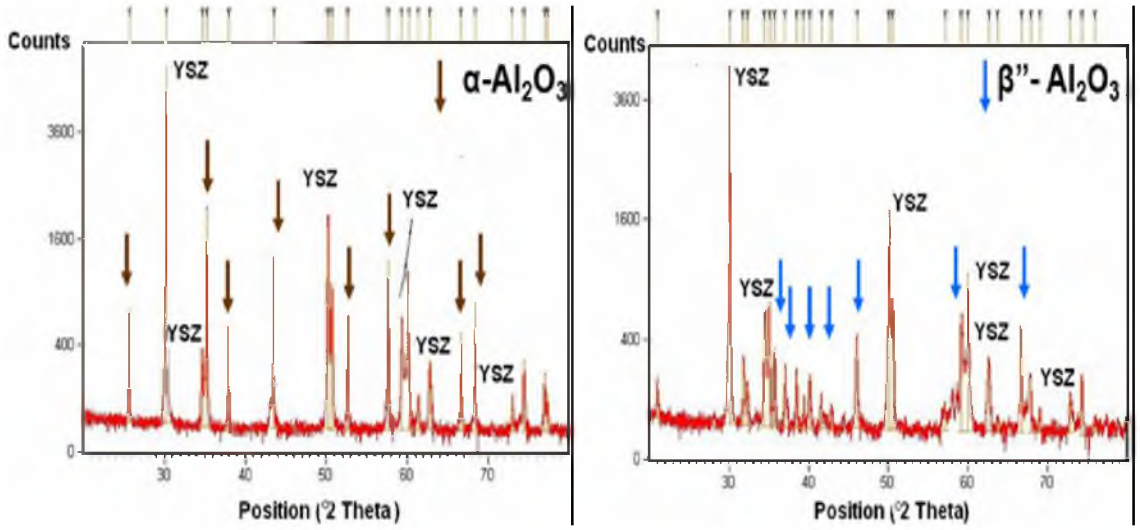

Figure 2.3 XRD patterns of as-sintered α-alumina/YSZ sample and converted β"-alumina/YSZ sample

(Figure 2.4). The elements detected were oxygen, aluminum, sodium, and zirconium, as expected. No zinc was found in the sample, which indicates that the ion exchange between sodium and zinc ions did not occur. This is a very important result, and demonstrates the viability of the concept proposed.

2.3.2 Electrochemical Testing of Tubular and Planar Cells

Figure 2.5 shows the voltage response curve of the tubular cell, which was assembled in the fully charged state. Initially, a current of 50mA was passed, which was gradually increased to 250mA in steps. After 1 hour, the current was increased to 500mA and the cell was discharged for about 2.5 hours with discharge voltage of about 2.0V.The current was again increased to 1A and the cell was discharged for another 2 hours with the output voltage of about 1.85V. The cell was disconnected from the circuit without reducing the temperature and left overnight. During the first run of the planar cell, a constant current of 20 mA was passed, which was gradually increased to 50 mA (Figure 2.6).

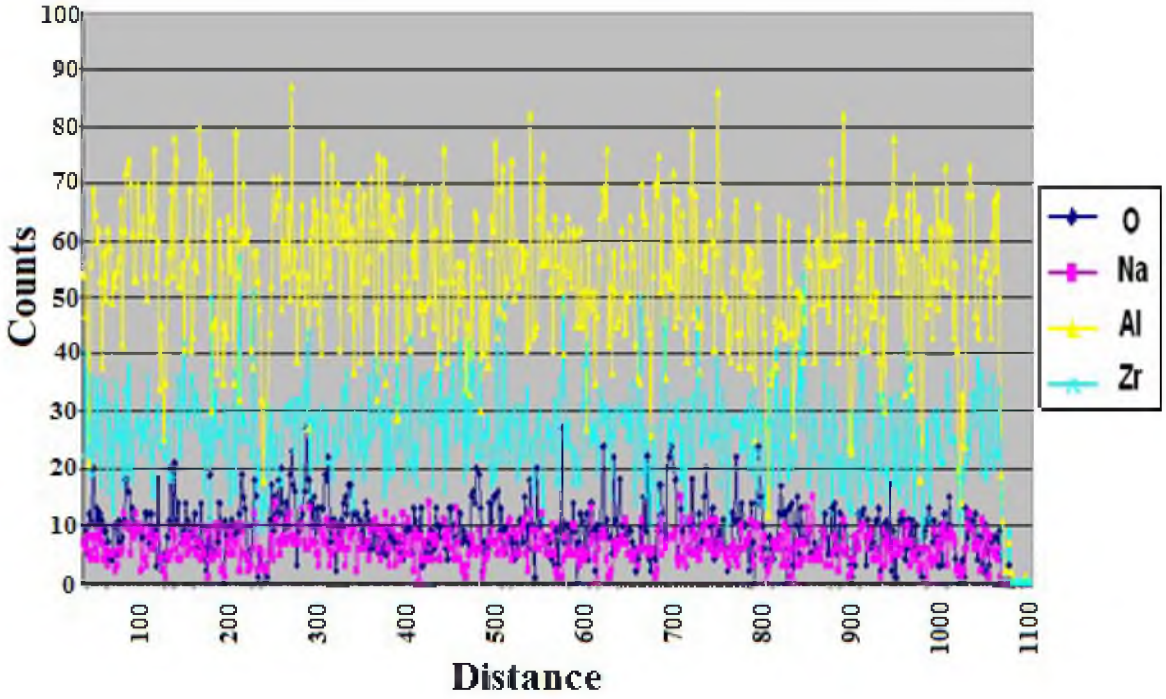

Figure 2.4 Chemical line scan of β”-alumina tube after 50 hours cycling

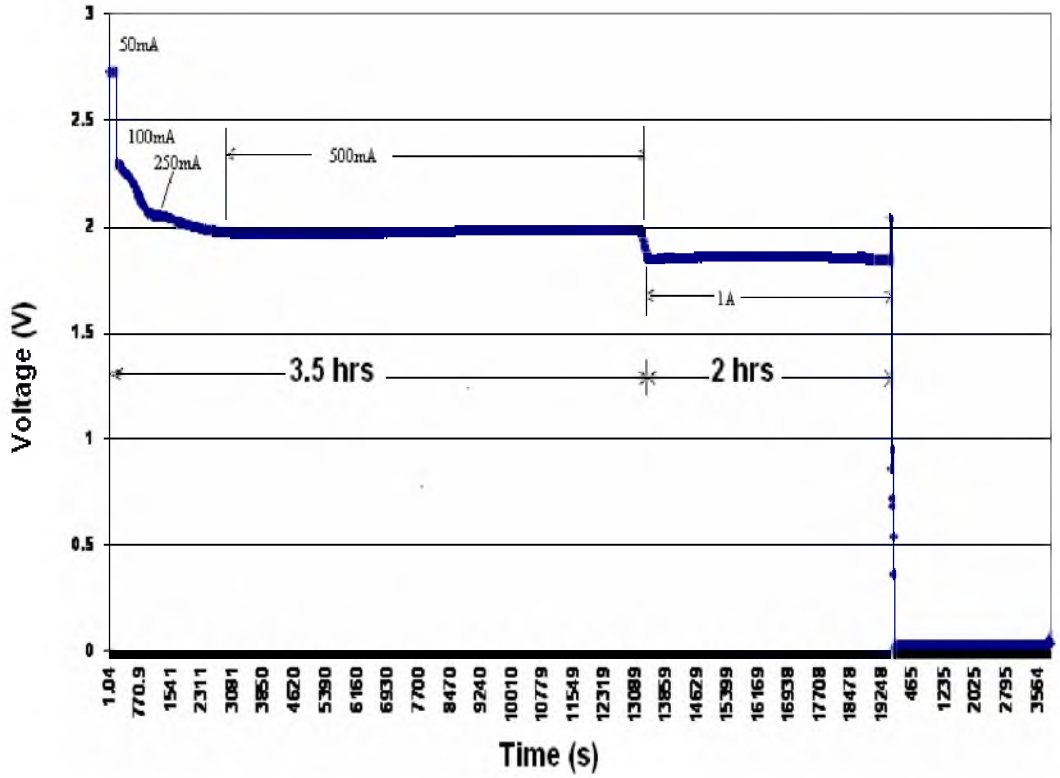

Figure 2.5 Voltage response of the tubular cell, T = 350°C, Time ~ 5.5 hours

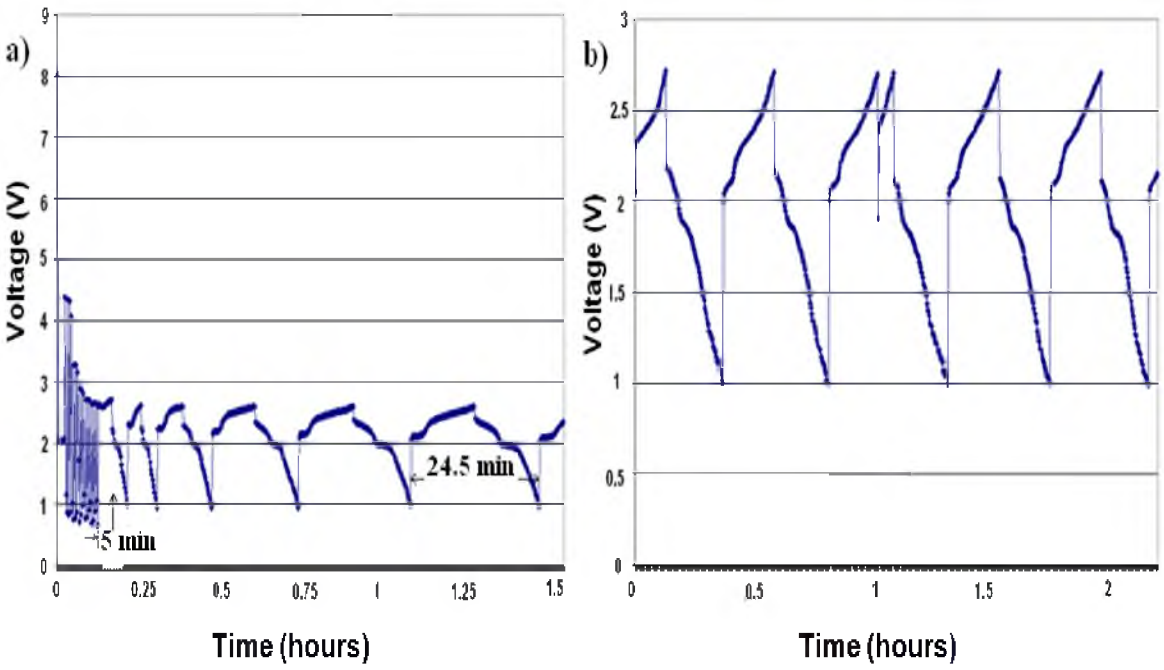

Figure 2.6 Voltage responses of planar cell after initial run and five freeze–thaw cycles

It was operated for about 4 hours and it showed no electrolyte failure or any other type of short. After the first freeze-thaw cycle, the cell was operated for about 2 hours at 50 mA. The cell was run for 3 hours after three freeze-thaw cycles at a constant current of 100 mA. The performance of the cell improved after each freeze-thaw cycle. After the fifth freeze-thaw cycle, the cell was operated for 1.5 hours at a constant current of 1A (Figure 2.6). The variation of voltage with time in a given cycle is due to very small amounts of materials in the electrodes in these experimental cells. It has already been shown that in the tubular cells with larger amounts of materials, the voltage vs. time plots are essentially flat (Figure 2.5).

After five freeze-thaw cycles, the planar cell was disassembled and analyzed under a scanning electron microscopy (Figure 2.7). Even after 5 freeze-thaw cycles, the electrolyte survived with no cracks. No ion exchange occurred, showing that zinc chloride is a viable cathode material for the rechargeable battery.

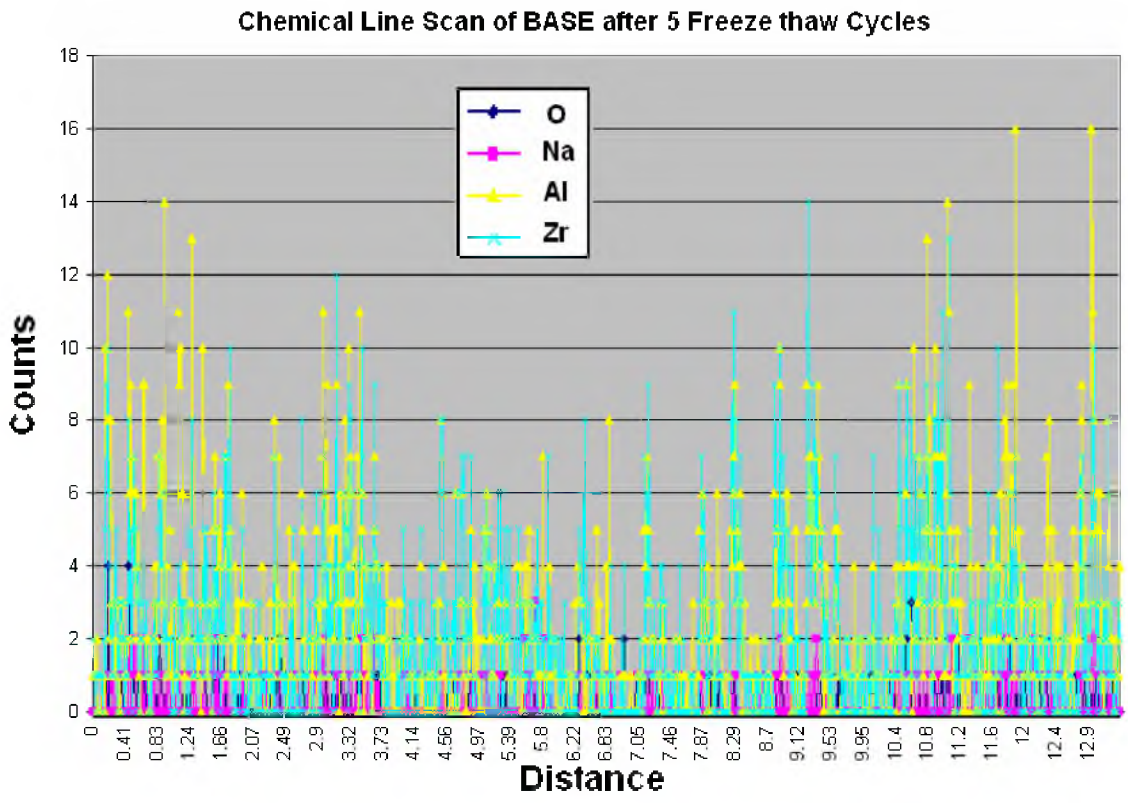

Figure 2.7 Chemical line scan of the planar cell electrolyte showing no trace of zinc

2.3.3 Testing of Three-cell Stack

The charging was done at a temperature of 400^{o}C. To ensure efficient charging, each cell was charged separately by passing equal amount of charge. Charging was started with a constant current of 10mA, which was gradually increased to 40mA. It was started as a three-cell stack. However, the top cell was found short circuited due to the misalignment of the electrolyte, and thus tested as a two-cell stack. Even though one of the cells in the cell stack was inoperable, the other two cells in the stack were tested. This is due to the fact that unlike sodium sulfur batteries, Na – $ZnCl_2$ batteries have high electrical conductivity due to the formation of metallic Zn in the cathode, which implies that a low resistant shunt forms when the cell fails.

The voltage response of the three-cell stack (with one failed cell) was analyzed

(Figure 2.8). A stable voltage is obtained, unlike the single planar cell response. This is due to the fact that the cathode and the anode compartment volumes are larger compared to the previous planar cell. A five-cell planar stack was designed and constructed (Figure 2.9). In the future, the constructed five-cell stack will be electrochemically tested and a ten-cell planar stack will be designed and tested followed by a full electrochemical characterization.

2.4 Conclusion

In conclusion, electrochemical tubular and planar cells of configuration, Na/BASE/$ZnCl_2$, were constructed and tested. There was no evidence of Zn ion exchange found in BASE. This implies that zinc chloride is a viable cathode. Several freeze-thaw cycles were conducted on the planar cell with a stable performance output. A three-cell stack was designed, constructed, and electrochemically tested.

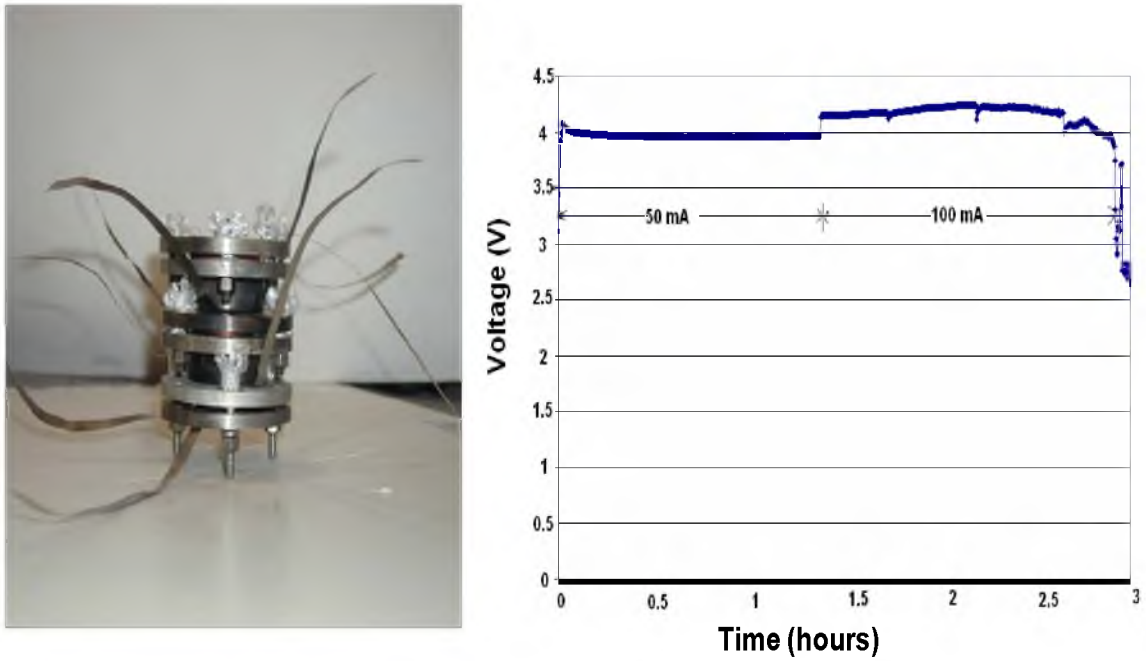

Figure 2.8 Planar cell stack and the voltage response of the two-cell stack operated at a temperature of 400°C

Figure 2.9 Five-cell planar stack arrangement

During the electrochemical testing, one of the cells became inoperable due to the misalignment of the electrolyte. As the electrode materials are highly conductive due to the presence of metallic Zn in cathode, the cell got short circuited with low resistance. The whole stack was tested as a two-cell stack. The stack gave a stable charging voltage of ~ 4.0 V. A five-cell stack was designed and constructed.

2.5 Acknowledgments

This work is supported by the U. S. Department of Energy under 'High Temperature Electrochemistry Center (HiTEC) Advanced Research Program' DOE Contract Number: **DE-PS26-05NT42470-1A**

2.6 References

1. M. McNamee, *Sodium-Sulfur Batteries*, *Modern Battery Technology*, p. 458, Ellis Horwood, Ltd, New York and London (1991).

2. R.S. Gordon, W. Fischer, A.V. Virkar, *Ceramic Transactions,* p. 203, American

Ceramic Society, Westerville, Ohio (1996).

3. J. L. Sudworth, *Modern Batteries: An Introduction to Electrochemical Power Sources*, Colin A. Vincent and Bruno Scrosati, Editors., p. 243, Arnold (Hodder Headline Group), London and John Wiley & Sons, New York (1997).

4. J.L. Sudworth and A. R. Tilley, *The Sodium Sulfur Battery*, Chapman and Hall, London (1985).

5. M. Kamibayashi and K. Furuta, *High Charge and Discharge Cycle Durability of the Sodium Sulfur (NAS) Battery*, Tokyo Electric Power Company and NKG Insulators, Ltd., presented at EESAT (2002).

6. T. Oshima and K. Furuta, *Performance Enhancements and Expanded Manufacturing Capacity for Commercial NAS Batteries*, NGK Insulators, LTD, presented at ESA (2003).

7. W. Fischer, *ABB NaS Battery Review and Preview*, Electrochemical Society Fall Meeting, Toronto (1992).

8. W. Fischer, *Status and Prospects of NaS High Energy Batteries*, 26th Annual IECEC Proceedings, **VI**, p. 80 Boston (1991).

9. J. Coetzer, *J. Power Sources*, **18**, 377 (1987)

10. C.-H. Dustmann, *ZEBRA Batteries Set to Take on the World*", Batteries International, July (1994)

11. A. V. Virkar, T. J. Armstrong, N. Weber, K-Z Fung and J-F Jue, *in High Temperature Material*", S. C. Singhal, Editor, PV 2002-5, The Electrochemical Society, Inc., Pennington, NJ (2002)

12. *Phase Diagrams for Ceramists: Volume II*, the American Ceramic Society, Westerville, OH (1969).

CHAPTER 3

A STUDY OF THE KINETICS OF CONVERSION OF ALPHA-ALUMINA + ZIRCONIA INTO SODIUM BETA" – ALUMINA + ZIRCONIA

3.1 Introduction

Sodium beta"-alumina is a nonstoichiometric sodium aluminate with an approximate composition – $Na_2O.\sim6Al_2O_3$, known for its excellent conductivity for sodium ions [1]. Even though the solid electrolyte is generally known as beta-alumina, there are two different crystal structures: beta-alumina and beta"-alumina. Both structures have a plane of sodium ions located between spinel blocks. Beta-alumina exists as a two-block structure and beta"-alumina as a three-block structure. The main difference in properties of beta and beta"-alumina is in the electrical resistivity, which is considerably lower for beta"-alumina compared to beta-alumina. The lower resistivity of beta"-alumina is attributed to differences in Na_2O content between beta" and beta-alumina ($Na_2O.\ \sim6Al_2O_3$ and $Na_2O.\sim11Al_2O_3$) since the former has a slightly higher soda content, and also differences in structure [2]. β"-alumina exhibits excellent conductivity at a relatively low temperature of 300°C compared to other known ion conductors as well: at 300°C the ionic resistivity (conductivity) of Na β"-alumina is ~3 Ωcm (~0.33 S/cm). By comparison, the ionic resistivity (conductivity) of YSZ at 800°C is ~30 Ωcm (~0.033 S/cm). At 300°C, the ionic conductivity of YSZ is orders of magnitude lower. The crystal

structure of sodium beta"-alumina provides a rigid framework with channels along which the mobile ionic species in the solid can migrate [3]. The rhombohedral structure of beta" is usually represented as a hexagonal unit cell with three times the volume of the rhombohedral cell. As mentioned earlier, the crystal structure consists of Al-O-Al spinel blocks, separated by conduction planes perpendicular to the c-axis (which is 1.5 times larger than beta-alumina) of the hexagonal unit cell [4]. The spinel blocks exhibit rotational symmetry about the c-axis and are held together by oxygen ions. Sodium ions are present in the conduction plane and ion transport involves hopping from site to site along these channels. Weber [5] furthered his studies on beta"-alumina and showed that small amounts of MgO or Li_2O can stabilize this phase so that it can be sintered into polycrystalline compacts. Because of its high Na^+ ion conductivity, sodium beta"-alumina is used as a solid electrolyte in electrochemical energy storage systems. As described in the previous chapter, one of the most advanced energy storage systems is based on Na β"-alumina solid electrolyte (BASE). The high temperature sodium sulfur battery, invented at Ford Motor Company during the nineteen sixties, has attractive features for such applications. The important features include low materials cost, good durability, high depth of discharge, and potentially low cost. Additionally, the thermodynamic stability of BASE against reduction or development of electronic conduction is far greater than that of oxygen ion conductors such as yttria-stabilized zirconia (YSZ). This presents an excellent opportunity to explore electrochemical energy conversion or storage devices using BASE.

The traditional method for the fabrication of sodium β"-alumina solid electrolyte (BASE) is by the calcination of a mixture of Na_2CO_3, Al_2O_3 and $LiNO_3$ in air, at ~1250^oC [6]. The calcined mixture is then compacted to form desired shapes and they are

sintered at a temperature of ~1600^{o}C. Sintering occurs by a transient liquid phase mechanism between beta-alumina and $NaAlO_2$. For sintering, the samples are encapsulated in either MgO crucibles or platinum bags in order to prevent the loss of Na_2O by evaporation. Finally, the sintered samples are annealed to ensure the complete conversion of β - alumina to sodium β"-alumina. There are several limitations to the traditional method of fabrication. Higher sintering temperature enhances soda loss from the samples, which can be avoided only by providing an expensive encapsulation of samples using Pt bags or MgO crucibles. Remnant sodium aluminate ($NaAlO_2$) which is hygroscopic in nature is present at the grain boundaries. Thus, beta"-alumina formed by this process is prone to moisture and CO_2 attack from the atmosphere and must be stored in vacuum chambers in order to avoid degradation. In addition, the strength of conventional beta"-alumina is low, typically on the order of 200 MPa or less due to the occurrence of exaggerated grain growth. A novel patented vapor phase process has been developed for the conversion of α-alumina into sodium beta"-alumina in order to circumvent the limitations mentioned above [7].

In the vapor phase process, α- alumina is exposed to a source of Na_2O, forming a thin layer of sodium β"-alumina on the surface of the exposed α- alumina. Since β"-alumina is a good conductor of Na^+ ions, diffusion of sodium ions through β"-alumina is fast. However, to form β"-alumina, it is necessary to incorporate Na_2O in the structure. Therefore, both sodium ions and oxygen ions must have reasonable diffusivities through the BASE for a vapor phase process. Once a surface layer of β" is formed, further conversion of alumina to β"-alumina practically shuts down due to the sluggish diffusion of O^{2-} ions through sodium beta"-alumina. The rate of diffusion of Na_2O (formation of β"-alumina) is dictated by the rate of diffusion of O^{2-} ions through β"-alumina. In fact,

Nicholson et al. [9,10] used the same approach as described above to form a thin layer of β"-alumina on sapphire crystals and the rate of film growth was very slow due to the slow diffusion rate of oxygen ions.

The process can be described as follows. The condition of electroneutrality must be met, which requires that the fluxes of Na^+ and O^{2-} be coupled. From the coupling of fluxes, the chemical diffusion coefficient of Na_2O through β"-alumina is given by,

$$\widetilde{D}_{Na_2O}^{\beta''} = \frac{D_{Na^+}^{\beta''} D_{O^{2-}}^{\beta''}}{D_{Na^+}^{\beta''} + 4D_{O^{2-}}^{\beta''}} \left(1 + \frac{\partial \ln \gamma_{Na_2O}}{\partial \ln X_{Na_2O}}\right) \tag{3.1}$$

where $D_{Na^+}^{\beta''}$ and $D_{O^{2-}}^{\beta''}$ are self-diffusivities of Na^+ and O^{2-} ions in β"-alumina, $\left(1 + \frac{\partial \ln \gamma_{Na_2O}}{\partial \ln X_{Na_2O}}\right)$ is the thermodynamic factor with γ_{Na_2O} and X_{Na_2O} being, respectively, activity coefficient and mole fraction of Na_2O in β"-alumina. Since O^{2-} ion diffusion is sluggish in β"-alumina, we can assume that $D_{Na^+}^{\beta''} >> D_{O^{2-}}^{\beta''}$. Thus, the above equation becomes,

$$\widetilde{D}_{Na_2O}^{\beta''} \approx D_{O^{2-}}^{\beta''} \left(1 + \frac{\partial \ln \gamma_{Na_2O}}{\partial \ln X_{Na_2O}}\right) \tag{3.2}$$

If the thermodynamic factor is assumed to be unity, the chemical diffusion coefficient of Na_2O is the same as the self diffusion coefficient of O^{2-} ions.

$$\widetilde{D}_{Na_2O}^{\beta''} \approx D_{O^{2-}}^{\beta''} \tag{3.3}$$

At a temperature of ~1400°C, if the diffusivity of O^{2-} ions in β"-alumina ($D_{O^{2-}}^{\beta''}$) is on the

order of 10^{-10}cm^2/sec, then the thickness of α-alumina that is converted to β"-alumina in two days will be ~50 microns. The slow kinetics is due to the slow transport of O^{2-} ions through β"-alumina.

In order to expedite the conversion process, a different approach is used wherein a rapid path is provided for the diffusion of O^{2-} ions [7]. This is done by incorporating an oxygen ion conductor, yttria stabilized zirconia (YSZ), in the starting material. Thus, a coupled diffusion of Na^+ and O^{2-} ions transport can occur in two phases, leading to a faster conversion of alumina to sodium beta"-alumina. Once a thin layer of beta"-alumina is formed on the surface, Na^+ ions diffuse through the formed beta"-alumina and O^{2-} ions through the YSZ present in the material. This process leads to the formation of a two-phase composite of BASE and zirconia.

From the condition of local electroneutrality and the coupling of fluxes, the chemical diffusion coefficient of Na_2O through β"-alumina /YSZ is given by,

$$\widetilde{D}_{Na_2O}^{\beta''/YSZ} = \frac{V_{YSZ}V_{\beta''}C_{O^{2-}}^{YSZ}\widetilde{D}_{O^{2-}}^{YSZ}\widetilde{D}_{Na^+}^{\beta''}}{C_{Na^+}^{\beta''}V_{\beta''}\widetilde{D}_{Na^+}^{\beta''} + 4DC_{O^{2-}}^{YSZ}V_{YSZ}\widetilde{D}_{O^{2-}}^{YSZ}} \tag{3.4}$$

where $\widetilde{D}_{O^{2-}}^{YSZ}$ and $\widetilde{D}_{Na^+}^{\beta''}$ are, respectively, the chemical diffusion coefficients of O^{2-} ions in YSZ and Na^+ ions in β"-alumina, $C_{Na^+}^{\beta''}$ is the concentration of Na^+ ions in β"-alumina, $C_{O^{2-}}^{YSZ}$ is the concentration of O^{2-} ions in YSZ, and $V_{\beta''}$ and V_{YSZ} are, respectively, the volume fractions of β"-alumina and YSZ. In the above equation, the concentration gradient of Na_2O corresponds to that in the BASE. If the thermodynamic factors are assumed to be unity, the chemical diffusion coefficients can be replaced by self-diffusivities of the corresponding ions. That is,

$$\widetilde{D}_{Na_2O}^{\beta''/YSZ} = \frac{V_{YSZ}V_{\beta''}C_{O^{2-}}^{YSZ}D_{O^{2-}}^{YSZ}D_{Na^+}^{\beta''}}{C_{Na^+}^{\beta''}V_{\beta''}D_{Na^+}^{\beta''} + 4C_{O^{2-}}^{YSZ}V_{YSZ}D_{O^{2-}}^{YSZ}} \tag{3.5}$$

Here, the diffusivities of O^{2-} ions in YSZ and Na^+ ions in Na β"-alumina are relatively comparable (a few orders of magnitude different). The above equations are derived under the assumptions that both phases are contiguous and parallel transport of oxygen through Na β"-alumina is negligible. Thus, the chemical diffusion coefficient of Na_2O through β"-alumina/YSZ is much greater than that through single phase β"-alumina. At a temperature of 1400°C, the thickness of α-alumina that is converted to β"-alumina in ~16 hours was ~1000 microns [8].

By choosing the composition of YSZ with a low yttria content, typically 3%, the two-phase composite can be fabricated with strength on the order of ~900 MPa, which is more than four times that of the conventional BASE. In the vapor phase process, no encapsulation is needed as the conversion temperature is relatively low (1450°C), resulting in negligible soda loss. Moreover, the process is carried out in such a way that the thermodynamic activity of Na_2O is significantly lower than the activity of Na_2O in $NaAlO_2$, preventing the formation of hygroscopic $NaAlO_2$ at the grain boundaries. The activity of Na_2O is controlled by the conversion temperature and composition. The BASE thus formed is resistant to atmospheric moisture and CO_2, and can even be boiled in water without any degradation.

3.2 Theoretical Model

Figure 3.1 shows a schematic of the conversion mechanism of a two-phase, contiguous compact of α -alumina + YSZ into a Na-β"-alumina + YSZ compact. The

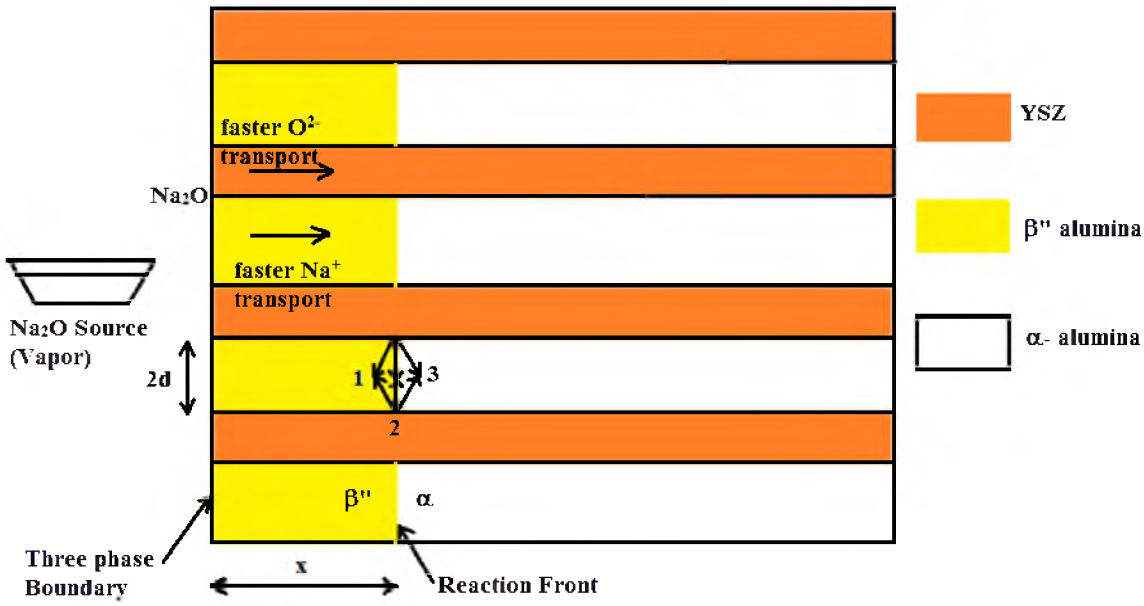

Figure 3.1 Mechanism of conversion of α – alumina to BASE. Oxygen ions are transported through YSZ and sodium ions are transported through β"-alumina. It also shows the three different paths through which O^{2-} ions can diffuse at the reaction front to form BASE.

schematic is depicted as alternate layers of alumina and YSZ for the sake of simplicity.

This assumption is reasonable because, in the actual microstructure of the two-phase material, both phases are contiguous. A theoretical model describing the conversion kinetics of α – alumina/3YSZ samples to sodium β" – alumina/3YSZ samples is given in what follows. The conversion was achieved using the patented vapor phase method [7] and the chemical reaction is as follows:

$$Na_2O + \sim 6.2Al_2O_3 \rightarrow Na_2O.\sim 6.2\ Al_2O_3 \qquad (3.6)$$

For conversion, a composite of α –alumina + YSZ is exposed to a vapor of Na_2O source at elevated temperatures. A surface layer is converted to Na β"-alumina + YSZ upon the incorporation of Na_2O. Subsequent conversion occurs by the coupled transport of Na^+ ions and O^{2-} ions through the ceramic. Sodium ions are transported through the already

formed layer of β”-alumina and oxygen ions are transported through YSZ.

The kinetics of conversion may be either interface controlled or diffusion controlled or a combination of both. Let x be the thickness converted to β”-alumina at time t. When the thickness converted is small, the kinetics should be linear (interface control) and when the thickness converted is large, the kinetics should be parabolic (diffusion control). The process of conversion to sodium β”-alumina can be broken down into three steps: interface reaction at the three-phase boundary (YSZ, Na β”-alumina, and gas phase), transport of ions across the bulk, and the formation of BASE at the reaction interface. Figure 3.2 shows a schematic of the variation of the chemical potential of Na_2O across the converted (β”-alumina + YSZ) thickness (x). During the conversion process, O^{2-} ions need to diffuse through BASE/α-alumina to combine with Na^+ ions to form BASE, which is a slow kinetic step. This can occur along three different paths: through the β”-alumina phase, along the interface, or through the α-alumina phase, as shown in Figure 3.1. It is expected to depend on the grain size of the sample as the diffusion distance of O^{2-} ions is half the grain size (d/2) of the sample, as shown in the schematic.

Na_2O is dissociated at the three-phase boundary (gas phase, β”-alumina, and YSZ) and Na^+ ions are transported through β”-alumina and O^{2-} ions are transported through YSZ, as shown in the schematic – Figure 3.1. The condition of electroneutrality must be satisfied, thus resulting in the fluxes of Na^+ and O^{2-} ions being coupled.

Assuming a quasi-steady state:

$$Na_2O \longrightarrow 2Na^+ (\beta'') + O^{2-} (YSZ) \tag{3.7}$$

Let the interface between the gas phase (Na_2O) and β”-alumina+YSZ layer be denoted by I and the interface between the reaction front (β”-alumina+YSZ) and α-alumina+YSZ be

denoted by II.

Assuming electroneutrality and a quasi-steady state, the fluxes of sodium ions and oxygen ions are related as follows.

$$\text{i.e.} \qquad J_{Na^+} = 2J_{O^{2-}} \tag{3.8}$$

and

$$J^{I}_{Na_2O} = J_{Na_2O} = J^{II}_{Na_2O} \tag{3.9}$$

The chemical potential of Na_2O on the gas phase side of interface I is $\mu_1 = \mu^{I}_{Na_2O}$

The chemical potential of Na_2O on the α-alumina/YSZ side of interface II is $\mu_2 = \mu^{II}_{Na_2O}$

At the gas solid interface (I) and reaction front (II), the flux of Na_2O is defined by

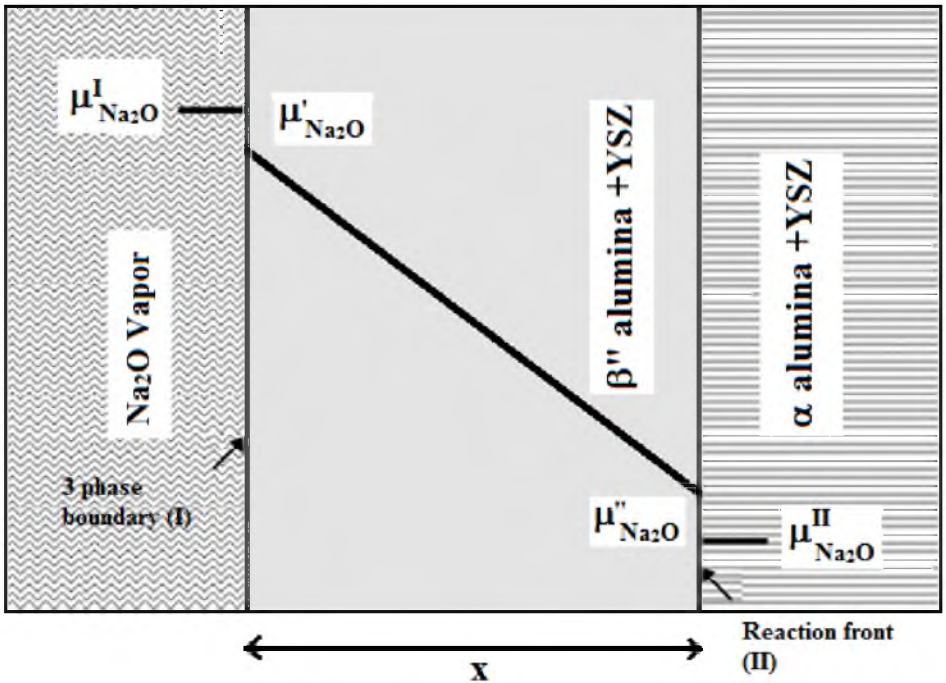

Figure 3.2 A schematic showing the variation of the chemical potential of Na_2O across the converted BASE with a thickness x. The process involves two interfacial steps and one diffusive (coupled) step.

the corresponding interfacial parameters. Across the converted thickness of β"-alumina +YSZ, flux of Na_2O is a function of the chemical diffusion coefficient and the concentration of Na_2O in β"-alumina and the gradient in chemical potential of Na_2O across the thickness.

$$J_{Na_2O} = K''\left(\mu'' - \mu^{II}_{Na_2O}\right) = K'\left(\mu^{I}_{Na_2O} - \mu'\right) = \frac{1}{V_m}\frac{dx}{dt} = \frac{\tilde{L}_{Na_2O}}{k_B T}\frac{(\mu' - \mu'')}{x} \qquad (3.10)$$

where K' and K" are the interfacial reaction coefficients at the gas-solid interface (interface I) and the reaction front (interface II), respectively. μ' is the chemical potential of Na_2O in β"-alumina/YSZ, close to the gas phase (Na_2O vapor) near interface I and μ" is the chemical potential of Na_2O in β"-alumina/YSZ, close to the reaction front (α-alumina/YSZ) near interface II.

V_m - Molar volume of BASE

$\tilde{L}_{Na_2O}$ - Chemical diffusion coefficient of Na_2O

C - Concentration of Na_2O in BASE

x – Thickness converted to β"-alumina at time t

k_B – Boltzmann constant

T – Temperature

Since the chemical potentials μ' and μ" are not measurable parameters, we need to eliminate them from the equations. From equation (3.10) we know that,

$$K''\mu^{II}_{Na_2O} - K''\mu'' = K'\mu' - K'\mu^{I}_{Na_2O}$$
$$\therefore \mu' = \frac{K''\left(\mu^{II}_{Na_2O} - \mu''\right)}{K'} + \mu^{I}_{Na_2O} \qquad (3.11)$$

We can eliminate μ' by substituting μ' in equation (3.10)

$$K''\left(\mu''^{II}_{Na_2O}-\mu''\right)=-K''\left(\mu''-\mu''^{II}_{Na_2O}\right)=\frac{\tilde{L}_{Na_2O}}{k_BTx}\left(\mu''-\frac{K''\left(\mu''^{II}_{Na_2O}-\mu''\right)}{K'}-\mu'^{I}_{Na_2O}\right) \tag{3.12}$$

or

$$-k_BTxK''(\mu''-\mu''^{II}_{Na_2O})=\frac{\tilde{L}_{Na_2O}}{K'}\left(K'\mu''-K''\mu''^{II}_{Na_2O}+K''\mu''-K'\mu'^{I}_{Na_2O}\right) \tag{3.13}$$

Rearranging,

$$-K'K''k_BTx\mu''+K'K''k_BTx\mu''^{II}_{Na_2O}=\tilde{L}_{Na_2O}(\quad\quad\quad

Simplifying equation (3.18),

$$\frac{K'K''\tilde{L}_{Na_2O\sim\cdots}(\mu^{II}_{Na_2O}-\mu^{I}_{Na_2O})}{\tilde{L}_{Na_2O\sim\cdots}(K'+K'')+K'K''k_BTx}=\frac{1}{V_m}\frac{dx}{dt} \tag{3.19}$$

or

$$K'K''\tilde{L}_{Na_2O\sim\cdots}(\mu^{II}_{Na_2O}-\mu^{I}_{Na_2O})V_m\cdots\left[\tilde{L}_{Na_2O\sim\cdots}\cdots\cdots K''k_BTx\right]dx \tag{3.20}$$

or

$$\frac{\tilde{L}_{Na_2O\sim\cdots}(K'+K'')}{K'K''\tilde{L}_{Na_2O\sim\cdots}(\mu^{II}_{Na_2O}-\mu^{I}_{Na_2O})V_m}dx+\frac{K'K''k_BTx}{K'K''DC(\mu^{II}_{Na_2O}-\mu^{I}_{Na_2O})V_m}dx=dt \tag{3.21}$$

On integration,

$$\int_0^x\frac{(K'+K'')}{K'K''(\mu^{II}_{Na_2O}-\mu^{I}_{Na_2O})V_m}dx+\int_0^x\frac{k_BT}{\tilde{L}_{Na_2O\sim\cdots}(\mu^{II}_{Na_2O}-\mu^{I}_{Na_2O})V_m}xdx=\int_0^t dt \tag{3.22}$$

$$\therefore\frac{(K'+K'')x}{K'K''(\mu^{II}_{Na_2O}-\mu^{I}_{Na_2O})V_m}+\frac{k_BTx^2}{2\tilde{L}_{Na_2O\sim\cdots}(\mu^{II}_{Na_2O}-\mu^{I}_{Na_2O})V_m}=t \tag{3.23}$$

The general equation is

$$\frac{k_BT}{2\tilde{L}_{Na_2O\sim\cdots}(\mu^{II}_{Na_2O}-\mu^{I}_{Na_2O})V_m}x^2+\frac{(K'+K'')}{K'K''(\mu^{II}_{Na_2O}-\mu^{I}_{Na_2O})V_m}x=t \tag{3.24}$$

This general equation describes the kinetics of conversion in terms of measurable (in principle) parameters. Here, time t is defined as the hold time at the conversion temperature. So at t = 0, there will be an initial thickness converted (x_o) as some conversion takes place during the heating up process. On integrating from x_0 to x instead

of 0 to x, the general equation is

$$\frac{k_B T}{\tilde{L}_{Na_2O}(\mu^{II}_{Na_2O}-\mu^{I}_{Na_2O})V_m}(x^2-x_0^2)+\frac{(K'+K'')}{K'K''(\mu^{II}_{Na_2O}-\mu^{I}_{Na_2O})V_m}(x-x_0)=t \tag{3.25}$$

Consider a case where the conversion thickness x is very small. In a typical experiment, the initial thickness x_o may not be negligible due to the occurrence of conversion during the heating up process. If we assume x_o to be negligible and if the diffusion distance of the coupled transport of sodium and oxygen ions across the β"-alumina layer is very small, then,

$$\frac{(K'+K'')}{K'K''}x >> \frac{k_B T}{2\tilde{L}_{Na_2O}}x^2$$

We have

$$\frac{(K'+K'')x}{K'K''(\mu^{II}_{Na_2O}-\mu^{I}_{Na_2O})V_m} \cong t \tag{3.26}$$

$$x=\frac{K'K''}{(K'+K'')}\left(\mu^{II}_{Na_2O}-\mu^{I}_{Na_2O}\right)V_m t \tag{3.27}$$

$$x=K_{\text{int}}\left(\mu^{II}_{Na_2O}-\mu^{I}_{Na_2O}\right)V_m t \tag{3.28}$$

where $K_{\text{int}}=\frac{K'K''}{K'+K''}$ which includes both interfacial reactions at the gas phase interface (I) and reaction front interface (II). The kinetics is thus interface controlled.

Effective interfacial coefficient can be defined as,

$$K_{eff} = K_{\text{int}}(\mu^{II}_{Na_2O} - \mu^{I}_{Na_2O})V_m = \frac{K'K''}{(K'+K')}(\mu^{II}_{Na_2O} - \mu^{I}_{Na_2O})V_m \tag{3.29}$$

Then,

$$x \approx K_{eff}t \tag{3.30}$$

Here, the conversion process is controlled by the two interface reactions at gas phase (I) and reaction front (II) since the diffusion distance is very small for the diffusion across β"-alumina. Thus, the process follows linear kinetics or it is interface controlled.

Consider a case where the conversion thickness x is large. In this case, the diffusion distance of sodium and oxygen ions across the β"-alumina/YSZ converted layer is large. That is,

$$\frac{(K'+K'')}{K'K''}x << \frac{k_BT}{2\tilde{L}_{Na_2O\sim}} \quad x^2,$$

Thus,

$$\frac{k_BTx^2}{2\tilde{L}_{Na_2O\sim}(\mu^{II}_{Na_2O} - \mu^{I}_{Na_2O})V_m} \cong t \tag{3.31}$$

$$\therefore x^2 = \frac{2\tilde{L}_{Na_2O\sim}(\mu^{II}_{Na_2O} - \mu^{I}_{Na_2O})V_m}{k_BT}t \tag{3.32}$$

Effective diffusion coefficient can be defined as

$$D_{eff} = \frac{2\tilde{L}_{Na_2O\sim}(\mu^{II}_{Na_2O} - \mu^{I}_{Na_2O})V_m}{k_BT} \tag{3.33}$$

Thus,

$$x^2 \approx D_{eff} t \tag{3.34}$$

In this case, the conversion process is controlled by the diffusion step since the diffusion distance is large and the two interface reactions are relatively fast. Thus, the process follows parabolic kinetics or it is diffusion controlled.

The general form of the equation derived can be written in terms of effective coefficients of diffusion and interfacial reactions as follows.

$$x^2\left(\frac{1}{D_{eff}}\right) + x\left(\frac{1}{K_{eff}}\right) - \left(\frac{x_0}{D_{eff}} + \frac{1}{K_{eff}}\right)x_0 = t \tag{3.35}$$

3.3 Experimental Procedure

A mixture of 70 vol. % α-Al_2O_3 and 30 vol. % 3–YSZ (Baikowski CR–30 and Tosoh TZ-3Y, respectively) was prepared by planetary milling to ensure a well-mixed, fine starting powder. Several α-alumina+3YSZ discs were prepared by die-pressing followed by isostatic pressing. These samples were then sintered at different temperatures and for different durations: temperatures ranging from 1500°C to 1800°C and durations from 1 hour to 4 hours. The densities of the samples were determined. The samples sintered at different temperatures were fine–polished, thermally etched, and analyzed under a Scanning Electron Microscope to determine the grain sizes of the samples. These samples were then converted to sodium β" – alumina+3YSZ by heat treating them at different temperatures ranging between 1250°C and 1450°C and durations ranging from 1 hour to 15 hours. The converted samples were cross-sectioned, coarsely polished, and examined again under a Scanning Electron Microscope to measure the thickness of the sample converted and for calculating the corresponding conversion rates. Some of the

partially converted samples were cross-sectioned, finely polished, and analyzed under the microscope to study the microstructure of the reaction interface between the converted and the unconverted regions of the samples. The kinetics of conversion at various conversion temperatures ranging between 1250°C and 1450°C was studied and the theoretical model proposed was fitted to the experimental data to determine the various parameters.

3.4 Results and Discussion

The α-alumina+YSZ samples, sintered at different temperatures ranging from 1500°C/1 hour to 1800°C/3 hours, were examined using a Scanning Electron Microscope. Figures 3.3 (a) through (d) show the microstructures of sintered samples with widely differing grain sizes: α-alumina + 3YSZ samples sintered at 1500°C, 1600°C, 1700°C, and 1800°C, respectively. The grey areas are alumina and the white areas are YSZ.

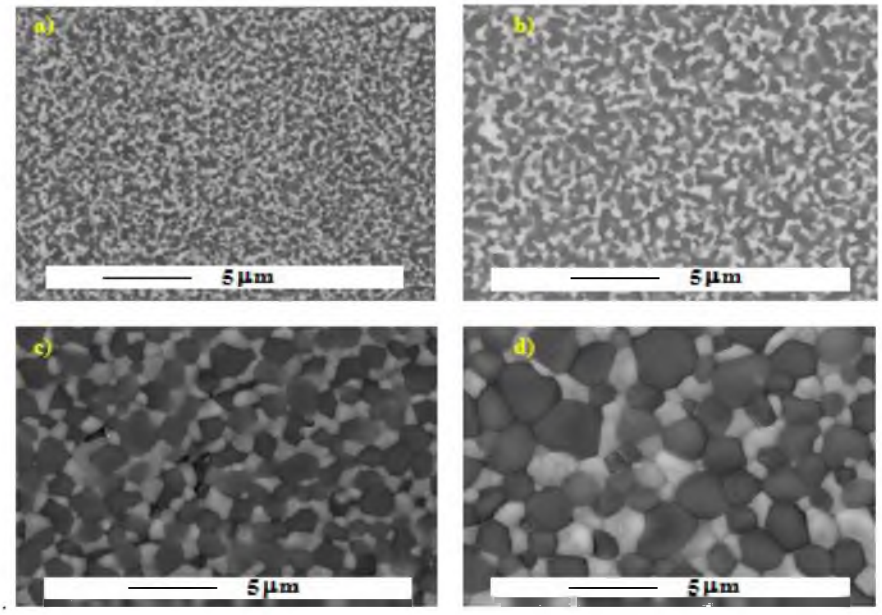

Figure 3.3 Microstructures of α-alumina + 3YSZ samples sintered at (a) 1500°C for 1 hour, (b) 1600°C for 1 hour, (c) 1700°C for 1 hour, and (d) 1800°C for 1 hour.

The grain size is considerably greater in the samples sintered at higher temperatures and for longer times. The average grain sizes of the samples were determined using Schwartz – Saltykov diameter analysis [11]

Table 3.1 lists the grain size as a function of sintering conditions. The grain size (average of alumina and zirconia) of the sample sintered at 1500°C/1 hour was 0.53 μm and that of the sample sintered at 1800°C/3 hours was 4.15 μm. The growth in grain size was about 8 times when the temperature/time were increased from 1500°C/1 hour to 1800°C/3 hours. This result is consistent with the expectations since the sample sintered at higher temperature and for longer time exhibits a larger grain size. Figure 3.4 (a) shows a micrograph of the cross-section of a partially converted β"-alumina sample. In the figure, interface A shows the actual chemical interface where α-alumina/YSZ changes to β"-alumina+YSZ and interface B shows the structural interface where damaged β"-alumina+YSZ changes to a dense β"-alumina+YSZ structure. At the chemical interface (A), the microstructure of the sample changes abruptly from α-alumina+YSZ to β"-alumina+YSZ. Even though the actual chemical interface is at A, there is an interface band between A and B which has the same structure as that of β"-alumina+YSZ with the exception of porosity/cracks. When α-alumina+YSZ sample is converted to β"-alumina+YSZ, there will be a volume change due to differences in their densities (density of α-alumina: 3.97 g/ml and that of beta"-alumina: 3.28 g/ml) and due to the incorporation of Na_2O in the structure.

Consider 1 mole of α-alumina converted to 1 mole of Na β"-alumina.

Volume of 1 mole of α-Al_2O_3 = (102g/3.97 g/ml) = 25.69 ml

Volume of 1 mole of β"-alumina, (1/6.2) $Na_2O.Al_2O_3$ = (112g/3.28) =34.15 ml

The net volume change is

Table 3.1: Grain size as a function of sintering conditions

Sintering Temperature (^{o}C)	Hold time (hours)	Grain Size (um)
1500	1	0.53 ± 0.03
1500	2	0.57 ± 0.04
1500	4	0.61 ± 0.05
1550	1	0.67 ± 0.01
1550	2	0.74 ± 0.05
1550	4	0.86 ± 0.07
1600	1	0.95 ± 0.01
1600	2	1.14 ± 0.03
1600	4	1.32 ± 0.03
1700	1	1.80 ± 0.02
1700	3	2.40 ± 0.04
1800	1	3.70 ± 0.06
1800	3	4.15 ± 0.05

$$\frac{34.15-25.69}{25.69}\times 100 = 32.93\%$$

This volume change needs to be accommodated in the material. Figure 3.4 (a) shows that significant cracking/porosity occur in the structural interface band. The reaction front undergoes a change in microstructure by repairing the pores formed and densifying beta"-alumina+YSZ. This is evident from Figure 3.4 (b), which is a chemical line scan profile across the cross-section of the partially converted sample which shows the weight percent of sodium with distance. Concentration of sodium in the unconverted portion is negligible, whereas the concentration of sodium in the converted portion (β"-

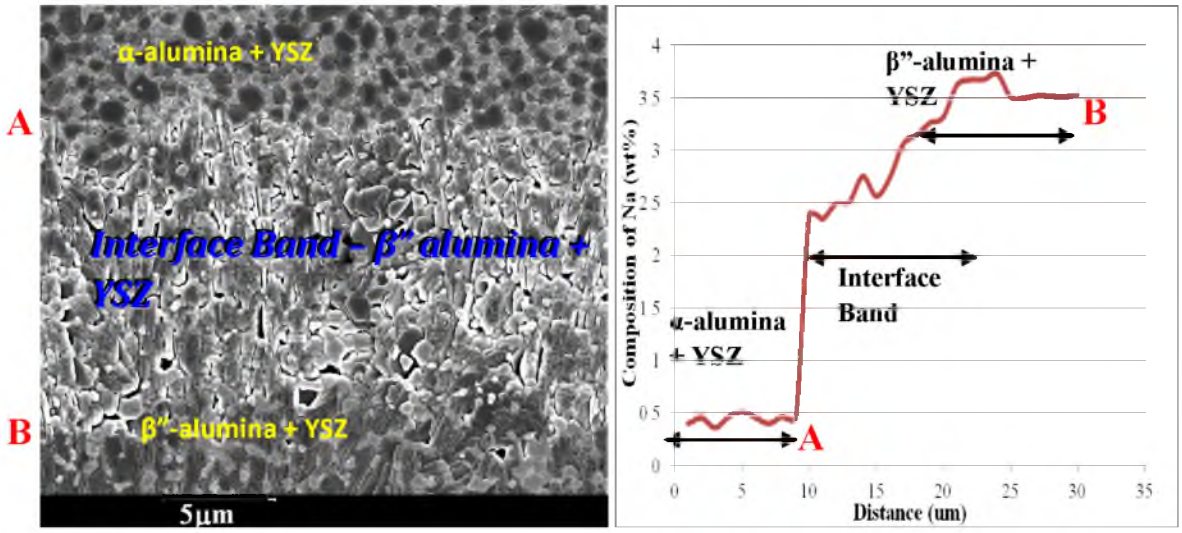

(a) (b)

Figure 3.4 Analysis of the interface of partially converted sample. (a) Micrograph of the interface of the partially converted α – alumina+3YSZ sample which shows the unconverted portion in the top and the interface band in the middle and the converted portion in the bottom. The interface band has the structure of β"-alumina + YSZ but with porosity. (b) Chemical line scan shows the weight percent of sodium present across the cross-section of the sample. The concentration of sodium in the unconverted portion (α-alumina+YSZ) is negligible as compared to that in the interface band and the converted portion (β"-alumina+YSZ), which is an order of magnitude higher.

alumina+YSZ) is ~3.7 (wt) %.

At the chemical interface A, there is a sharp change in the concentration of sodium (0.5% to 2.5%), which is consistent with the change in structure from α-alumina+YSZ to β"-alumina+YSZ. However, across the interface band (between A and B), right after the sharp increase in sodium concentration, the sodium concentration further increases gradually as it nears the fully densified β"-alumina+YSZ at interface B. This may be attributed to the presence of porosity in the interface band. When the structure changes from α-alumina to β"-alumina, the incorporation of Na_2O in the structure is accompanied by structural damage, which creates pores. As the structure rearranges and repairs itself to form a dense β"-alumina, the porosity gradually decreases through the interface band as the sample becomes dense β"- alumina. An order of

magnitude analysis of the concentration profile through the interface band is given below.

Let $V_{\beta}^{'}, V_{Z}^{'}$, and $V_{P}^{'}$ be the volume fractions of β"-alumina, YSZ, and porosity, respectively, at the chemical interface and $V_{\beta}^{"}, V_{Z}^{"}$, and $V_{P}^{"}$ be the volume fractions of β"-alumina, YSZ, and porosity, respectively, at the dense β"-alumina (B interface).

Then we have,

$$V_{\beta}^{'} + V_{z}^{'} + V_{P}^{'} = 1 \tag{3.36}$$

$$V_{\beta}^{"} + V_{z}^{"} + V_{P}^{"} = 1 \tag{3.37}$$

Since the sample is considered fully dense at the structural interface, $V_{P}^{"}$ is essentially zero.

i.e., $$V_{\beta}^{"} + V_{z}^{"} = 1 \tag{3.38}$$

The starting composition of the sample before conversion was 70 vol.% of α-alumina and 30 vol.% of YSZ. During conversion, YSZ remains unchanged. Thus, the volumes of fully converted sample are 75.77 vol.% β"-alumina and 24.23 vol.% YSZ. Thus,

$$\frac{V_{\beta}^{'}}{V_{z}^{'}} = \frac{V_{\mu}^{"}}{V_{z}^{"}} = \frac{0.7577}{.2423} = 3.127$$

i.e. $$V_{\beta}^{'} = 3.127 * V_{z}^{'} \tag{3.39}$$

Substituting equation (3.39) into equation (3.36)

$$3.127V_{z}^{'} + V_{z}^{'} + V_{P}^{'} = 1 \tag{3.40}$$

From Figure 3.4(b), the ratio of sodium concentrations at the chemical interface and converted β"-alumina is $\frac{2.5}{3.5} = 0.714$.

i.e., $\frac{V_\beta^{'}}{V_\beta^{''}} = 0.714 \qquad \therefore V_\beta^{'} = 0.714 * V_\beta^{''} = 0.714 * 0.7577 = 0.541$ (3.41)

From equation (3.39), we can determine $V_Z^{'}$

$$V_Z^{'} = \frac{0.541}{3.127} = 0.173 \tag{3.42}$$

Therefore, the porosity in the structural interface band can be calculated from equation (3.40) as

$$V_P^{'} = 1 - 0.541 - 0.173 = 0.286 \tag{3.43}$$

Thus, the porosity at the chemical interface is calculated to be 28.6%. No separate measurements of porosity in the interface band have been made. The net volume change of the sample when converted from α-alumina+YSZ to β"-alumina+YSZ was calculated to be 32.93%. From the microstructure of the sample cross-section, it is hard to determine the variation of porosity from interface A to B. The porosity is expected to decrease from interface A to B as the structure repairs itself to form a dense β"-alumina+YSZ.

As mentioned earlier in this chapter, the conversion to β"-alumina involves three kinetic steps: two interface reactions and one diffusion step. Interface reaction kinetics is expected to depend upon the average grain size of the sample. At the reaction front (K"), O^{2-} ions must transport through either the BASE formed, or through the α-alumina, or along the α-alumina+BASE interface (see schematic in Figure 3.1). The diffusion

distance is about half the grain size of α-alumina (or BASE). Since the grain size in a given sample is constant, this diffusion distance is fixed. Thus, diffusion distance parallel to α + YSZ/ β" + YSZ remains fixed throughout the conversion. This reflects as an interfacial step. The three paths for diffusion are in parallel, and the phenomenon is very similar to the formation of pearlitic steel by a cellular decomposition of austenite in the iron-carbon system. Thus, the local diffusion distance at the reaction front is larger for coarse grained samples and is smaller for fine grained samples. Thus, the interface kinetic parameter K" is expected to be an inverse function of grain size.

At the gas phase-solid interface (K') as well, the kinetics depends upon the grain size of the sample. At this interface, Na_2O dissociates to form Na^+ and O^{2-} where the three phases (gas phase, β"-alumina, and YSZ) meet. $2Na^+$ ions transport through β"-alumina and O^{2-} transport through YSZ. Figure 3.5 shows a schematic representation of the three phase boundaries of samples with small average grain size and large average grain size for comparison. The stars in the schematic show the number of three-phase boundaries with gas phase (Na_2O vapor), α or β"-alumina, and YSZ. Since the reaction occurs only at the three-phase boundaries, the kinetics of this interface reaction is proportional to the number of points where all the three phases meet. The smaller the average grain size, the larger the number of three-phase boundaries. Thus, the interfacial kinetics at the three-phase boundaries is also expected to be an inverse function of grain size.

The effect of grain size on diffusion coefficient can be hypothesized using the Brick-Layer model [12]. According to the Brick-Layer model, it can be shown that the ionic conductivity of BASE is a function of grain size; the larger the grain size, the higher the conductivity. The resistivity of a β"-alumina sample depends on the resistivity of

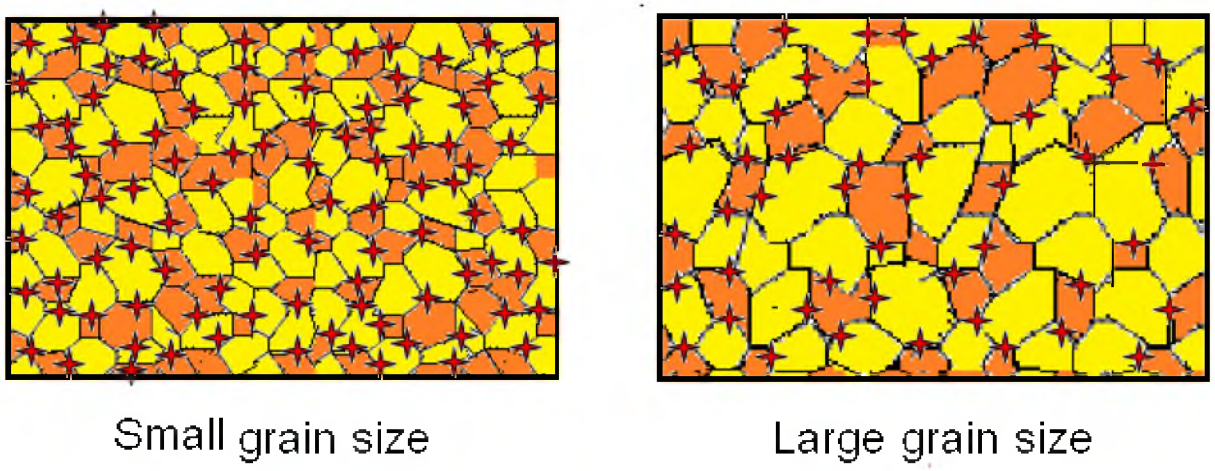

Figure 3.5 Schematic of three-phase boundaries (gas phase, α or β”-alumina, and YSZ) – smaller grain size and larger grain size

grain and grain boundary. The dependence is as shown below.

Resistance $R = R_g + R_{gb} + R_g + R_{gb} + \ldots$

Resistivity of β”-alumina, $\rho_{\beta''} = \rho_g + \frac{1}{d}\left(\lambda \rho_{gb} \delta_{gb}\right)$

where ρ_g - resistivity of grain

d – average grain size

λ – geometrical constant

ρ_{gb} - resistivity of grain boundary

δ_{gb} - grain boundary thickness

Thus, the resistivity of β”-alumina is an inverse function of the grain size. The above equation holds good for both β”-alumina and YSZ. Therefore, the conductivity/diffusivity in β”-alumina/YSZ is expected to increase with increase in grain size. Hence, the expectation is that the effective diffusivity of β”–alumina+YSZ may increase with increase in grain size. However, this model is mainly applicable to samples at lower temperatures (200°C – 700°C). It has been observed that typically, the effect of

grain size on conductivity is negligible at higher (>700°C) temperatures. The temperature range studied here was between 1250°C and 1450°C. Thus, the effect of grain boundary resistance in the current study is negligible. Therefore, the diffusion coefficient is expected to be independent of the grain size of the sample.

In the vapor phase conversion process, the approach to making samples of varying grain sizes involved the fabrication of α-alumina+YSZ samples by sintering at different temperatures and times. This was achieved by sintering α-alumina+YSZ samples at different temperatures ranging from 1500°C to 1800°C for various durations ranging between 1 hour and 4 hours. These samples were then converted to sodium beta"-alumina+YSZ at different temperatures ranging between 1250°C and 1450°C and hold times varying from 1 hour to 15 hours. The samples were cross-sectioned and analyzed to determine the rate of conversion from α-alumina to β"-alumina. The experimental data obtained were fitted to the general kinetics equation given in equation (3.35) using MATLAB software. Figure 3.6 shows the thickness of conversion of samples with varying grain sizes as a function of hold time at a conversion temperature of 1250°C. Figure 3.7 shows the conversion kinetics of samples with varying grain sizes as a function of hold time at a conversion temperature of 1450°C. The dependence of conversion thickness on time was fitted using the general equation: $\frac{\left(x^2 - x_0^2\right)}{D_{eff}} + \frac{\left(x - x_0\right)}{K_{eff}} = t$. In both sets of plots (Figures 3.6 and 3.7), non-zero y-intercepts (x_0) exist, which indicate that some conversion of α-alumina+YSZ to β"-alumina+YSZ occurs during the initial heat up. x_0 depends on the conversion temperature and grain size of the samples. For higher temperatures and smaller grain sizes, x_0 is large and for lower temperatures and larger grain sizes, x_0 is small. This is as expected because

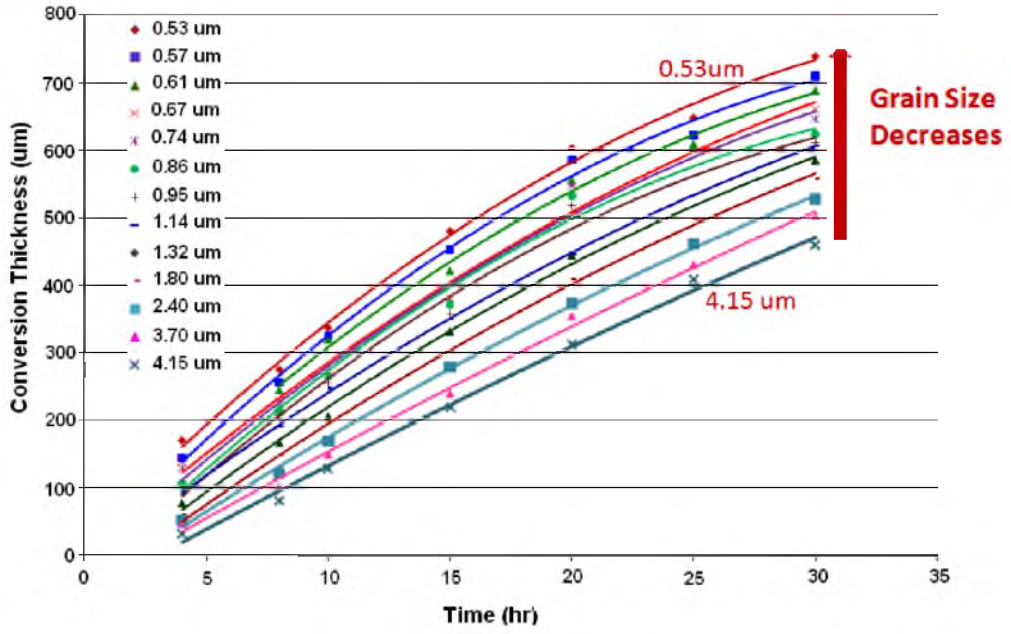

Figure 3.6 Conversion Thickness as a function of hold time for the samples with varying grain sizes, Conversion Temperature – 1250°C. The dependence was fitted to the general kinetic equation modeled for conversion: $\frac{\left(x^2 - x_0^2\right)}{D_{eff}} + \frac{\left(x - x_0\right)}{K_{eff}} = t$

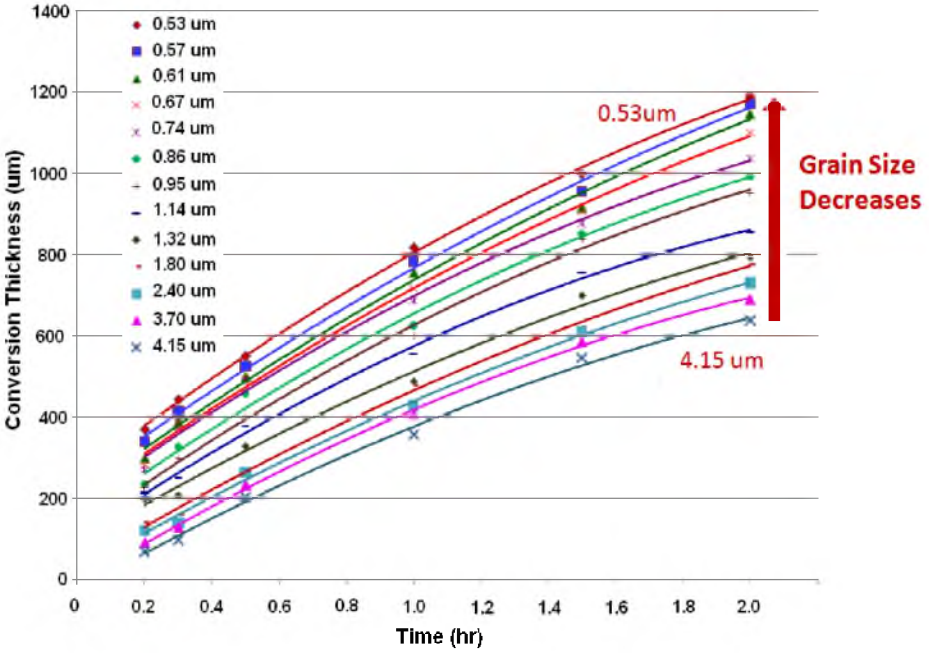

Figure 3.7 Conversion Thickness as a function of hold time for the samples with varying grain sizes, Conversion Temperature – 1450°C. The dependence was fitted to the general kinetic equation modeled for conversion: $\frac{\left(x^2 - x_0^2\right)}{D_{eff}} + \frac{\left(x - x_0\right)}{K_{eff}} = t$.

as the grain size increases, the rate of conversion decreases at a constant conversion temperature, whereas the rate of conversion increases with increase in the conversion temperature. At the conversion temperature of 1450°C, it was found that for the 1500°C/1 hour sample (average grain size – 0.53 μm), the rate of formation of β"-alumina was about 0.23μm/sec, whereas for the 1800°C/1 hour sample (average grain size – 3.7 μm), the rate of formation of β"-alumina was about 0.06μm/sec. Therefore, a sample of thickness 1mm, sintered at 1500°C for 1 hour will require ~35 minutes to convert completely to beta"-alumina at a temperature of 1450°C. For a 1mm thick sample sintered at 1800°C for 1 hour, the time required for complete conversion to β" – alumina will be about 140 minutes (~ 2 hours 20 minutes) when heat treated at 1450°C. This result indicates that the rate of conversion is higher for the samples having a smaller grain size. It was observed that the kinetics of conversion was linear (interface controlled) when the conversion thickness x is small and the conversion kinetics exhibited inverse dependence on grain size – the smaller the grain size, the faster the conversion rate. These results can be explained in terms of transport mechanisms.

Over the range of conversion thicknesses studied, which are well over 1 mm, it is observed that the kinetics is nearly linear when x is small. The observation that the kinetics is linear at small x implies the kinetics is not controlled by the parallel diffusion of Na^+ through the BASE formed and O^{2-} through the zirconia phase to the reaction front, even though conversion requires coupled transport of Na^+ and O^{2-}. That is, the diffusion step is relatively fast. With the available experimental data and the best fit obtained using the theoretical model, the effective diffusion and interfacial rate constants were determined. Figures 3.8 and 3.9 show the dependence of both interfacial rate constants and diffusion coefficients as a function of grain size for conversion temperatures of

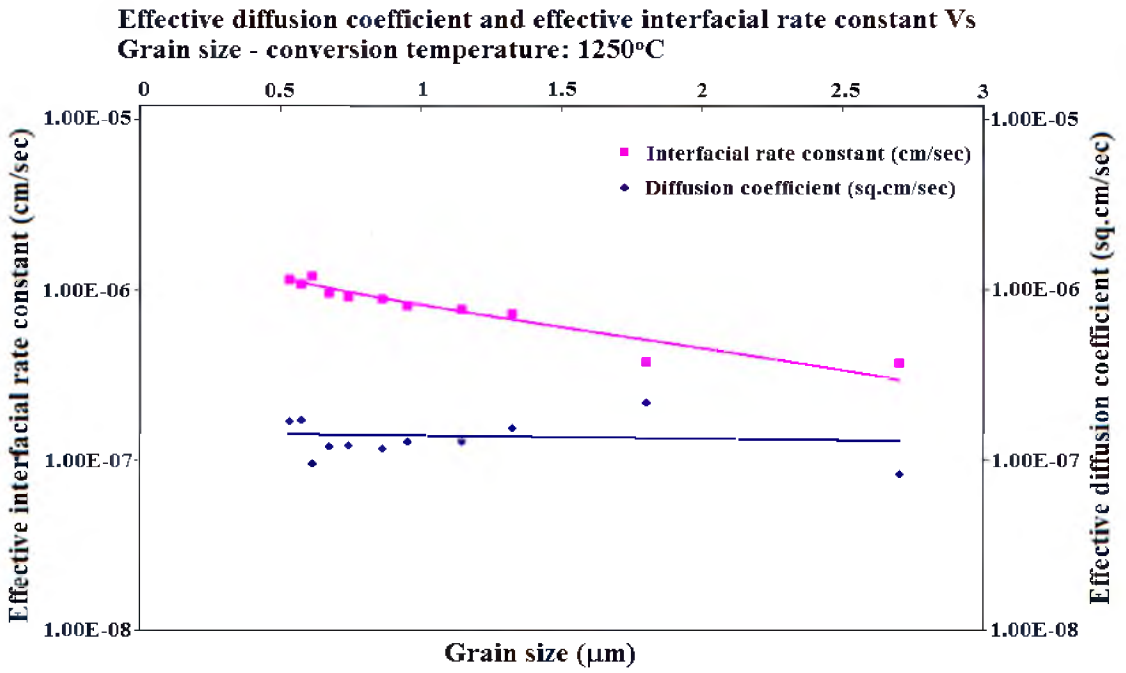

Figure 3.8: Effective diffusion and interfacial rate constants as a function of grain size for a conversion temperature of 1250°C. Dependence of diffusion coefficients with respect to grain size is negligible as compared to that of interfacial rate constants.

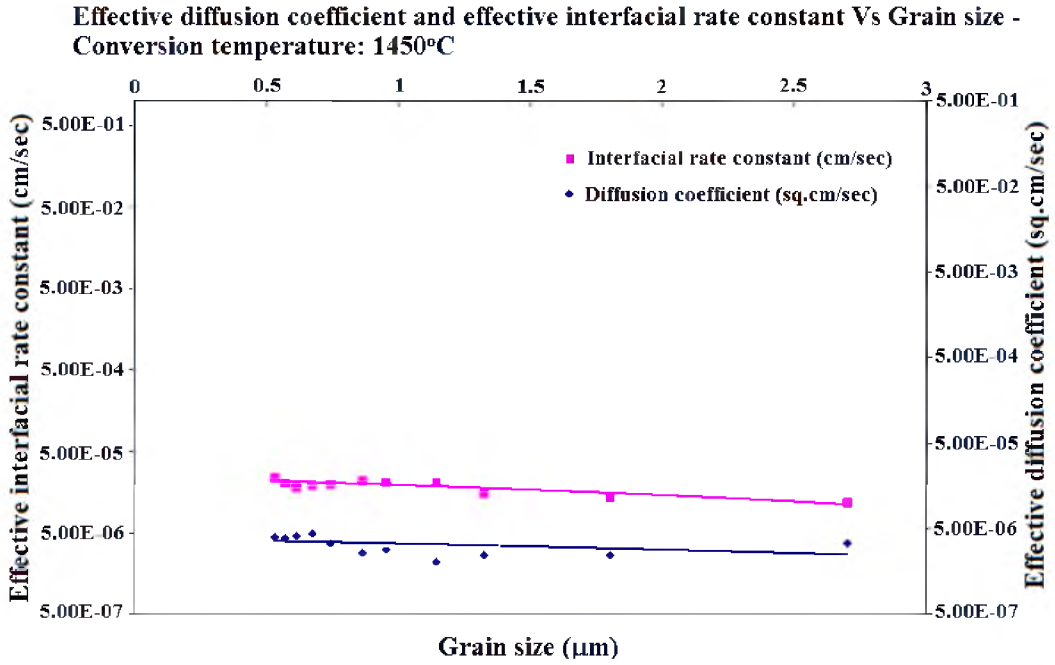

Figure 3.9: Effective diffusion and interfacial rate constants as a function of grain size for a conversion temperature of 1450°C. Dependence of diffusion coefficients with respect to grain size is negligible as compared to that of interfacial rate constants. The effective interfacial rate constant decreases slightly as grain size increases.

1250°C and 1450°C, respectively. At 1250°C, the effective interfacial rate constant (K_{eff}) decreases with increase in grain size, whereas the effective diffusion coefficient (D_{eff}) is essentially independent of grain size. Similarly at 1450°C, K_{eff} decreases slightly with increase in grain size and dependence of D_{eff} with grain size is negligible. According to the Brick-Layer model [12], D_{eff} is expected to increase with increase in grain size, as discussed earlier. However, the effect of grain boundary resistance is more prominent only at lower temperatures and is negligible at higher temperatures. In the present study, since the conversion temperatures are high, it may not affect the diffusion coefficients of the sample. At 1250°C, the ratio of diffusion coefficients between smallest and largest grain size is 1.49 and at 1450°C, the corresponding ratio is 1.2. However, the variation of interfacial rate constants with grain sizes is significant for both conversion temperatures. The ratio of interfacial rate constants between smallest and largest grain size at 1250°C is 3.3 and at 1450°C is 2.0. In both cases, the dependence at higher conversion temperature is less prominent than that at lower temperature. This is evident from Figures 3.10 and 3.11, which show the Arrhenius plots of interfacial and diffusion rate constants, respectively, of the samples with different grain sizes.

The activation energies corresponding to each of the grain sizes were calculated. The activation energies for diffusion varied between 328 kJ/mol and 340 kJ/mol, whereas the activation energies for interfacial reaction varied between about ~290 kJ/mol and ~350 kJ/mol with increasing grain sizes. That is, for smaller grain size samples, the activation energy for interfacial reactions is smaller and vice versa. Thus, the interface kinetics tends to be more sluggish for large grain size samples.

Figure 3.12 shows the dependence of activation energies corresponding to interface

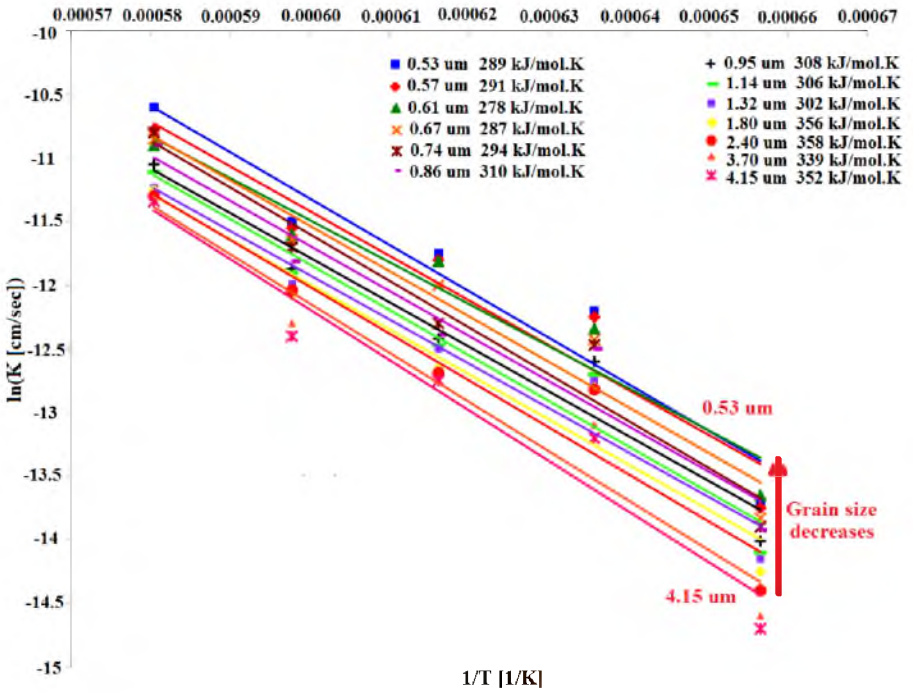

Figure 3.10 Arrhenius plot of interfacial rate constants for different grain sizes of the β" – alumina samples. As grain size decreases, the activation energy of interfacial reactions also decreases. It suggests that interfacial kinetics is dependent on grain size variation.

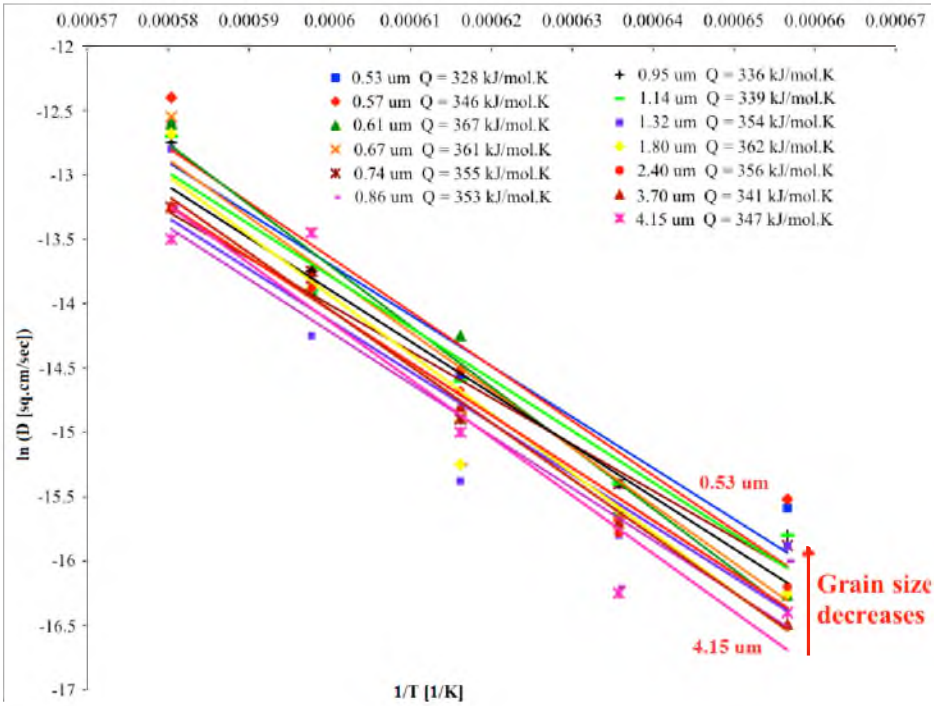

Figure 3.11 Arrhenius plots of diffusion constants for different grain sizes of the β" – alumina samples. As grain size decreases, the activation energy of diffusion reactions remains constant. This suggests that the diffusion kinetics is independent of grain size variation.

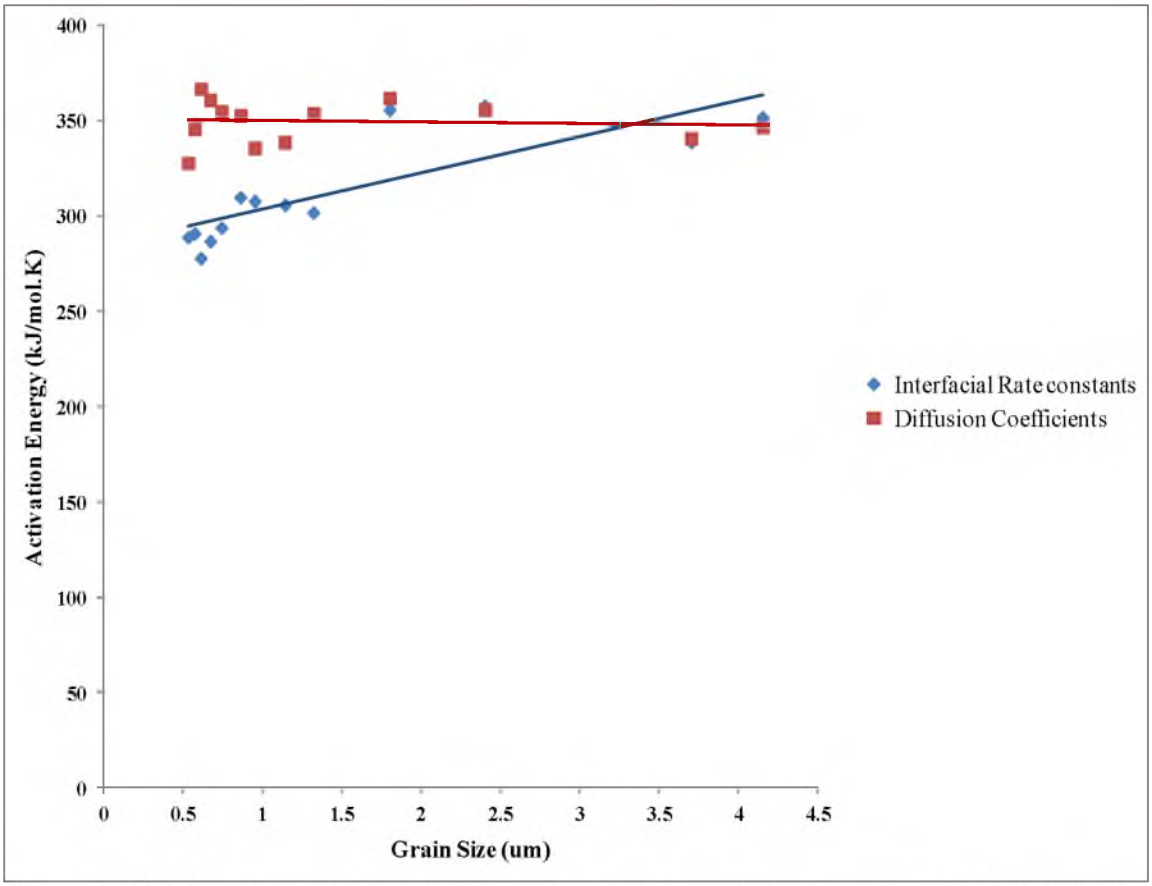

Figure 3.12 Variation of activation energies of interfacial rate constants and diffusion coefficients with grain size. Activation energy for interfacial reaction increases with increase in grain size, whereas activation energies of diffusion coefficient is independent of grain size variations.

reaction and diffusion for various grain size samples. Activation energies for interface reaction increase with increase in grain size, whereas activation energies for diffusion step are independent of the grain size variation. The dependence of diffusion constants on the grain sizes was not very substantial as compared to the dependence of interfacial rate constants on the grain sizes of the samples.

3.5 Summary

The kinetics of conversion of α-alumina/YSZ to Na β”-alumina/YSZ was studied. A novel patented vapor phase method was used to fabricate Na β”-alumina samples. In

order to expedite the diffusion of Na_2O through the samples, an oxygen ion conductor was incorporated in the starting α-alumina samples. This provided a rapid parallel path for the transport of O^{2-} ions as β"-alumina is a poor conductor of oxygen ions. A theoretical model was proposed and a general kinetic equation for conversion was formulated with diffusion and interfacial parameters. Several samples of various grain sizes from 0.53 μm to 4.15 μm were fabricated. These samples were converted to β"-alumina at several temperatures and for various times ranging from 1250°C to 1450°C and 1 hour to 15 hours. The effective diffusion and interfacial rate constants were determined from the experimental data and the proposed theoretical model. It showed that when the thickness converted is small, the kinetics is linear (interface controlled) and when the thickness converted is large, the kinetics is parabolic (diffusion controlled). The results also indicated that the smaller the grain size, the faster the rate of conversion. Arrhenius plots of interfacial and diffusion reactions showed that interfacial reactions at the three-phase boundaries and reaction front depended more on grain size than the actual diffusion of Na_2O through the sample (Na^+ through β"-alumina and O^{2-} through YSZ).

3.6 Acknowledgements

This work is supported by the US Department of Energy under Grant Number DE-FG02-06ER46086.

3.7 References

1. P. T. Mosley, *The solid electrolyte: properties and characteristics,* p. 19, in '*The sodium-sulfur battery*', J. L. Sudworth and A. R. Tilley,Editors, Chapman and Hall, London (1985).

2. J. T. Kummer, "*β-alumina electrolytes*", p. 141, in '*The sodium-sulfur battery*', J. L, Sudworth and A. R. Tilley, Editors, Chapman and Hall, London (1985).

3. G. Yamaguchi, and K. Suzuki, *Bull. Chem. Soc. Japan,* **41**, 93 (1968).

4. G. Yamaguchi, *J. Japan Electrochem. Soc*. **11**, 260 (1943).

5. N. Weber and A. Venero, 72nd Annual meeting of Am. Ceramic Soc., May 1970, Philadelphia, unpublished work.

6. G. E. Youngblood, A. V. Virkar, W. R. Cannon and R. S. Gordon, *Bull. Amer. Ceram. Soc.*, **56**, 206 (1977).

7. A. V. Virkar, J-F. Jue, And K-Z. Fung, U. S. Patent No. 6,117,807, (2000).

8. A.V. Virkar, T.J. Armstrong, N. Weber, K-Z. Fung and J-F. Jue, *Electrochem. Sco. Proc*., PV 2002-5, 200 (2002)

9. C. K. Kuo, P.S. Nicholson, *Solid State Ionics*, **67**, 157 (1993)

10. C. K. Kuo, P.S. Nicholson, *Solid State Ionics*, **82**, 173 (1995).

11. S. A. Saltykov, in *Proceedings of the Second International Congress for Stereology,* p.163, H. Elias, Editor, National Science Foundation, New York (1967).

12. T. Van Dijk, A. J. Burggraaf, *Phys. Stat. Sol. A*, **63**, 229 (1981).

CHAPTER 4

ELECTROCHEMICAL COARSENING OF COPPER POWDER IN AQUEOUS MEDIA

4.1 Introduction

A process in which larger particles grow at the expense of smaller particles is known as Ostwald ripening or coarsening. Numerous theoretical and experimental studies on Ostwald ripening have been conducted over the past several decades [1-3]. The first systematic study of coarsening was by Ostwald in 1900. Lifshitz and Slyozov [2], and Wagner [3] developed the basic theory of particle coarsening sixty years later. The theory states that coarsening follows a temporal power law $\bar{d}_t^n \propto t$ with exponent $n = 3$ for a diffusion-controlled process and $n = 2$ for an interface-controlled process, where $\bar{d}_t^n$ is the expectation value of the nth moment of the particle size. Following the work of Lifshitz and Slyozov [2], many theoretical studies on the Ostwald ripening process have been reported [4-8]. Recently, Voorhees et al. have conducted an extensive study on the simulations of classical Ostwald ripening in elastically stressed solids [9].

A few reports on electrochemical Ostwald ripening are also available in the literature: Mulder et al. conducted a coarsening study on two mercury drops placed on a Pt – plate in an aqueous Hg^{2+} electrolyte [10]. Even though the droplets were apart (not in physical contact), the larger droplet grew at the expense of the smaller one as ion transport occurred through the bulk electrolyte and electron transport occurred via the

platinum metal support [10]. Redmond et al. observed that Ag films reformed electrochemically when exposed to water containing Ag^+ ions [11]. This was attributed to a negative shift in standard electrode potential of silver which causes differences in the equilibrium silver ion concentration around each particle [12]. Schroeder et al. have done an extensive study on electrochemical Ostwald ripening using a solid electrolyte cell [13-15]. They observed that the open circuit voltage of the electrochemical cell Ag (nano)| solid silver electrolyte| Ag (bulk) was unstable due to the coarsening of nano crystalline silver. The coarsening was attributed to the migration of Ag^+ via the electrolyte and e^- through the metal [13-15].

In conventional solid state Ostwald ripening, metal particles grow by bulk or grain boundary diffusion. In electrochemical Ostwald ripening, growth occurs by a coupled transport of electrically charged species, for example, metal ions and electrons via parallel paths: metal ions through the liquid/ionomer and electrons through the metal or supporting carbon in PEMFC. Coarsening of ionic compounds dissolved in a solvent also occurs by electrochemical Ostwald ripening. An example is a super-saturated solution of NaCl in water; coarsening of particles occurs by a coupled transport of Na^+ and Cl^- through the solution.

Figure 4.1 shows a schematic of the particle coarsening process of metal particles by electrochemical Ostwald ripening [16]. If the two metal particles are isolated in an ion conducting medium, initially, the smaller particles will tend to dissolve and precipitate on larger particles as the chemical potential of smaller particles is higher than that of the larger particles. Thus, for isolated metal particles in an ion conducting medium (no or negligible electron concentration), particle growth is not expected. However, this process will occur if the particles are soluble as neutral species in the conducting medium.

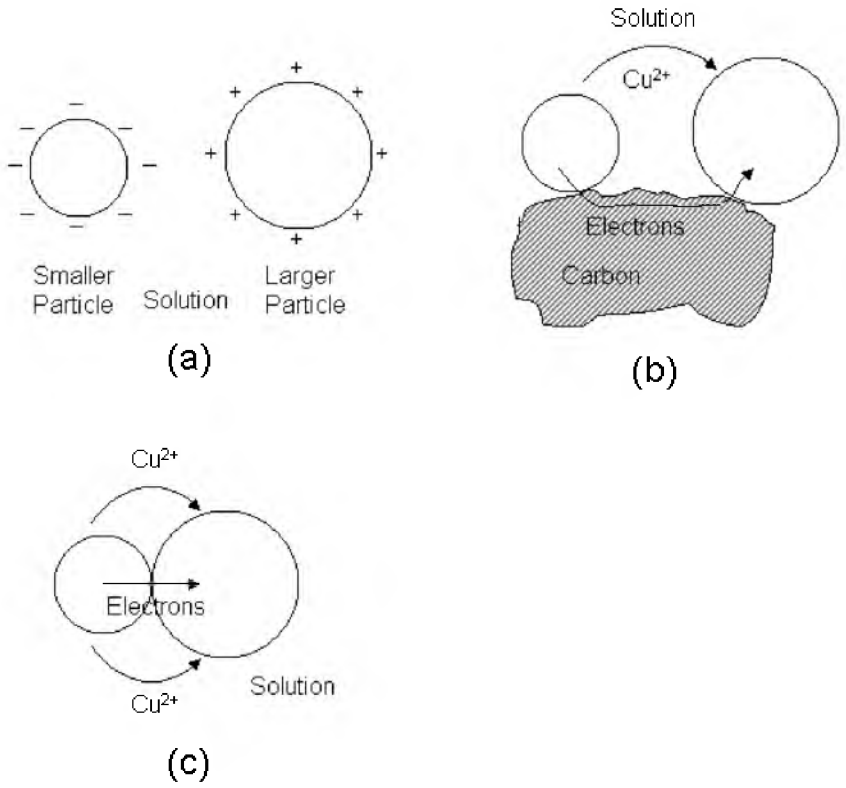

Figure 4.1 Mechanism of coarsening in copper particles. (a) A schematic of two isolated copper particles in an aqueous solution containing copper ions. Transport of copper ions occurs from the smaller particle to the larger particle. Once the electrochemical potential of copper ions is the same in both particles, further transport shuts down. The smaller particle is then negatively charged and the larger one is positively charged. (b) If the particles are sitting on an electronically conducting support, a path for transport of electrons exists, thus causing coarsening (Ostwald ripening). (c) If the particles are in contact with each other, electron transport occurs directly with copper ions transporting through the liquid (agglomeration).

Assuming the presence of only ions in the ion conducting medium (negligible electronic conduction), ions will be transported through the conducting medium from smaller to larger particles, leaving behind electrons. Thus, the smaller particles will become negatively charged and the larger particles become positively charged. Once the electrochemical potential of ions in the particles is equilibrated, further ion transport will be shut down (Figure 4.1(a)). However, the coarsening will occur if there is an alternate path for electrons, as shown in Figure 4.1(b). Coarsening thus will occur by a coupled

transport of ions and electrons.

Coalescence/agglomeration as a mechanism of growth has also been widely discussed in the literature [17, 18]. The driving force is the same as for Ostwald ripening, and bulk diffusion and/or grain boundary diffusion determines the kinetics of growth in the solid state. Figure 4.1(c) shows two metal particles in contact with each other in an ion conducting medium. Here, the ions are transported through the ion conducting medium and electrons through the metal particles in contact. The kinetics of this process is expected to be much faster compared to the typical solid state diffusion when the ion conducting medium is a liquid (such as an aqueous solution). This paper investigates the mechanism of electrochemical Ostwald ripening/agglomeration in copper particles treated under various test conditions. Copper powder was placed in DI water and in different solutions containing various concentrations of $Cu(NO_3)_2$. Copper particles in contact with each other are expected to grow at the expense of smaller particles while isolated copper particles should not grow. Analysis of the results obtained from these experiments should give insight into the mechanisms of particle coarsening by electrochemical Ostwald ripening/agglomeration.

4.2 Experimental Procedure

Commercial copper powder from MCB reagents was used. Copper powder was ultrasonically treated in ethanol for 30 minutes. The sample was filtered and dried. Four different solutions of copper nitrate were prepared in test tubes: 0.001M, 0.01M, 0.1M, and 1M. Five grams of copper powder was added to each of the copper nitrate solutions. Additionally, 5 g of powder each was added to two test tubes containing DI water. Hydrogen gas was bubbled through one of the test tubes with DI water. Figure 4.2 shows

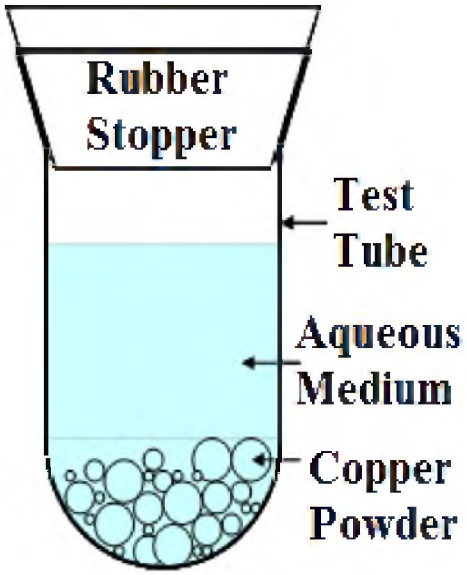

Figure 4.2: A schematic showing the experimental arrangement.

a schematic of the experimental setup. After 48 h at room temperature, the copper powder was filtered, washed in DI water to remove the salt, and dried. The dried samples were analyzed using X-ray diffraction (XRD) and scanning electron microscopy (SEM).

Four different filtrates – DI water sample, DI water sample bubbled with hydrogen, 0.001M copper nitrate solution, and 0.01M copper nitrate solution – were saved from the experiments for further analysis. These filtrate samples were analyzed for the presence of trace elements using Particle Induced X-ray Emission (PIXE). In order to determine the effect of temperature, similar experiments were also conducted at 80^{o}C in DI water, DI water with H_2 bubbling, 0.001M, and 1M $Cu(NO_3)_2$ solutions.

In order to determine the kinetics of coarsening of copper powder, experiments were also conducted in DI water and 0.01M $Cu(NO_3)_2$ solutions for various time periods: 12h, 24h, 48h, 72h, 96h, and 144h. One sample was treated in DI water for 144 h with hydrogen bubbling. The samples were washed in DI water, filtered, and dried. These samples were analyzed using scanning electron microscopy.

The as-received copper powder was also washed in DI water, filtered, and dried and analyzed using SEM. Powders were filtered using a Grade 1 Whatman filter paper. The filtered and dried copper powder samples were analyzed by XRD and SEM. The filtrates of the samples treated 144 h were analyzed for the presence of trace elements using PIXE.

The average particle size distributions of the samples were estimated using the Schwartz-Saltykov diameter analysis [19]. Assuming particles to be spherical, particle volume density is calculated for a particular volume. The different particle sizes were broken down into a number of groups up to 15, depending upon the desired accuracy. With the help of the table of coefficients for the Schwartz-Saltykov method, the particle size distributions were calculated [19]. The coefficients were used in such a way that the volume density of the particles in each size range was obtained by multiplying the number fraction with the given multiplying factor according to the respective contributions to the distribution.

4.3 Results and Discussion

4.3.1 Experiments Conducted at 25°C for 48 h

Figures 4.3(a) through 4.3(d) show scanning electron micrographs (SEM) of copper powder treated at different conditions. Figure 4.3(a) is an SEM of the as-received copper powder. Figures 4.3(b) and Figure 4.3(c) are SEM micrographs of copper powder treated for 48 h in DI water and DI water bubbled with hydrogen, respectively. Figure 4.3(d) shows an SEM image of copper powder treated for 48 h in 1M $Cu(NO_3)_2$ solution.

Table 4.1 lists the average particle sizes measured after various tests conducted for 48 h. The particle size of the copper powder generally increases with increasing

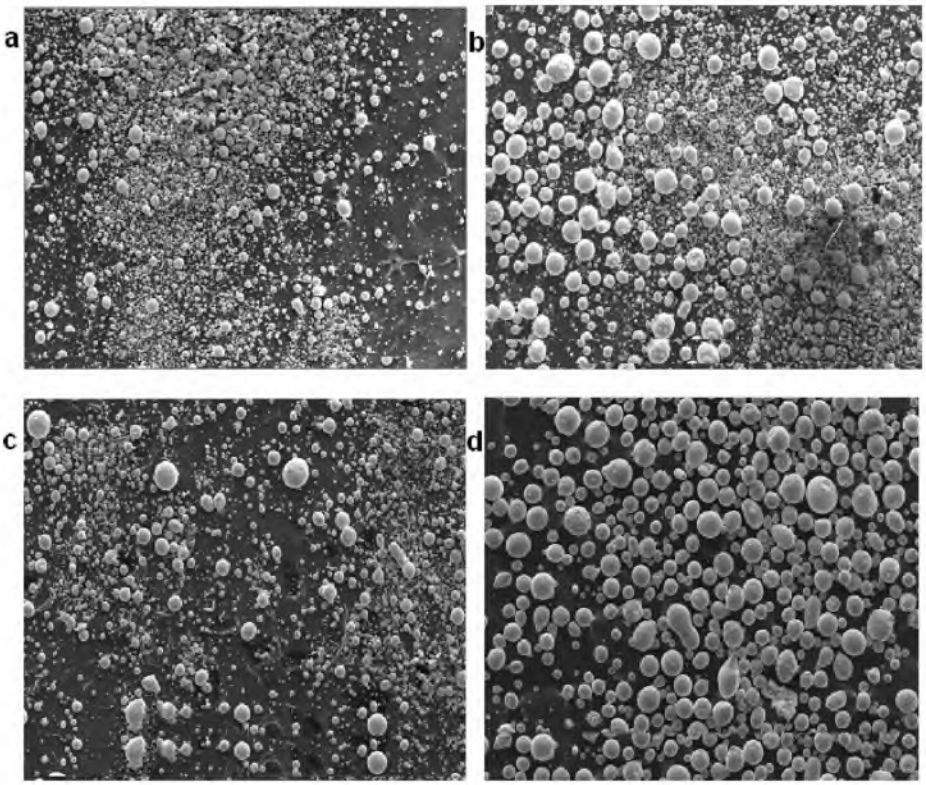

Figure 4.3: SEM micrographs of copper powder subjected to various treatments at room temperature: (a) As-received, (b) DI water for 48 h, (c) DI water with hydrogen bubbling for 48 h, and (d) 1 M $Cu(NO_3)_2$ solution for 48 h. Significant growth occurred in DI water and even greater growth occurred in 1 M solution.

Table 4.1: Comparison of average particle sizes after various treatments and the corresponding copper ion concentration in the filtrates after the tests in selected cases.

Test Condition (Duration - 48 hrs)	Average Particle Size at 25°C (48 h)	Average Particle Size at 80°C (48 h)	Concentration of copper ions present in the filtrate in ppm (25°C)
As-received copper	22 μm ± 10	-	-
DI water treated	33 μm ± 21	41 μm ± 31	6.8 ± 0.6
DI water + H_2	22 μm ± 11	28 μm ± 16	0.0
0.001M $Cu(NO_3)_2$	29 μm ± 17	38 μm ± 26	46.1 ± 1.4
0.01M $Cu(NO_3)_2$	33 μm ± 14	-	530.9 ± 5.3
0.1M $Cu(NO_3)_2$	48 μm ± 28	-	-
1M $Cu(NO_3)_2$	67 μm ± 30	71 μm ± 35	-

copper nitrate concentration. Considerable particle growth occurred in the copper powder treated with 1M copper nitrate solution with an average particle size of 67 μm as compared to the particle size of the as-received copper powder (22 μm). As the copper ion concentration is much higher in 1 M $Cu(NO_3)_2$ solution than in 0.001 M $Cu(NO_3)_2$ solution, the kinetics of coarsening is expected to be more rapid in the solution with higher copper nitrate concentration, as observed. Significant particle growth also occurred in copper powder treated in DI water. The average particle size of the copper powder treated in DI water with hydrogen bubbling is essentially the same as that of the as-received copper powder. Thus, it can be concluded that significant particle coarsening did not occur when hydrogen was bubbled in the DI water. The expectation is that copper ion concentration will be suppressed when hydrogen is bubbled through the liquid. The observed minimal growth is thus consistent with expectations.

In order to determine concentrations of copper ions in the filtrates, samples were analyzed using the Particle Induced X-ray Emission (PIXE) technique. Table 4.1 shows the measured concentration of copper in each of the filtrate samples. The energy of the major X-ray line used for the quantification of copper is 8.048 keV and the standard detection limit is 0.533 ppm. The concentration of copper in the filtrate of copper powder treated with DI water for 48 h was 6.8 ppm. No copper, however, was detected in the filtrate sample with hydrogen bubbling. The measured concentrations of copper ions in 0.001M, and 0.01M copper nitrate solutions were, respectively, 46.1 ppm and 530.9 ppm. However, the average particle size did not seem to vary in proportion to the concentration of copper ions. Also, the coarsening rate was almost the same for copper particles treated in DI water and those treated in 0.01M copper nitrate solution. This may be explained assuming that the local concentration of copper ions near the metal particles probably

was about the same in de-ionized water, 0.001M, and 0.01M copper nitrate solutions since the samples were stagnant during the experiments. Typical diffusion coefficients in liquids are on the order of $10^{-6}cm^2s^{-1}$. Thus, any concentration nonuniformities established near the particles will not be easily dissipated during the course of a typical experiment. For example, the typical diffusion distance in 144 h, the maximum duration of experiments in the present work, will be ~0.5 cm. The water (solution) column height over the powder was ~3 cm. When the filtrate was analyzed, it was not possible to measure the local copper ion concentration as the whole liquid had to be analyzed.

From the literature [20], it is known that pH of the solution plays an important role in the solubility of metals. The solubility of copper in neutral water (pH ~7) is negligible [20]. The pH of the DI water used in the experiment, however, was measured to be ~5.5. This may be due to the CO_2 present in the atmosphere. As soon as the DI water is exposed to atmospheric air, carbon dioxide present in the atmosphere may dissolve in DI water, forming carbonic acid. The solubility of carbon dioxide in water is 1.8g/l. In order to account for the change in pH from 7 to 5.5, the required hydrogen ion concentration is only 3.2×10^{-6}M. As the DI water used was acidic, the copper ion concentration is expected to be higher than at pH 7, which may explain the higher rate of coarsening in DI water than initially anticipated. Furthermore, the measured pH of 0.01M copper nitrate solution was also ~5.5, which is almost the same as that of DI water. Even though the experimentally detected copper concentration present in the filtrate of copper powder treated with DI water for 48 hours was only 6.8 ppm, as stated earlier, the local copper ion concentration close to the particles may be high and comparable to that of 0.01M copper nitrate solution. The measured pH of 0.001M copper nitrate solution was ~6, which is slightly less acidic compared to 0.01M copper nitrate solution, resulting in a

slightly slower rate of coarsening. Copper nitrate tends to act as a buffer in a solution as it is formed by a strong acid and its conjugate base. Because of the presence of copper nitrate in the solution, addition of any reagent which tends to change the pH of the original solution may not be as effective and the pH changes by less than it would do if the solution were not buffered.

The pH of the DI water filtrate after treating copper particles for 48 hours at room temperature was measured to be ~6.5. This indicates that after the test, the filtrate has turned slightly basic compared to the initial DI water. The pH of a saturated solution of copper hydroxide was also measured to be ~6.5. Thus, one of the possible chemical reactions that may occur when copper powder is placed in water is

$$Cu + 2H_2O \rightarrow Cu(OH)_2 + H_2$$

The equilibrium concentration of hydrogen for the above reaction is $\sim 10^{-20}$ bar, while the actual concentration of hydrogen in air is 5×10^{-7} bar [21]. If copper corrosion is presumed to involve the formation of copper oxide, the corresponding equilibrium pH_2 is $\sim 10^{-16}$ bar at $20^{o}C$ [22]. If sufficient hydrogen concentration exists, copper particles will not coarsen when treated in DI water, as the above reaction will shift to the left. Comparison of the micrographs given in Figures 4.3(a) and 4.3(c) shows that only very few copper particles coarsened with hydrogen bubbling. The observation that a few particles coarsened even with hydrogen bubbling suggests that the hydrogen concentration might have been insufficient near the particles. This is attributed to slow bubbling of hydrogen on purpose to ensure particles were not stirred during the experiments. If the particles are stirred, the coarsening phenomenon will be entirely different from what is studied in this research.

4.3.2 Experiments Conducted at 80°C

Figures 4.4(a), 4.4(b), 4.4(c), and 4.4(d) show SEM micrographs of the as-received powder, treated in DI water, in DI water with H_2 bubbling, and in 0.001M $Cu(NO_3)_2$ solution, respectively, for 48 hours at 80°C. The particle sizes of the three treated samples are given in Table 4.1. A comparison shows an average growth of around 35 – 40% with respect to the particle size of copper powder treated in DI water and 0.001M $Cu(NO_3)_2$ solution at room temperature. Copper powder treated in DI water with hydrogen bubbling exhibited significant growth as compared to that at room temperature. The concentration of copper ions in the liquid in close proximity to the particles must be higher due to higher temperature, stagnant medium, and partial pressure/concentration of

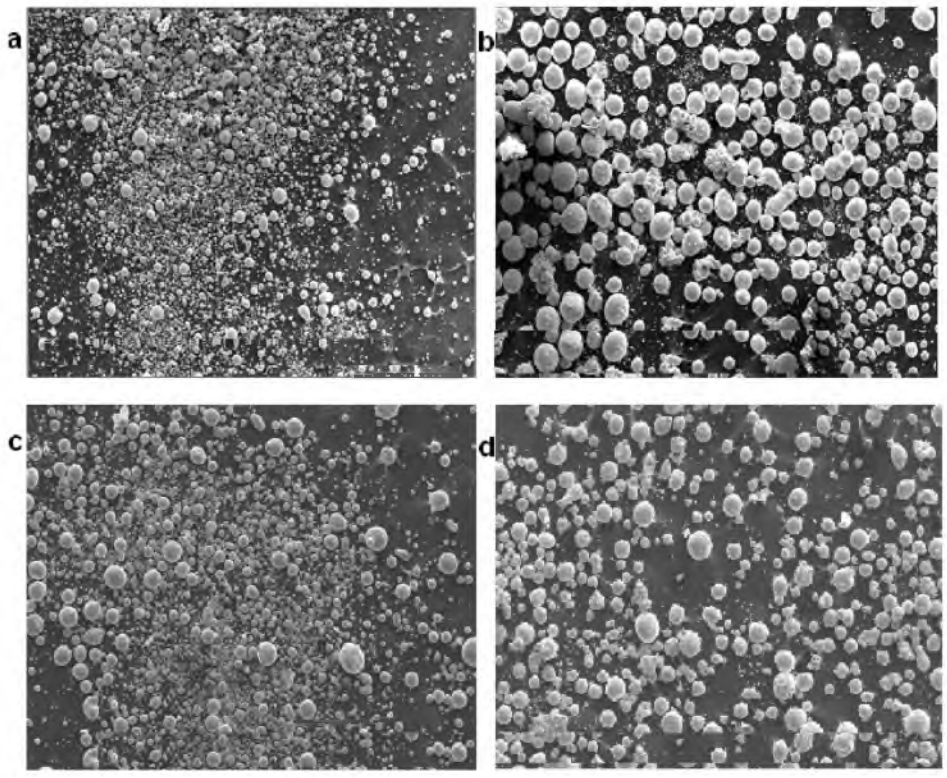

Figure 4.4: SEM micrographs of copper powder subjected to various treatments at 80°C: (a) As-received, (b) DI water for 48 h, (c) DI water with hydrogen bubbling for 48 h, and (d) 1 M $Cu(NO_3)_2$ solution for 48 h. Detectable growth occurred in DI water with hydrogen bubbling. Growth occurred to a greater extent in DI water. Surface of copper powder treated in 1 M solution appears rough due to the formation of copper oxide

the bubbling hydrogen close to the particles being lower than a similar experiment conducted at room temperature. The solubility of H_2 in DI water at 25°C is 156μg/100g of water, whereas the solubility at 80°C is 0.000079g/100g of water [24]. Thus, the solubility at 80°C is lower by a factor of about 2. Significant growth of particle size at 80°C even with hydrogen bubbling thus can in part be attributed to the lower solubility of hydrogen.

In order to determine the possible formation of an oxide layer on copper powders, the samples were analyzed by XRD. Figure 4.5 shows XRD patterns of copper samples treated in different solutions for 48 h: (a) at room temperature, and (b) at 80°C. Peaks corresponding to copper are identified in all samples. The sample treated in 1 M solution at 80°C contained additional peaks. These extraneous peaks were identified as belonging to copper oxide. The powder also exhibited dull dark red color as opposed to bright metallic luster, consistent with surface oxide formation. Miller and Lawless [23] observed that the formation of oxide on copper crystals when immersed in a copper salt solution is dependent on the pH of the solution. They conducted experiments with copper sulfate solution and determined that oxide formation occurred in solutions with pH below 3.8. The pH of copper nitrate solutions of various concentrations used in this study was measured. The pH of DI water and 0.01M copper nitrate solutions were about the same (~5.5). The pH of 0.1M copper nitrate solution was ~4.5 and that of 1M copper nitrate solution was ~3.6, which explains the formation of copper oxide when treated with 1M copper nitrate solution. Thus, for the current study, copper samples treated with 1M copper nitrate solution at 80°C are not considered in further analysis. Figures 4.6 and 4.7 show the particle size distributions of copper particles subjected to various test conditions for 48 h.

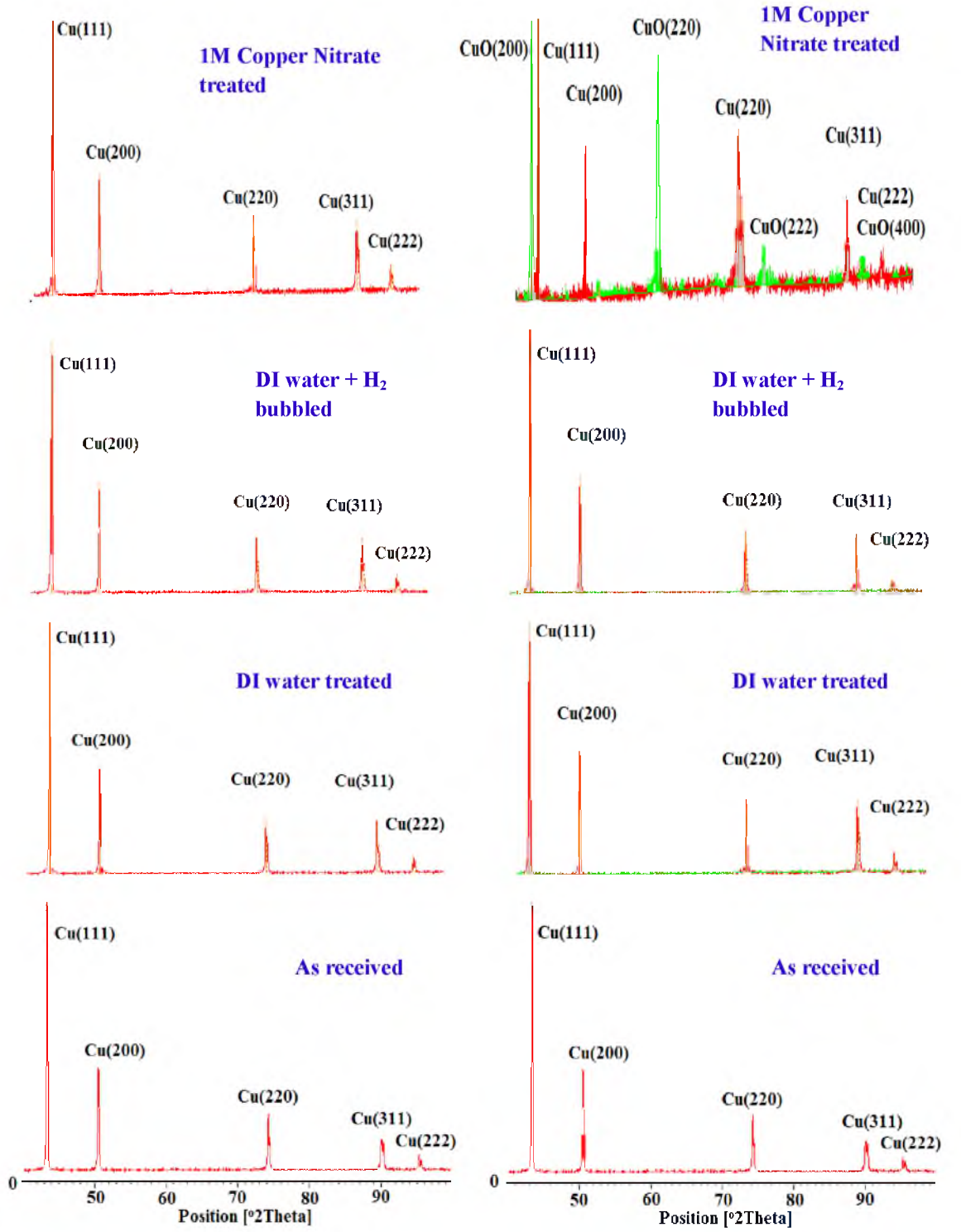

(a) Room temperature (b) 80°C

Figure 4.5: X-ray diffraction patterns of copper powder after various tests and comparison with the as-received powder. (a) Experiments at room temperature. All XRD patterns show only the metallic copper peaks. (b) Experiments at 80°C. All XRD patterns show only metallic copper peaks, except the sample treated in 1 M $Cu(NO_3)_2$ solution which also shows peaks corresponding to copper oxide (CuO).

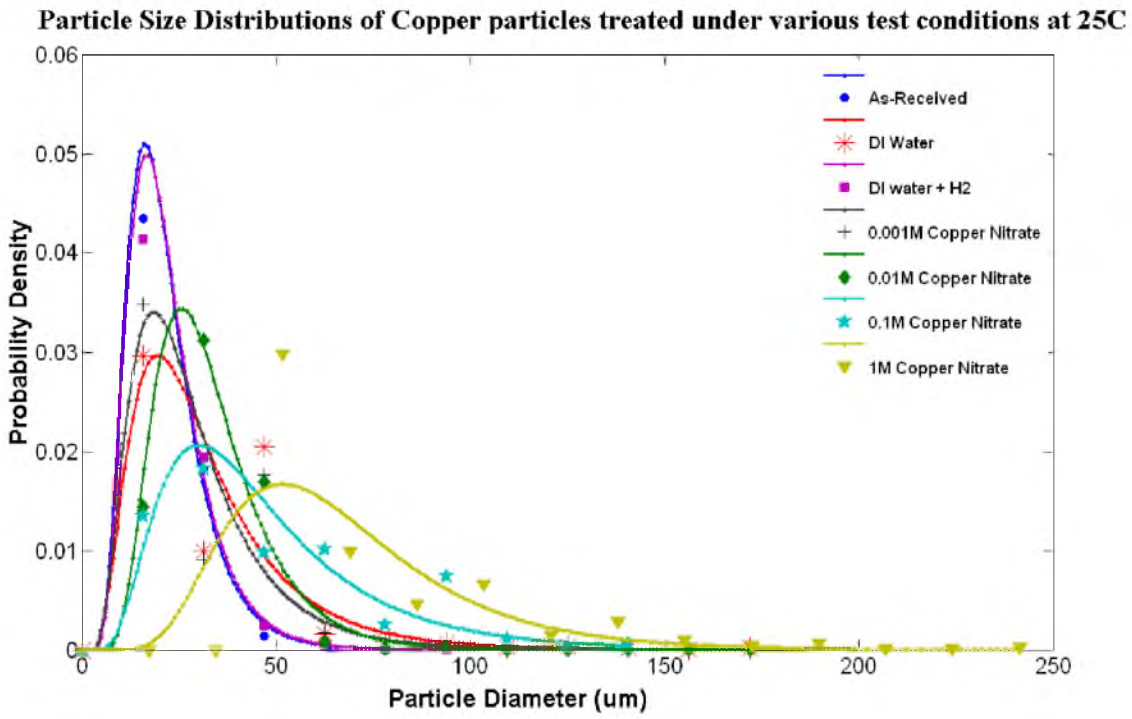

Figure 4.6: Particle size distributions of samples subjected to various treatments at room temperature for 48 h.

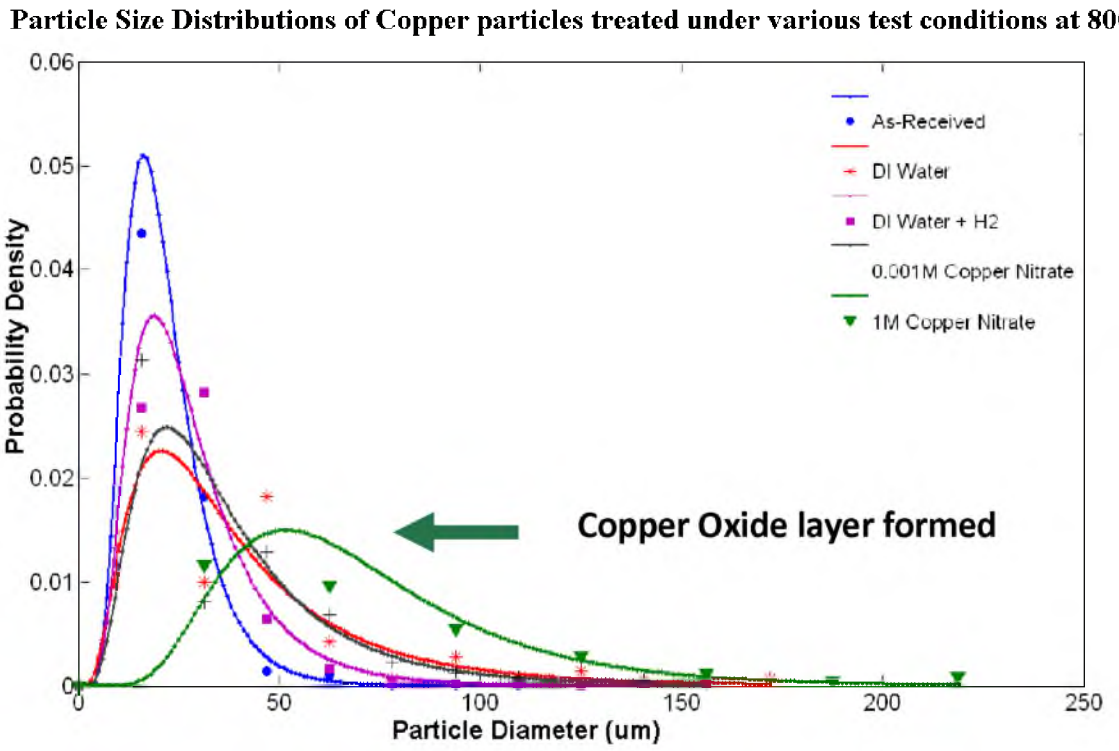

Figure 4.7: Particle size distributions of samples subjected to various treatments at 80°C for 48 h.

Schwartz-Saltykov diameter analysis was used to determine the distribution and was fitted log normally with the help of MATLAB software. Figure 4.6 shows the particle size distributions of copper particles treated in different solutions at room temperature as compared to the as-received copper powder sample. From the distribution, it is clear that the particle size distribution of copper particles treated in DI water bubbled with hydrogen is essentially the same as the as-received sample. Growth of particles and broadening of the distribution is seen in the samples treated in DI water, 0.001 M solution, and 0.01 M solution. These three distributions appear to be about the same within the experimental scatter. As stated earlier, this may well be related to possibly having about the same concentration of copper ions in close proximity to particles due to the stagnant medium. Distributions for the samples treated in 0.1 M and 1 M solutions are broader and have shifted to the right, as expected.

Figure 4.7 compares the particle size distributions of copper particles treated in various solutions at 80^{o}C with the as-received sample. At 80^{o}C, even with hydrogen bubbling, there is significant growth of particle size and broadening of the distribution. As mentioned earlier, the lower solubility of hydrogen in water can be the reason for the increased growth of copper particles at the higher temperature. At other concentrations also, the effect of temperature is to broaden the distribution in relation to the corresponding experiments at room temperature. Also shown in the figure is the distribution for treatment in 1 M solution.

4.3.3. Experiments Conducted at 25^{o}C for up to 144 h

Figures 4.8(a), 4.8(b), 4.8(c), and 4.8(d) show SEM micrographs of the as-received and washed powder, treated in DI water at room temperature for 12 h, 72 h, and

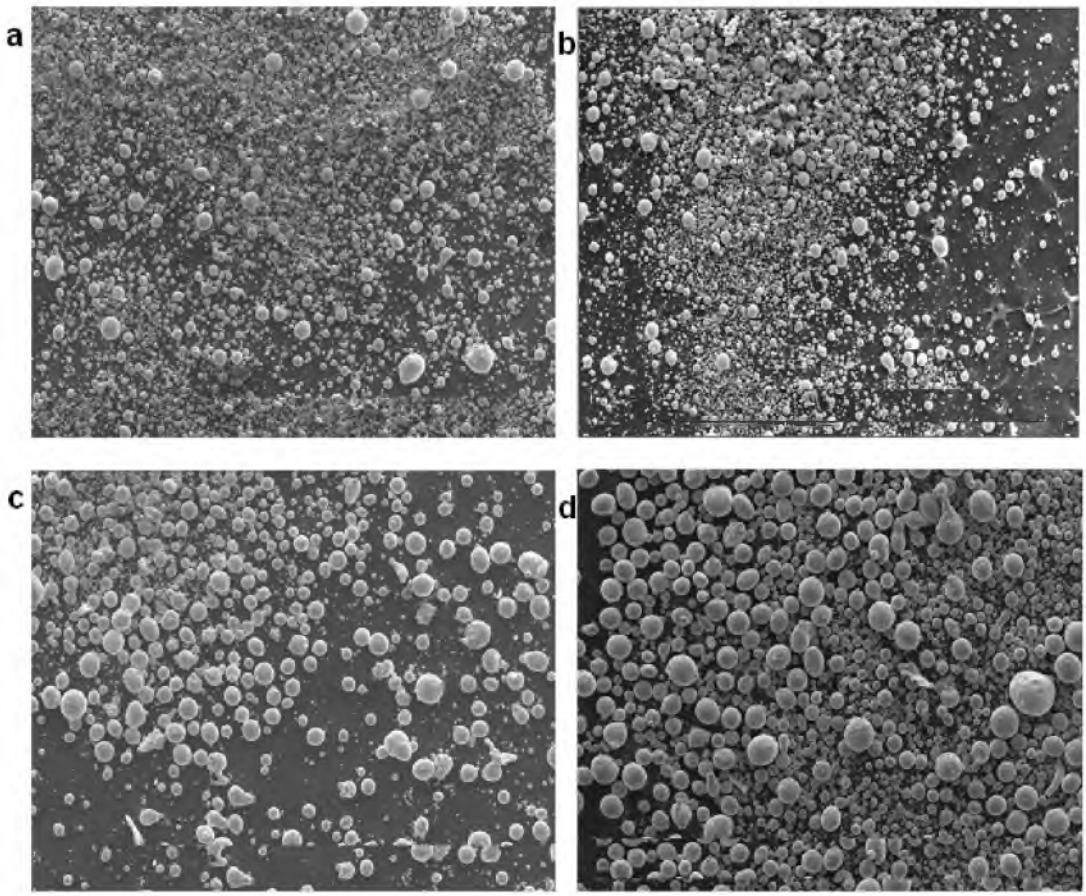

Figure 4.8: SEM micrographs of copper powder treated in DI water at room temperature for various periods of time: (a) As-received and washed, (b) 12 h, (c) 72 h, and (d) 144 h.

144 h, respectively.

Figures 4.9(a), 4.9(b), 4.9(c), and 4.9(d) show SEM micrographs of the as-received and washed powder, and treated in 0.01M $Cu(NO_3)_2$ solution at room temperature for 12 h, 72 h, and 144 h, respectively. The average particle size of the samples measured is given in Table 4.2. Coarsening occurred in both sets of samples. The average particle size of copper powder treated in 0.01M copper nitrate solution for 144 h is larger than the as-received copper by a factor of ~3. This shows that considerable growth occurred. The average particle sizes of copper powder treated in DI water and 0.01 M copper nitrate solutions for 144 h appear to be almost the same. As stated earlier,

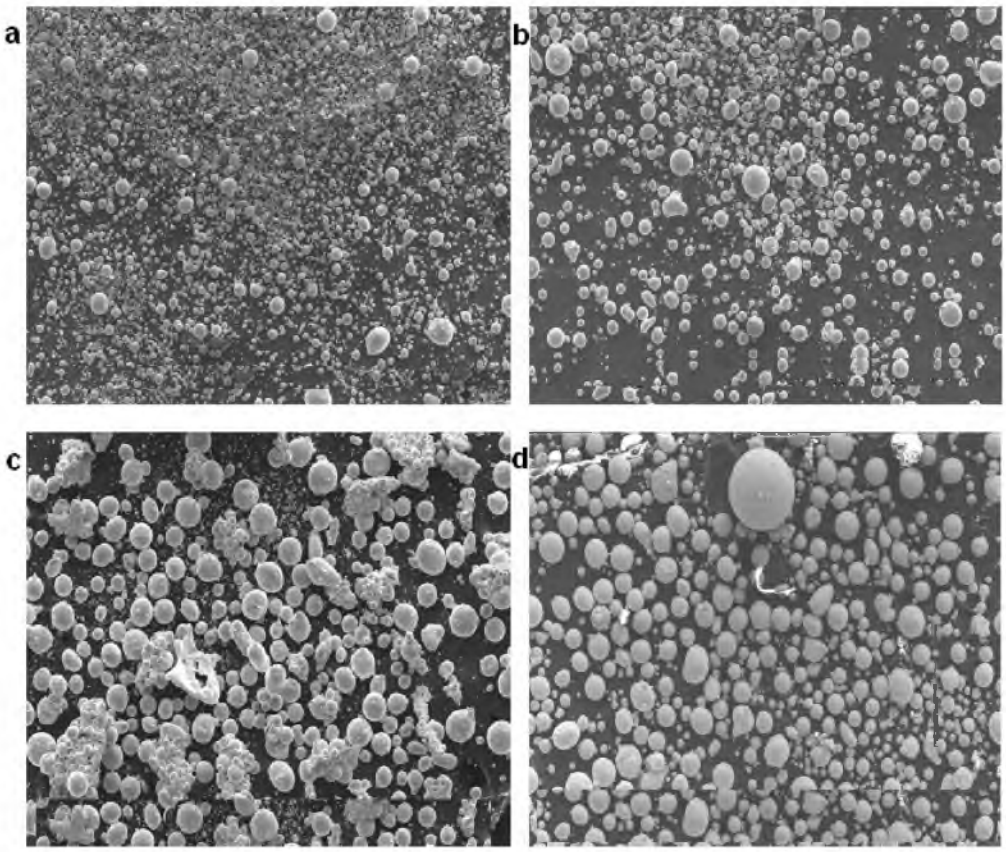

Figure 4.9: SEM micrographs of copper powder treated in 0.01M copper nitrate solution at room temperature for various periods of time: (a) As-received and washed, (b) 12 h, (c) 72 h, (d) 144 h.

Table 4.2: Comparison of average particle sizes after conducting the experiments for various durations at room temperature

Duration (hr)	As-received and washed - Average Particle Size	DI water treated - Average Particle Size	0.01 M $Cu(NO_3)_2$ - Average Particle Size
-	22.4 μm ± 11	-	-
12	-	25 μm ± 14	27 μm ± 19
24	-	30 μm ± 21	31 μm ± 21
48	-	33 μm ± 23	36 μm ± 20
72	-	39 μm ± 21	42 μm ± 24
96	-	48 μm ± 18	49 μm ± 25
144	-	59 μm ± 23	64 μm ± 30

the pH of both DI water and 0.01M copper nitrate solutions were about the same (~5.5) before conducting the experiment. The concentration of copper ions in the samples treated for 144 h were determined by PIXE analysis. The concentration of copper in the filtrate of copper powder treated with DI water for 144 h was 2.9 ppm as compared to 6.8 ppm for 48 h. This difference in the measured concentrations may be due to the dilution of the local concentration of copper ions when the whole liquid was analyzed. The measured concentration of copper ions in 0.01M copper nitrate solution for 144 h was 567 ppm as compared to 530 ppm for 48 h. Even though the copper ion concentration of 0.01M $Cu(NO_3)_2$ is vastly different from that of the DI water, the average particle size was comparable. This suggests that the local concentration of copper ions near the metal particles may be similar to that in de-ionized water and 0.01M copper nitrate solutions since the samples were stagnant during the experiments. Since the whole liquid was analyzed, determining the local concentration where the growth occurred was not possible. Figures 4.10 and 4.11 show the particle size distributions of the copper particles treated at room temperature in DI water and in 0.01M copper nitrate solution, respectively, for various times ranging between 12 h and 144 h. With increase in the time of treatment, the distributions for the samples treated in both DI water and in 0.01M copper nitrate solution are broader and have shifted towards the right, as expected.

Copper powder was also treated in DI water with hydrogen bubbling for 144 h. It was observed that the average particle was virtually unchanged (~23 microns) when compared to the starting powder size (~22 micron). This observation is again in accord with expectations – negligible copper ion concentration with hydrogen bubbling leading to negligible transport and negligible particle growth. This is due to the reducing nature of hydrogen.

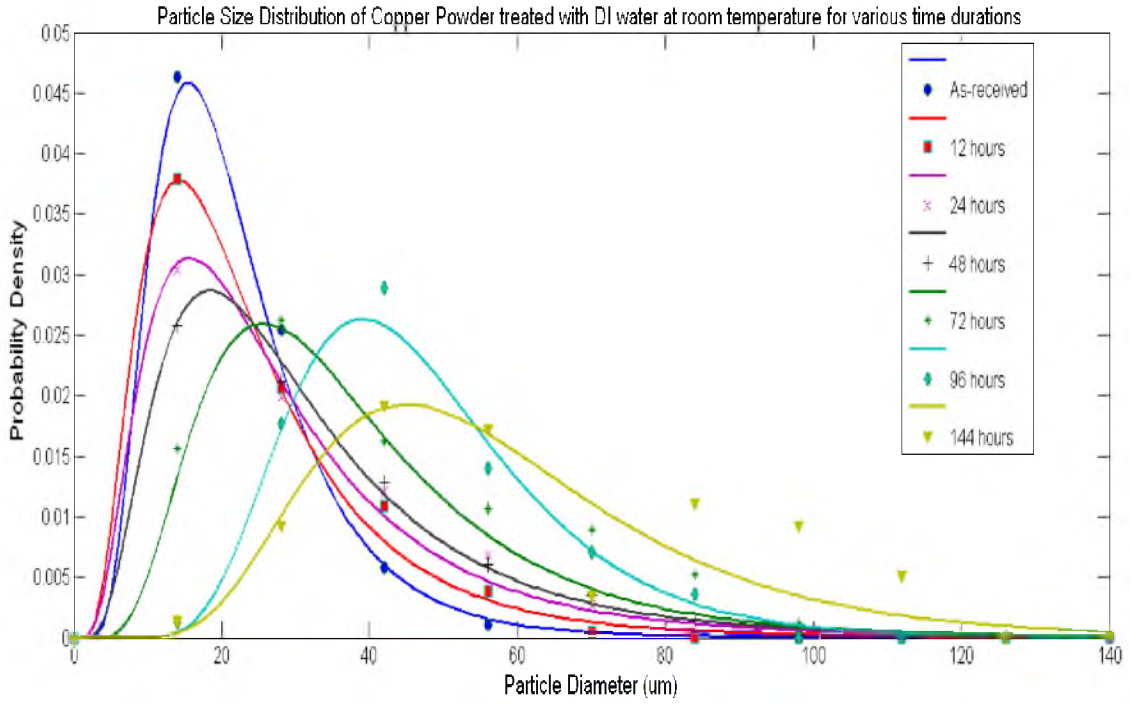

Figure 4.10: Particle size distributions of samples treated in DI water at room temperature for various periods of time.

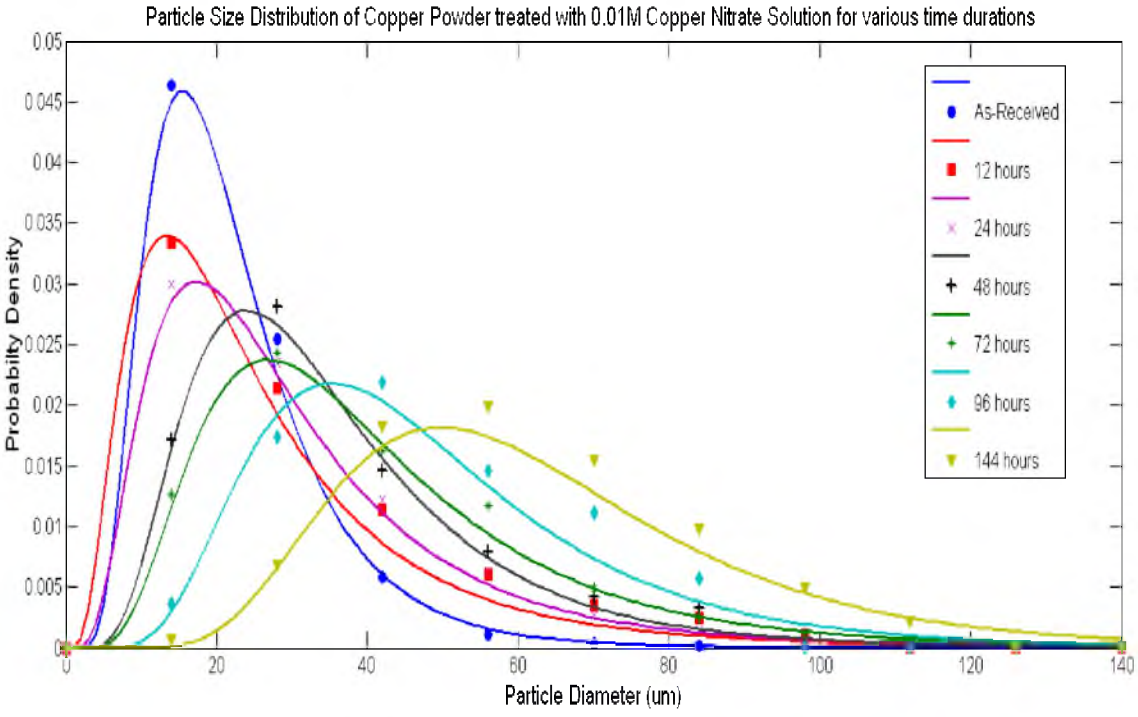

Figure 4.11: Particle size distributions of samples treated in 0.01M copper nitrate solution at room temperature for various periods of time.

4.3.4 Kinetics of Coarsening

The kinetics of particle coarsening or Ostwald ripening can be typically described by relations of the following type, depending upon whether the process is diffusion-controlled or interface-controlled. For diffusion-controlled coarsening,

$$\bar{d}_t^3 - \bar{d}_o^3 = k_D t \tag{4.1}$$

where $\bar{d}_o^3$ is the average of the third moment of the initial particle size, $\bar{d}_t^3$ is the average of the third moment of the particle size after time t, and k_D is the rate constant for diffusion-controlled growth (cm^3/s). If the kinetics is interface-controlled,

$$\bar{d}_t^2 - \bar{d}_o^2 = k_S t \tag{4.2}$$

where k_S is the rate constant for interface-controlled growth (cm^2s^{-1}). The above equations describe growth kinetics of isolated particles in many metallic and ceramic systems

Figure 4.12 shows plots of the particle size vs. time for copper particles treated with DI water and 0.01M $Cu(NO_3)_2$ solution at room temperature for up to 144 h. Also shown in Figure 4.10 is the data point corresponding to the particle size of the sample treated in DI water for 144 h with hydrogen bubbling. As is evident, negligible growth occurred consistent with negligible concentration of copper ions with hydrogen bubbling. As seen in the figure, the kinetics exhibit linear dependence on time, that is

$$\bar{d}_t - \bar{d}_o = k_L t \tag{4.3}$$

The rate constant, k_L, is 7.07 x 10^{-9} cms^{-1} for powder treated in DI water and

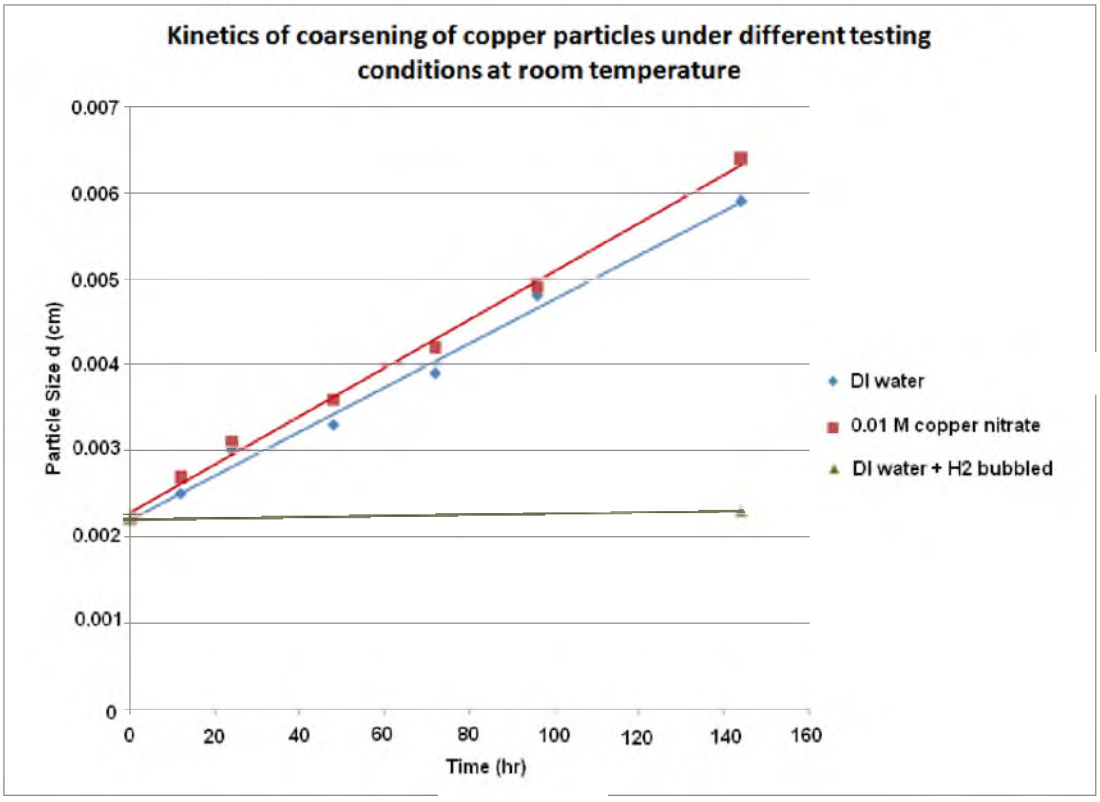

Figure 4.12: Kinetics of coarsening of copper particles under different testing conditions at room temperature.

7.7×10^{-9} cms^{-1} for powder treated in 0.01 M $Cu(NO_3)_2$ solution. The authors are not aware of any systems exhibiting linear dependence of coarsening. In most studies on particle coarsening, such as in many metallic systems, particles are physically separate (isolated). Also, particle growth in PEMFC cathodes involves transport between particles that are mostly physically isolated although in contact with carbon support. In such a case, particle growth occurs by electrochemical Ostwald ripening with ion transport through aqueous medium/Nafion and electron transport occurs through carbon support [16]. In both of these cases, conventional Ostwald ripening of physically separate metallic particles (e.g., in a two-phase alloy) or catalyst degradation in PEMFC, the diffusion distance remains the same.

In the present case, growth of agglomerated particles occurs with ion transport

through the liquid and electron transport through direct particle to particle contact. Thus, as one particle grows at the expense of another in contact, the center-to-center distance decreases. A decrease in center-to-center distance would mean an even greater increase in the driving force – beyond that due to increasing difference in particle sizes of neighboring particles. The observed linear kinetics may be related to this aspect. Thus, the kinetics appears to be interface-controlled with the added feature of decreasing inter-particle distance between contacting particles. With hydrogen bubbling, negligible growth occurred. It is thus the expectation that at very low copper ion concentrations, the kinetics may be diffusion-controlled.

4.4 Summary

Experiments on the growth of copper particles in aqueous media containing various concentrations of copper ions (by dissolving copper nitrate) were conducted. The samples were placed in test tubes in stagnant conditions. Experiments were conducted at room temperature and at 80^{o}C. In order to obtain as low a concentration of copper ions as possible, experiments were also conducted in DI water with hydrogen bubbling. For determining the kinetics of particle growth, experiments were conducted for different time periods varying between 12 h and 144 h at room temperature in DI water, in DI water with hydrogen bubbling, and in 0.01 M $Cu(NO_3)_2$ solution. Negligible growth occurred in samples treated at room temperature with hydrogen bubbling, which was attributed to very low copper ion concentration. It was also observed that the kinetics was faster at higher temperature. Since electron concentration in an aqueous medium is negligible, it is expected that no growth would have occurred in isolated particles. However, as particles were placed in test tubes, the vast majority of particles were not

isolated (were in contact with the neighboring particles). The growth of particles occurred by a coupled transport – that of copper ions through the liquid and that of electrons through direct contact. Solid state transport is all but ruled out given the very low diffusion coefficient of copper in the solid state at such a low temperature. Indeed, a comparison of the present results with Ostwald ripening in metallic alloys shows orders of magnitude difference in kinetics. Since the diffusion coefficient of ions through aqueous media is typically 10^{-6} to 10^{-5} cm^2s^{-1}, which is several orders of magnitude higher than that in the solid-state, the kinetics of electrochemical Ostwald ripening/agglomeration is expected to be much faster compared to solid state Ostwald ripening, as observed in the present work.

The kinetics of particle growth exhibited linear dependence. For physically separated particles in most studies, kinetics of growth is typically cubic (diffusion-controlled – equation (4.1)) or parabolic (interface-controlled – equation (4.2)). The observation that the kinetics is linear (equation (4.3)) is attributed to interface-controlled growth with the additional feature of increased driving force due to decreased transport (diffusion) distance as the center-to-center distance between particles decreases with the occurrence of growth. Since negligible solid state transport is expected, the difference between Ostwald ripening of physically separate particles (yet sitting on an electronically conducting support) and those in direct contact with each other (often referred to as agglomeration) is only the relative difference in diffusion distances. Agglomeration in such a case may be referred to as electrochemical agglomeration. Since the diffusion distance is shorter in electrochemical agglomeration, its kinetics is expected to be much faster than Ostwald ripening of physically separate (yet sitting on an electronically conducting support) particles. This has important implications to catalyst growth in

PEMFC. The present work suggests that catalyst growth of particles in direct physical contact (agglomerated) may be much faster than physically separate (yet sitting on carbon) particles. Thus, special care should be taken to avoid agglomeration in PEMFC electrodes, especially the cathode.

4.5 Acknowledgements

This work was supported by the US Department of Energy under the Grant Number DE-FG02-06ER46086.

4.6 References

1. G. W. Greenwood, *Acta Metallurgica*, **4**, 243 (1956).
2. I. M. Lifshitz, V. V. Slyozov, *Phys. Chem. Solids*, **19**, 35 (1961).
3. C. Wagner, *Z. Elektrochem.*, **65**, 581 (1961).
4. P. W. Voorhees, *J. Stat. Phys.*, **38**, 231 (1985).
5. S. P. Marsh, M. E. Glicksman, *Acta Materialia*, **44**, 3761 (1996).
6. H. Gratz, *J. Mater. Sci. Lett.*, **18**, 1637 (1999).
7. P. Streitenberger, *Scripta Mater.*, **39**, 1719 (1998).
8. G. Madras, B. J. McCoy, *Powder Tech.*, **143**, 297 (2004).
9. K. Thornton, N. Akaiwa, P. W. Voorhees, *Acta Materialia*, **52**, 1353 (2004).
10. W.H. Mulder, J.H. Sluyters, *J. Electroanal. Chem.*, **468**, 127 (1999).
11. P. L. Redmond, A. J. Hallock, L. E. Brus, *Nano Lett.*, **5**, 131 (2005).
12. W. J. Plieth, *J. Phys. Chem.*, **86**, 3166 (1982).
13. A. Schroeder, J. Fleig, D. Gryaznov, J. Maier, W. Sitte, *J. Phys. Chem. B*, **110**, 12274 (2006).
14. A. Schroeder, J. Fleig, H. Drings, R. Wuerschum, J. Maier, W. Sitte, *Solid State Ionics*, **173**, 95 (2004).

15. A. Schroeder, J. Fleig, J. Maier, W. Sitte, *Electrochimica Acta*, **51**, 4176 (2006).

16. A.V. Virkar, Y. Zhou, *J. Electrochem. Soc.*, **154**, B540 (2007).

17. X. Wang, C. Somsen, G. Grundmeier, *Acta Materialia*, **56**, 762 (2008).

18. J. D. Porter, T. O. Robinson, *J. Phys. Chem.*, **97**, 6696 (1993).

19. S. A. Saltykov, *Stereology*, p. 163, H. Elias,Editor, *Proc. Second Int. Cong. For Stereology*, Springer-Verlag, New York (1967).

20. J. A. Dyer, N.C. Scrivner, S.K. Dentel, *Environ. Progress*, **17**, 1 (1998).

21. G. Hultquist and P. Szakalos, *J. Atmos. Chem.*, **55**, 131 (2006).

22. B. Beverskog and I. Puigdomenech, *J. Electrochem. Soc.*, **144**, 3476 (1997).

23. G. T. Miller, Jr., K. R. Lawless, *J. Electrochem. Soc.*, **106**, 854 (1959).

24. A. Seidell, *Solubilities of Inorganic and Metalorganic Compounds, Vol. I.*, Van Nostrand: New Jersey (1958).

CHAPTER 5

EFFECT OF STRESS ON DISSOLUTION/PRECIPITATION OF PLATINUM: IMPLICATIONS CONCERNING CORE-SHELL CATALYSTS AND CATHODE DEGRADATION IN PEM FUEL CELLS

5.1 Introduction

Proton Exchange Membrane Fuel Cells (PEMFCs) have applications in transportation, distributed power, and portable power. Considerable progress has been made over the past two decades in PEMFC. However, it is well known that degradation in performance occurs over time, which in part has limited the commercial exploitation of PEMFC. There are many factors which influence PEMFC degradation. These include the materials used in PEMFC and the operating conditions. Typically, both the cathode and the anode of a PEMFC contain nanosize noble metal (Pt) or noble metal alloy particles supported on high surface area carbon. One of the reasons for alloying Pt with non-noble metals is to reduce the Pt loading and thus lower the cost [1-8]. The lowering of Pt loading can also be achieved by making core-shell catalysts with core made of a non-noble metal or a Pt alloyed with a non-noble metal and shell of Pt. Considerable work has been reported on core-shell catalysts [9-34].

Several mechanisms of cathode degradation have been reported [35-46]. They include: (a) detachment of catalyst particles from carbon support, thus rendering them

electro-catalytically inactive; (b) Ostwald ripening of particles; (c) agglomeration and associated growth (sintering) of particles; (d) dissolution of the catalyst at the cathode, its transport and precipitation into the membrane. All of these phenomena lead to a decrease in the catalyst surface area, decrease in catalytic activity, and thus loss in performance. Insofar as the operating conditions are concerned, studies have shown that greater degradation occurs at open circuit than when the fuel cell is under load. This observation has important implications concerning the idling characteristics of a PEMFC. It is also known that negligible degradation occurs at the anode even when its composition is substantially the same as the cathode.

Figure 5.1 shows schematics of the four aforementioned degradation mechanisms. Ostwald ripening, agglomeration and sintering, and precipitation in the membrane all depend upon some aspects of local dissolution of Pt, its transport, and its precipitation [47].

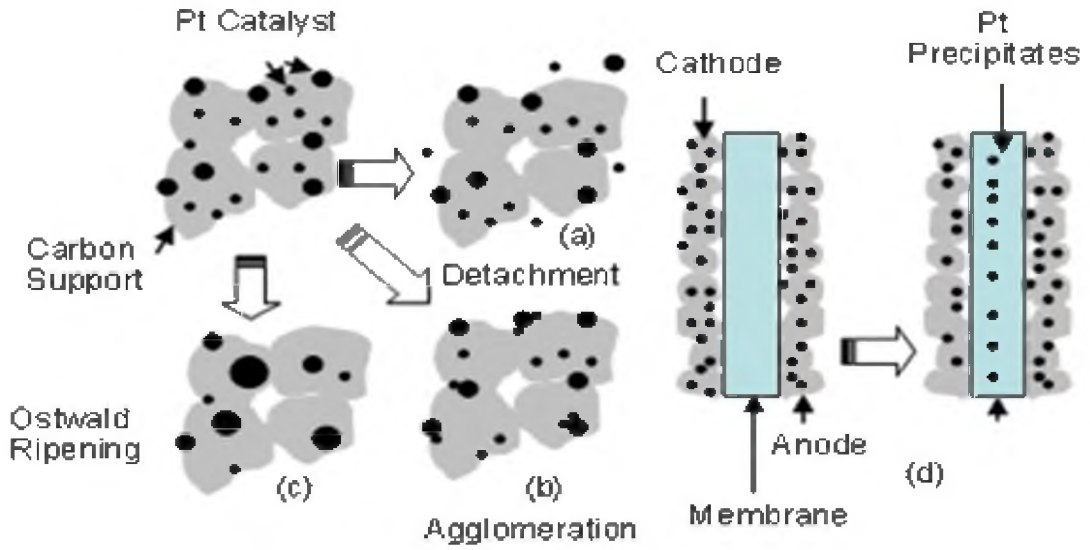

Figure 5.1: Mechanisms of cathode degradation in PEMFC: (a) Detachment from carbon support, (b) Agglomeration and sintering, (c) Ostwald ripening, and (d) Dissolution at the cathode, transport and precipitation into the membrane.

The thermodynamic driving force for agglomeration/sintering and Ostwald ripening is the reduction in surface energy accompanying particle growth. This phenomenon leads to dissolution of smaller particles and growth of larger particles. Ostwald ripening occurs by the dissolution of particles into a medium, transport through the medium, and deposition on larger particles. In PEMFC, transport of electrically neutral Pt occurs via a coupled process involving the transport of ions (Pt^{2+} and/or Pt^{4+}) through an ionomer/aqueous medium and a parallel (coupled) transport of electrons through the carbon support [48]. In agglomeration/sintering, a similar process occurs where ions transport through an ionomer/aqueous medium and electrons transport through a direct particle-to-particle contact. Figure 5.2 shows schematics of the growth of Pt particles by dissolution/precipitation of isolated particles (supported on high surface area carbon) and of particles in direct physical contact with each other (agglomeration/sintering). The fundamental physical parameter which dictates degradation kinetics is the electrochemical potential of Pt ions, which depends upon the chemical potential of Pt. All those factors which lower the chemical potential of Pt should generally decrease the kinetics of degradation, and all those factors which increase the chemical potential of Pt should increase the kinetics of degradation.

The chemical potential of a species depends on composition, temperature, and pressure. Alloying Pt with other metals lowers the chemical potential of Pt. Many alloys of Pt are currently being explored for application as PEMFC catalysts [1-8]. Hydrostatic stress (pressure) also affects the chemical potential. This of course is well known and is the basis of the Gibbs-Kelvin equation and is the reason for the occurrence of Ostwald ripening/agglomeration [49].

The dependence of chemical potential of Pt, μ_{Pt}, on temperature, composition,

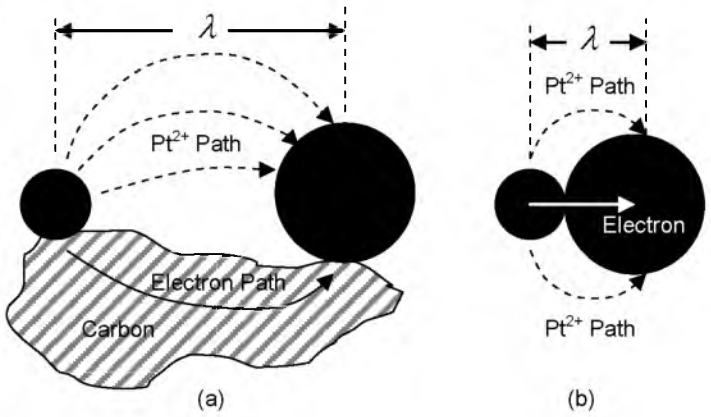

Figure 5.2: Mechanism of particle growth by (a) Ostwald ripening, (b) Agglomeration/ sintering. Both occur by a coupled transport of Pt^{2+} (or Pt^{4+}) ions through ionomer/aqueous media and electron transport through the carbon support (or through direct particle-to-particle contact). Net Pt transport occurs from smaller particles to larger particles.

and on pressure is given by [49]

$$\mu_{Pt} = \mu_{Pt}^{o} + RT \ln a_{Pt} + pV_m \tag{5.1}$$

where μ_{Pt}^{o} is the standard state chemical potential of Pt, a_{Pt} is the activity of Pt, V_m is the partial molar volume of Pt, and p is the pressure. If the material is pure Pt, then a_{Pt} is unity. For spherical particles, the pressure is given by $2\gamma/r$ where r is the particle radius and γ is the surface energy. Thus, the smaller the particle size, the higher is the pressure inside the particle, the higher is the chemical potential, and the greater is the tendency for its dissolution and deposition on larger particles.

Equation (5.1) is very general in that the sign of pressure determines whether it will increase or decrease the chemical potential. On a sample of any general geometric shape, positive or negative pressure can be created by the application of external forces. If the pressure is positive (compressive), the chemical potential will be higher compared

to a stress-free material. If the pressure is negative (tensile), however, the chemical potential should be lower compared to a stress-free material. The effect of stress on electrode potentials of metals was investigated during the 1950s and 1960s, primarily to determine the effect of stress on corrosion. Several authors had assumed that the dominant stress-related term in chemical potential is the strain energy, which is proportional to the square of stress (or the square of pressure). The expectation under this assumption was that the electrode potential should be the same in both tension and compression for a given magnitude of stress. However, many experimental results were found to be inconsistent with this expectation [50,51]. It was in fact observed that the sign of electrode potential depended upon whether the applied load was tensile or compressive [50,51]. Flood [52], in a classic paper, demonstrated that the dominant term in chemical potential is in fact linearly related to pressure (consistent with equation (5.1)), and thus, electrode potential is expected to exhibit a reversal in sign upon a reversal in the sign of stress (tensile or compressive), in accord with the general thermodynamic theory of Gibbs. This result is actually not surprising. Indeed, it is well known in theories of creep that matter movement occurs from regions of compression to regions of tension.

The analysis by Flood [52] has a significant bearing on the role of stress on catalyst stability and specifically on the design of core-shell catalysts. Core-shell catalysts typically consist of a core and a shell of different materials but generally of the same crystal structure, and with an epitaxially matched interface. The lattice parameters of the core and the shell determine the magnitude (and possibly the sign) of the stress in the shell of a core-shell catalyst. If the Pt shell is under greater compression than a pure Pt catalyst particle of the same diameter, the chemical potential of Pt will be higher in the

shell of the core-shell catalyst than the monolithic Pt catalyst. Such a catalyst may exhibit increased tendency for dissolution. If the Pt shell is under reduced compression (or even possibly in tension) than a pure Pt catalyst of the same diameter, the chemical potential of Pt in the shell will be lower in the core-shell catalyst than the monolithic Pt catalyst. Such a catalyst should exhibit decreased tendency for dissolution and thus should exhibit increased stability. An example is a core-shell catalyst with Pt shell and Ag or Au core. Such core-shell catalysts should be inherently more stable compared to pure Pt catalysts of the same outer diameter.

The objective of the present work was to investigate the role of stress on the chemical potential of Pt using an electrochemical technique. This was achieved using Pt wires/foils of macroscopic dimensions as electrodes. Implications of the results for the design of core-shell catalysts for PEMFC are discussed. The implications for core-shell catalysts are further compared with recent literature on atomistic level (DFT) calculations.

5.2 Theory

Figure 5.3 shows a schematic of the experimental setup used. Platinum (IV) chloride dissolved in DMSO (dimethyl sulfoxide) was used as the electrolyte to investigate the effect of tensile stress on Pt transport. When Pt wire/foil is immersed in $PtCl_4$+DMSO solution, the following chemical reaction (locally) is expected to take place

$$Pt + PtCl_4 \rightarrow 2\ PtCl_2 \tag{5.2}$$

since the standard Gibbs free energy change at room temperature for the above reaction is -23.02 $kJmol^{-1}$ [53]. The solubility of $PtCl_2$ in DMSO is very small. The electrolyte will

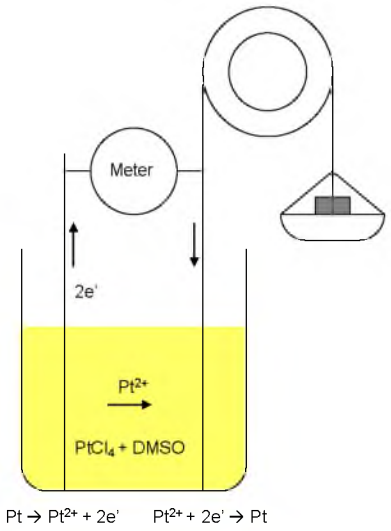

Figure 5.3: A schematic of the experimental setup used.

thus mainly contain Pt^{4+} ions with a small concentration of Pt^{2+}. When a tensile load is applied to one of the wires/foils, the chemical potential of Pt in the stressed wire/foil will decrease and platinum ions will initially transport from the unstressed platinum wire/foil to the stressed platinum wire/foil through the electrolyte. Negligible transport of electrons occurs under open circuit conditions since the *electronic* conductivity of the electrolyte is negligible. The transport of Pt^{2+} ions shuts down as soon as the electrochemical potentials of Pt^{2+} ions in both the stressed and the unstressed wires become equal, that is

$$\tilde{\mu}_{Pt^{2+}}^{unstressed} = \tilde{\mu}_{Pt^{2+}}^{stressed} \tag{5.3}$$

where $\tilde{\mu}_{Pt^{2+}} = \mu_{Pt^{2+}} + 2F\Phi$ is the electrochemical potential of Pt^{2+}, $\mu_{Pt^{2+}}$ is the chemical potential of Pt^{2+}, F is the Faraday constant, and Φ is the local electrostatic potential. Now, within platinum metal, the reaction $Pt \leftrightarrow Pt^{2+} + 2e'$ is at equilibrium. Thus,

$$\mu_{Pt} = \mu_{Pt^{2+}} + 2\mu_e = \tilde{\mu}_{Pt^{2+}} + 2\tilde{\mu}_e = \tilde{\mu}_{Pt^{2+}} - 2F\varphi \tag{5.4}$$

where,

$$\varphi = -\frac{\tilde{\mu}_e}{F} = -\frac{\mu_e}{F} + \Phi \qquad (5.5)$$

in which μ_e is the chemical potential of electrons, $\tilde{\mu}_e$ is the electrochemical potential of electrons, and φ is the experimentally measurable electric potential. Thus, the electrochemical potential of platinum ions in terms of the chemical potential of Pt and the measurable electric potential is given by

$$\tilde{\mu}_{Pt^{2+}} = \mu_{Pt} - 2\tilde{\mu}_e = \mu_{Pt} + 2F\varphi \qquad (5.6)$$

The electrochemical potentials of Pt^{2+} in the unstressed and the stressed Pt wires are given respectively by

$$\tilde{\mu}_{Pt^{2+}}^{unstressed} = \mu_{Pt}^{o} + 2F\varphi^{unstressed} \qquad (5.7)$$

and

$$\tilde{\mu}_{Pt^{2+}}^{stressed} = \mu_{Pt}^{o} + pV_m + 2F\varphi^{stressed} = \mu_{Pt} + 2F\varphi^{stressed} \qquad (5.8)$$

Substituting equations (5.7) and (5.8) into equation (5.3) gives

$$2F(\varphi^{stressed} - \varphi^{unstressed}) = -pV_m = -\left(\mu_{Pt} - \mu_{Pt}^{o}\right) \qquad (5.9)$$

and

$$(\varphi^{stressed} - \varphi^{unstressed}) = \Delta\varphi = -\frac{pV_m}{2F} = -\frac{\left(\mu_{Pt} - \mu_{Pt}^{o}\right)}{2F} \qquad (5.10)$$

That is, when a tensile load is applied, the hydrostatic pressure will be negative, which makes the stressed platinum wire positive (cathodic) – a sort of stress-induced cathodic protection.

5.3. Experimental Procedure

Figure 5.3 shows the experimental setup used. Two identical platinum wires of diameter 127 μm were partially immersed in 0.1 M platinum chloride ($PtCl_4$)+DMSO solution. The distance between the two wires was 1 mm. A tensile load was applied to one of the platinum wires using a pan tied to it and the other one was maintained stress-free. The wire attached to the pan was passed over a pulley. The load on the stressed wire was varied by adding several standard weights to the pan. The corresponding stress was varied between ~0 MPa and ~210 MPa. Any voltage created between the wires was measured using an electrometer (Keithley 6514) with a high input impedance (200 TeraΩ). In another experiment, an ammeter, capable of measuring current in the pA range, was connected between the two wires (effectively externally shorting the two wires) and the current passing through the external circuit was measured as a function of the applied mechanical load. The corresponding stress was varied between ~0 MPa and ~195 MPa. Similar experiments were also conducted using two identical platinum foils of thickness 127 μm and width 0.5 cm placed 1 mm apart, partially immersed in 0.1 M PtCl4+DMSO solution. Voltage (open circuit) and current (short circuit) were measured as a function of the applied stress ranging between 0 and 9 MPa.

In order to investigate the effect of stress on the kinetics of transport of platinum between the unstressed and the stressed wires/foils over a period of time, the same setup was used as above. Two identical platinum wires were partially immersed in the $PtCl_4$

electrolyte solution, separated by a distance of 1 mm. A constant tensile stress of 153 MPa was applied to one of the wires. The wires were electrically shorted externally to provide a path for electrons. The expectation was that platinum will dissolve at the unstressed wire and will deposit on the stressed wire. After 144 hours, the platinum wires were cleaned and examined under a scanning electron microscope (SEM). A similar experiment was also conducted using platinum foils of thickness 127 μm and width 0.5 cm. A tensile stress of 4.5 MPa was applied for 144 hours. The platinum foils were then cleaned and examined under an SEM.

Another set of experiments was conducted in which platinum wires ranging in diameters between 0.01 mm and 0.6 mm were used. In each experiment in this set, the two electrodes were of identical diameters. For a given wire diameter, the voltage between the stressed and the unstressed wires was measured as a function of the applied tensile stress. These experiments were conducted in order to determine the possible effect of the wire diameter on the dependence of voltage on the applied tensile stress.

5.4. Results and Discussion

5.4.1 Effect of Stress on Electrode Potential

Figures 5.4 and 5.5 show voltage (open circuit) and current (short circuit) vs. time plots for the experiments conducted on platinum wires under various applied tensile loads (stress ranging from 0 to 210 MPa). Under no applied load, the voltage across the two wires was near zero and it increased to ~3 mV as the applied stress was increased to 195 MPa. The wire under (tensile) stress became cathodic (positive). Similarly, the current (when shorted externally) varied between zero and ~2 nA when the applied tensile stress was varied between zero and ~210 MPa. In both experiments, as soon as the applied load

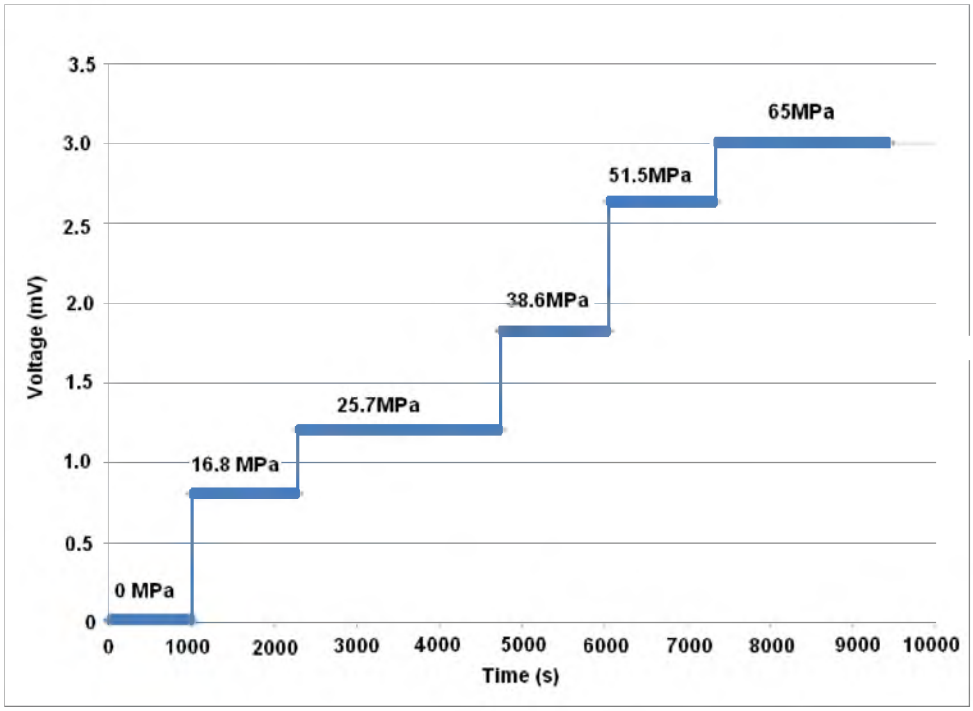

Figure 5.4: Variation of the voltage between the stressed (positive) and the unstressed Pt wires immersed in 0.1 M $PtCl_4$/DMSO solution for different applied loads.

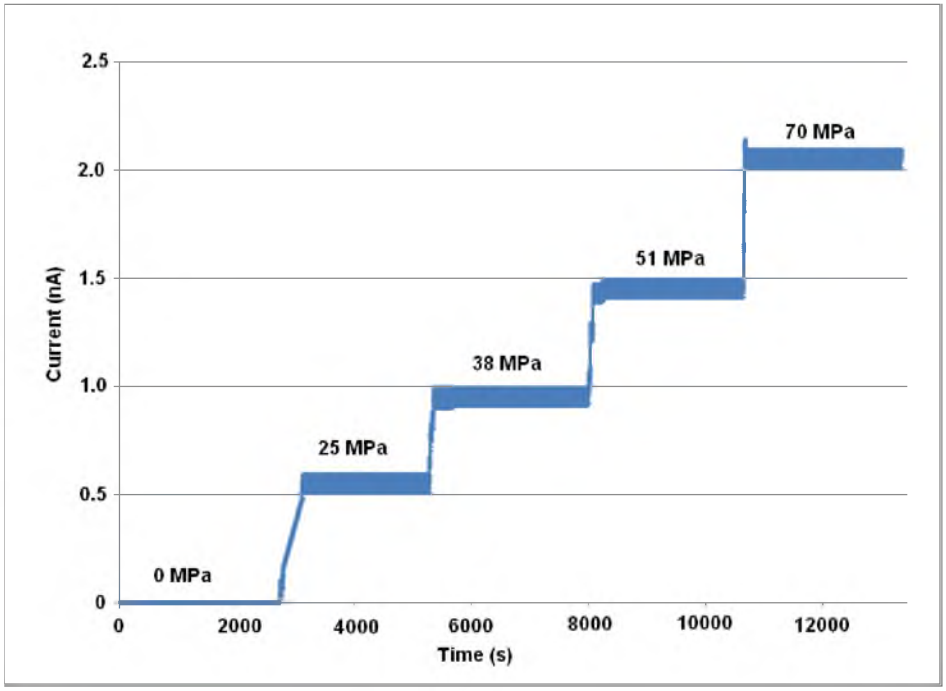

Figure 5.5: Variation of the current between the stressed and the unstressed platinum wires immersed in 0.1M $PtCl_4$/DMSO solution for different applied loads.

was changed, the voltage/current changed sharply and equilibrated almost instantaneously. Figure 5.6 shows the variation of the current between the stressed and the unstressed platinum foils as a function of time for different applied loads. The figure shows a discontinuity in the plot which is due to a temporary failure of the recording software. The higher measured current (as high as 170 nA) in the platinum foil experiment is attributed to the larger effective area of the foils as compared to the wires. It is also possible that the exchange current density on the wire surfaces was different than on foil surfaces due to possible differences in surface features/characteristics. Note that in this experiment also, the current stabilized instantaneously and remained stable for the duration over which the stress was maintained constant.

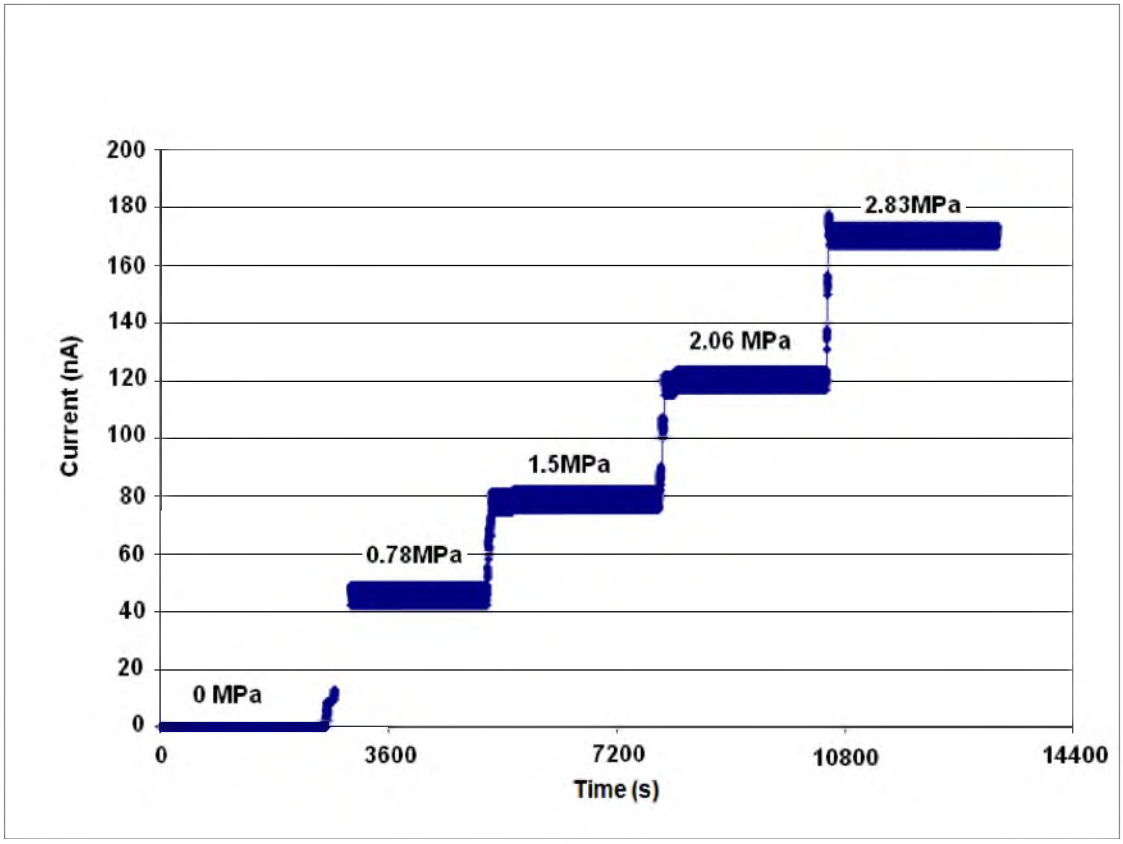

Figure 5.6: Variation of the current between the stressed and the unstressed Pt foils immersed in 0.1 M $PtCl_4$/DMSO solution for different applied loads.

Figure 5.7 shows plots of the measured voltage across the wires as a function of the applied tensile stress for various wire diameters. In each case, the measured voltage varies linearly with the applied stress. However, the voltage difference, $\Delta\varphi$, at a given stress is higher for wires of larger diameters. This observation can be explained on the basis of the linear elasticity theory [54]. For an elastic body under stress, the three principal stresses are σ_{xx}, σ_{yy}, and σ_{zz}. The corresponding hydrostatic pressure is given by [54]

$$p = -\frac{(\sigma_{xx} + \sigma_{yy} + \sigma_{zz})}{3} \tag{5.11}$$

The corresponding principal strains are related to principal stresses by [54]

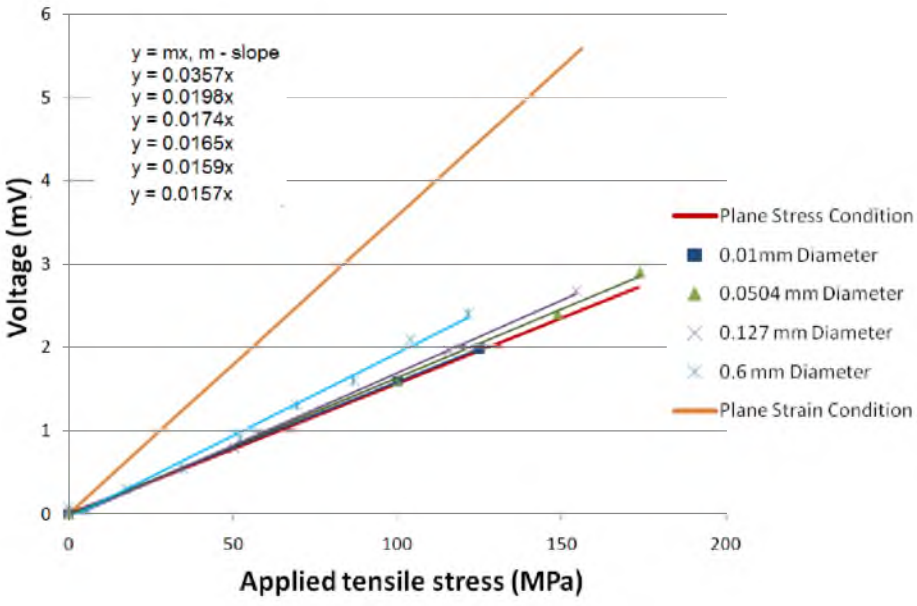

Figure 5.7: Voltage between the stressed (positive) and the unstressed wires as a function of the applied tensile stress for varying wire diameters. The intercept is ideally zero. In the fitting of the experimental data, the very small nonzero intercept was neglected in the voltage vs. stress equations given in the inset. Slopes give voltage coefficients per unit stress.

$$\varepsilon_{zz} = \frac{\sigma_{zz}}{E} - \frac{\nu}{E}\left(\sigma_{xx} + \sigma_{yy}\right) \tag{5.12}$$

$$\varepsilon_{xx} = \frac{\sigma_{xx}}{E} - \frac{\nu}{E}\left(\sigma_{yy} + \sigma_{zz}\right) \tag{5.13}$$

and

$$\varepsilon_{yy} = \frac{\sigma_{yy}}{E} - \frac{\nu}{E}\left(\sigma_{xx} + \sigma_{zz}\right) \tag{5.14}$$

where ν is the Poisson's ratio and E is the Young's modulus of elasticity. The two limiting cases in elasticity are of plane strain and plane stress [54] . Let us consider the application of a uniaxial load along the z direction. The corresponding stress is

$$\sigma_{zz} = \sigma \tag{5.15}$$

If plane strain conditions prevail,

$$\varepsilon_{yy} = \varepsilon_{xx} = 0 \quad \text{and} \quad \sigma_{yy} = \sigma_{xx} \tag{5.16}$$

Thus,

$$\varepsilon_{yy} = \varepsilon_{xx} = 0 = \frac{\sigma_{xx}}{E} - \frac{\nu}{E}\left(\sigma_{yy} + \sigma\right) = \frac{\sigma_{xx}}{E} - \frac{\nu}{E}\left(\sigma_{xx} + \sigma\right) \tag{5.17}$$

which gives

$$\sigma_{xx} = \sigma_{yy} = \frac{\nu\sigma}{(1-\nu)} \tag{5.18}$$

Substituting equations (5.15) and (5.18) into equation (5.11) and rearranging, the hydrostatic pressure is given by

$$p = -\left(\frac{1+\nu}{1-\nu}\right)\frac{\sigma}{3} \tag{5.19}$$

If plane stress conditions are assumed, however, $\sigma_{yy} = \sigma_{xx} = 0$, and the corresponding hydrostatic pressure in the wire is given by [54]

$$p = -\frac{\sigma}{3} \tag{5.20}$$

It is well known in the theory of elasticity that for very thin foils/wires, plane stress conditions prevail, and for very thick plates/rods, plane strain conditions prevail [54]. From equations (5.1), (5.10), and (5.20), the difference in the voltage between the stressed and the unstressed wires/foils under plane stress is given by

$$\frac{\left(\mu_{Pt}^{o} - \mu_{Pt}\right)}{2F} = \varphi(\sigma) - \varphi(0) = \Delta\varphi = \frac{V_m}{2F}\frac{\sigma}{3} = \frac{V_m}{6F}\sigma \tag{5.21}$$

where $\Delta\varphi$ is the voltage developed between the stressed and the unstressed wires/foils. Here, platinum ions are assumed to be in +2 oxidation state even when the salt used was $PtCl_4$, since locally a reaction between $PtCl_4$ and Pt is expected to form Pt^{2+}. The theoretically calculated slope of $\Delta\varphi$ vs. σ from equation (5.21) is 1.57 x 10^{-11} VPa^{-1}. For very thick wires, the prevailing state of stress will be that corresponding to plane strain. In such a case, the measured voltage will be given by

$$\varphi(\sigma) - \varphi(0) = \Delta\varphi = \frac{V_m}{2F}\frac{(1+\nu)\sigma}{(1-\nu)3} = \frac{V_m}{6F}\left(\frac{1+\nu}{1-\nu}\right)\sigma \tag{5.22}$$

For Pt, the Poisson's ratio is $\nu \approx 0.39$. The estimated slope for plane strain from equation (5.22) is 3.57 x 10^{-11} VPa^{-1}. The measured slopes of the plots in Figure 5.7 range between ~1.59 x 10^{-11} VPa^{-1} for a 10 micron wire diameter, which is close to the plane stress case,

and ~1.98 x 10^{-11} VPa^{-1} for a 0.6 mm wire diameter. Figure 5.8 shows the variation of the measured slopes or voltage coefficients per unit stress as a function of wire diameter. The increase in slope with increasing diameter is in accord with the predictions of the linear elasticity theory. The present results also show that a wire diameter of 0.6 mm is far below that required for plane strain conditions to prevail. It will be necessary to use rods of much larger diameters to reach plane strain conditions. This was beyond the practical range of the current experiments.

The present results also show that the dominant electrode reactions are Pt → Pt^{2+} + 2e' (anodic) at the unstressed wire/foil and Pt^{2+} + 2e' → Pt (cathodic) at the (tensile) stressed wire/foil even though the salt was $PtCl_4$.

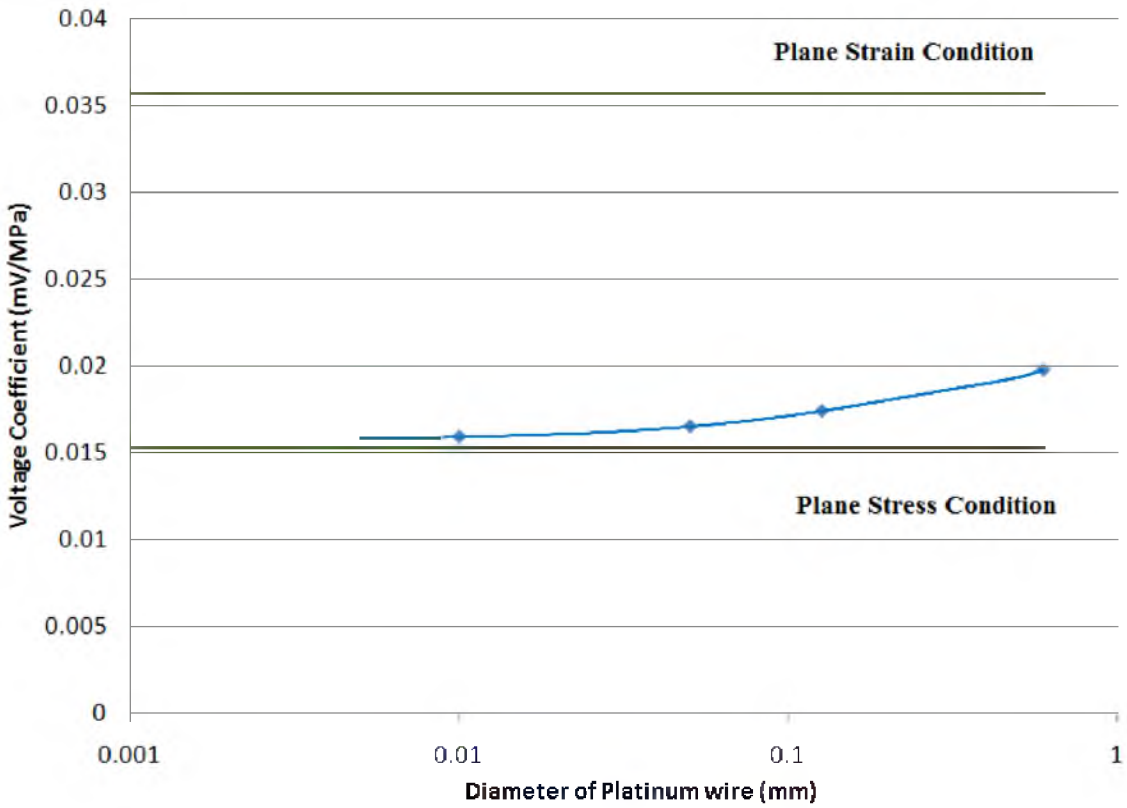

Figure 5.8: Variation of the voltage coefficient per unit stress as a function of the diameter of platinum wire.

If the dominant reactions had been Pt → Pt^{4+} + 4e' and Pt^{4+} + 4e' → Pt, the measured $\Delta\varphi$ would have been

$$\Delta\varphi = \frac{V_m}{12F}\sigma \tag{5.23}$$

or half the observed values. If both reactions had occurred to a comparable extent, the magnitude of the measured potential, $\Delta\varphi$, would have been between the values given by equation (5.23) and equation (5.21), resulting in mixed potential. The observation that the measurements are in agreement with equation (5.21) suggests that the present results were not influenced by any mixed potential effect.

5.4.2 SEM Observations of Wires and Foils

Figures 5.9(a) and 5.9(b) respectively show SEM micrographs of the unstressed and stressed platinum wires (externally shorted) after 144 hours of treatment in 0.1M $PtCl_4$+DMSO solution. The diameter of the unstressed platinum wire immersed in the solution shrank from 127 μm to 122 μm and that of the stressed wire increased from 127 μm to 134 μm. Figure 5.9(b) shows part of the stressed wire that was not immersed in the electrolyte; it exhibited no change in diameter. Figures 5.10(a) and 5.10(b) respectively show SEM micrographs of the cross-sections of the unstressed and the stressed platinum foils (externally shorted) after 144 hours of treatment in 0.1M $PtCl_4$+DMSO solution. The thickness of the unstressed foil shrank from 127 μm to 116 μm and that of the stressed foil increased from 127 μm to about 138 μm. Figure 5.10(a) shows the interface region where the top portion of the unstressed foil was outside the electrolyte and the bottom portion was immersed in the electrolyte. The volume of platinum deposited on the stressed wire/foil will be the same as the volume of platinum dissolved at the unstressed

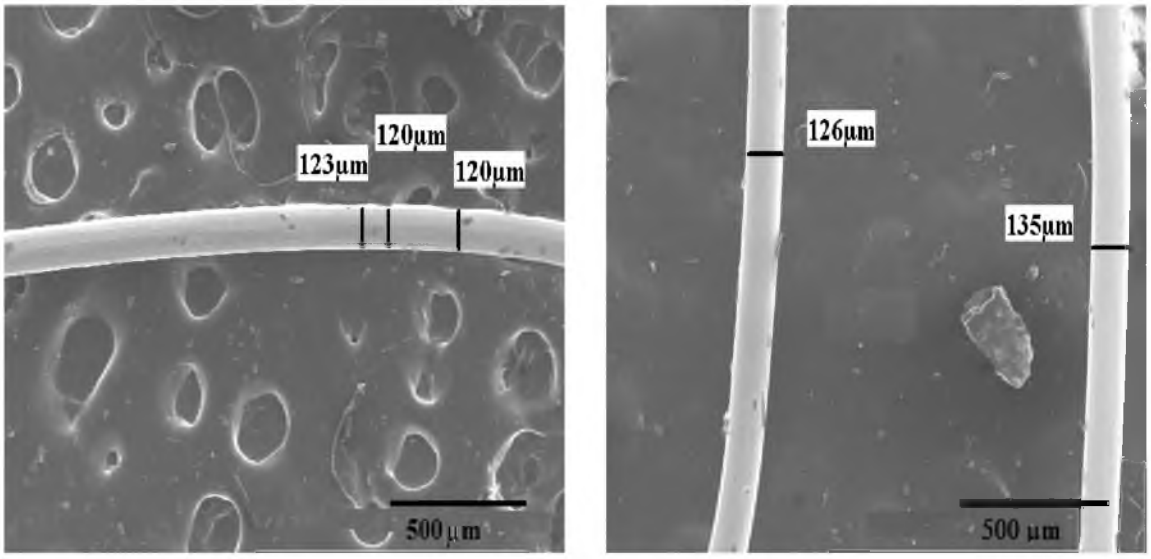

(a) (b)

Figure 5.9: SEM micrographs of: (a) Unstressed Pt wire immersed in 0.1 M $PtCl_4$+DMSO electrolyte for 144 hours. The wire diameter shrank to ~120µm. (b) Stressed Pt wire: The portion of Pt wire outside the electrolyte (no growth) and stressed Pt wire immersed in electrolyte – 135 µm (wire diameter grew to 135 µm).

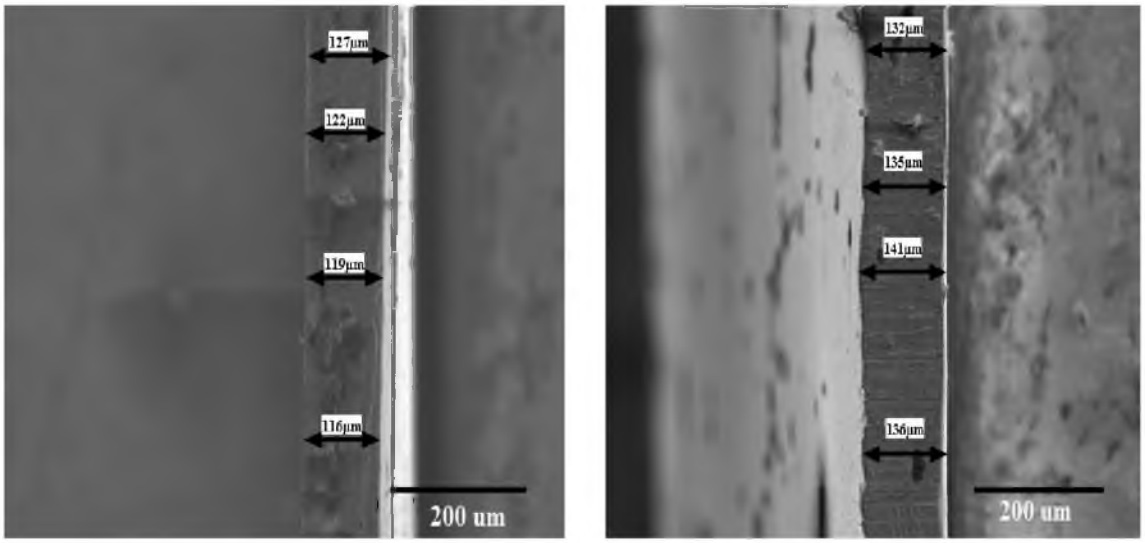

(a) (b)

Figure 5.10: SEM micrographs of foils immersed in 0.1 M $PtCl_4$/DMSO electrolyte for 144 hours. (a) Cross-section of the interface of the unstressed platinum foil where the top portion of the foil was outside the electrolyte (no change) and the bottom portion was immersed in the electrolyte (where dissolution occurred). The thickness reduced to ~116 µm. (b) Cross-section of stressed platinum foil immersed in the electrolyte. The thickness grew to ~136 µm.

wire/foil. In the experimental data, it seemed that the decrease in the unstressed wire diameter is less than the increase in the diameter of the stressed wire. Since the volume of Pt is conserved, this observation is attributed to the fact that the lengths of the wires immersed in the solution were not the same for the two wires.

5.4.3 The Sign of Stress/Potential and Chemical Potential

According to equation (5.21), the application of a tensile load/stress (leading to negative pressure) to a platinum wire/foil lowers the chemical potential of Pt compared to the unstressed wire/foil. In some of the literature, it has often been assumed (incorrectly) that applied stress always increases the chemical potential through the strain energy term [55]. This, however, is incorrect. Excellent discussion of this point has been given by Flood several decades ago [52]. The analysis by Flood [52] is in agreement with the original analysis by Gibbs which has often been ignored in more recent literature [55]. Also, experiments conducted on pure metals over 60 years ago are in accord with Flood's analysis [50,51] and in accord with predictions of thermodynamics. Thus, platinum ions tend to move from higher chemical potential of both neutral Pt and Pt^{2+} (unstressed wire/foil) to lower chemical potential of both neutral Pt and Pt^{2+} (wire/foil under a tensile stress). As the electron concentration is negligible in the electrolyte, no net transport of Pt takes place when no external path for electrons exists. The wire subjected to a tensile stress develops a positive potential (becomes cathodic) with respect to the unstressed wire. The equilibrium electric potential difference corresponds to the difference in chemical potentials of Pt and is given by equation (5.21) for plane stress (thin wire/foil) or equation (5.22) for plane strain (thick wire/foil). When an external path is provided for electrons by shorting the wires/foils, the circuit is completed; Pt ions move from the

unstressed wire/foil to the stressed (tensile) wire/foil through the electrolyte and electrons transport from the unstressed to the stressed (tensile) wire/foil in the external circuit. In this manner, net transport of neutral Pt occurs from the unstressed wire/foil to the stressed (tensile) wire/foil. This results in the thickening of the stressed (tensile) wire/foil and shrinking of the unstressed wire/foil, as observed in the present experiments. If the wire/foil had been stressed compressively (it would be more convenient to use a bar instead of wire/foil to prevent buckling), then the sign of the voltage developed would have been opposite; the compressively stressed one would have been negative (anodic). When connected externally, Pt transport would occur from the compressively stressed to the unstressed wire/foil.

5.5. Implications Concerning Core-Shell Catalysts for PEMFC

In PEMFC electrodes, catalyst particles are supported on an electronically conducting carbon support, which provides an electronic short. Particle growth occurs by a coupled transport of Pt ions through the liquid/ionomer and of electrons through the carbon support [48]. The present results and the preceding discussion suggest an approach for the synthesis of durable core-shell catalysts. Much of the reported work on core-shell catalysts has been primarily conducted with the objective of decreasing the Pt loading and also enhancing the catalyst activity [1,9,12,13]. While stability is well recognized as an important consideration, clear design strategies had not been defined until recently. Many recent studies have addressed stability of core-shell catalysts [16-19,22,25,28,34]. The majority of the studies are either experimental, in which catalyst performance is investigated using cyclic voltammetry, or theoretical, in which stability is inferred on the basis of DFT calculations [34]. The present results suggest that if a tensile

stress exists in the Pt shell (or a reduced compression as compared to a pure Pt particle), its chemical potential will be lowered and its stability against dissolution will be increased. In some core-shell catalyst studies, the nature of the core-shell interface has not been discussed in the literature. For example, in some studies, the Pt shell was deposited on cores of different crystal structure, leading to an incoherent interface. Figure 5.11 compares a monolithic Pt catalyst with core-shell catalyst having an incoherent interface. In such a case, the compressive stress in the Pt shell will be higher than in a monolithic Pt catalyst. The pressure is given by

$$p = \frac{2\gamma}{r} + \frac{2\gamma_{\text{int}} r_c}{r^2} \tag{5.24}$$

where r_c is the core radius, r is the outer radius, and γ_{int} is the interfacial energy between the core and the shell. If, however, the core-shell interface is perfectly coherent, γ_{int} is negligible, and if the lattice parameter of the core is larger than the Pt shell, such as

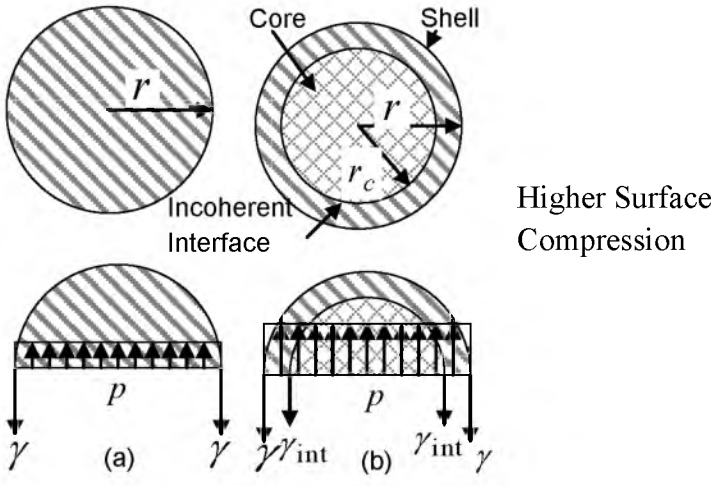

Figure 5.11: Schematics of monolithic and core-shell catalyst with an incoherent interface. Compressive stress in the shell is higher than the compressive stress in a monolithic catalyst particle. Such a catalyst should be less stable against dissolution compared to monolithic particle.

with Ag or Au core, the corresponding comparison between a monolithic Pt particle and a core-shell catalyst is shown in Figure 5.12. The corresponding stress state in the shell is given by

$$p(r) = \left(\frac{2\gamma}{r} - \frac{2\sigma_{\theta\theta}}{3} \right) \tag{5.25}$$

where $\sigma_{\theta\theta} = \sigma_{\phi\phi}$ are principal (angular) stresses in the shell [54]. At the surface , the state of stress is symmetric bi-axial (with the radial stress, σ_{rr}, on the surface of the shell being zero). The corresponding chemical potential of Pt in the shell is

$$\mu_{Pt}(r) = \mu_{Pt}^{o} + \left(\frac{2\gamma}{r} - \frac{2\sigma_{\theta\theta}}{3} \right) V_m \tag{5.26}$$

Note that if the shell is under a tension, $\sigma_{\theta\theta} = \sigma_{\phi\phi} > 0$. Thus, the chemical potential of Pt in the shell of such a core-shell catalyst is lower than the corresponding monolithic Pt catalyst particle of the same radius. The difference in chemical potential between the shell of a core-shell catalyst and a monolithic Pt catalyst is

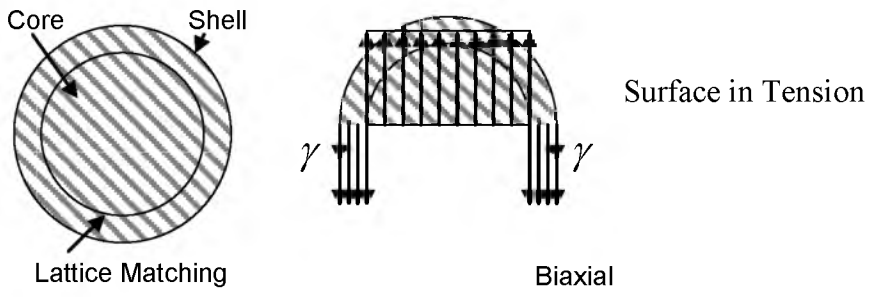

Figure 5.12: Schematic of a core-shell catalyst with a coherent interface. Compressive stress in the shell is lower than the compressive stress in a monolithic catalyst particle. Such a catalyst should be more stable against dissolution compared to monolithic particle.

$$\Delta\mu_{Pt}(r) = -\left(\frac{2\sigma_{\theta\theta}}{3}\right)V_m \tag{5.27}$$

If the core and the shell are of the same crystal structure, a coherent interface between the core and the shell is expected. Pt is f. c. c. (A1 structure). Other metals belonging to the same structure are Ag, Au, Cu, Pd, Ni, etc. Lattice parameters of Cu, Ni are smaller than that of Pt. Thus, core-shell catalyst made with these metals as the core will have the Pt shell in compression. This compressive stress will be in addition to the $2\gamma/r$ pressure created by the surface energy term. The prediction thus is that core-shell catalysts made with Cu or Ni as the core will tend to be less stable compared to pure Pt catalyst. If, however, core-shell catalysts are made with Ag or Au as the core which have larger lattice parameters than Pt, the Pt shell will be under a tensile stress (or reduced compression). Such core-shell catalysts will be more stable against dissolution compared to monolithic Pt catalysts.

The magnitude of the tensile stress in the Pt shell depends upon the difference in the lattice parameters, the elastic properties, and particle/shell dimensions. The lattice parameter of Pt is 0.3923 nm and that of Ag is 0.4086 nm. The corresponding strain in the shell of the core-shell catalyst is on the order of ~4%. The Young's modulus of Pt is 168 GPa. A hydrostatic tensile stress on the order of ~4 GPa can be expected in the shell of Pt. Such a high stress is possible if the interface is perfectly coherent with no dislocations. The corresponding EMF is given by $\Delta\varphi = \frac{\sigma_h V_m}{2F}$ or ~190 mV as compared to a monolithic Pt catalyst. This means a cathodic protection of core-shell catalysts by ~190 mV. This is a very significant effect. It implies that the stability of the Pt-shell Ag-core catalyst may be enhanced by ~190 mV in comparison to monolithic Pt catalysts.

Thus, core-shell catalysts with Ag as the core will lower the chemical potential of Pt in the shell. Therefore, the prediction is that Ag-core-Pt-shell catalysts will be more stable than pure Pt catalysts. Preliminary experiments have in fact shown that Ag/Pt core-shell catalysts are more stable than pure Pt catalysts [58].

Recently, Ramirez-Caballero et al. [34] conducted detailed DFT calculations of core-shell catalysts. In their work, relative stability of core-shell catalysts was investigated. In DFT calculations, the possible effects of stress are not separately accounted for. However, the energy minimization schemes include all effects, including the effect of stress. Ramirez-Caballero et al. [34] estimated that Pt-shell/Ag-core catalysts should increase the stability of core-shell catalysts by ~200 mV. Thus, these DFT calculations [34] and the results of continuum modeling based on thermodynamics presented here are in good agreement.

The lattice parameters of Au, Co, Ni, and Cu are, respectively, 0.40786 nm, 0.3544 nm, 0.35239 nm, and 0.36148 nm. Similar calculations as above give $\Delta\varphi = \frac{\sigma_h V_m}{2F}$ of ~180 mV, ~-500 mV, ~-520 mV, and ~-400 mV, respectively. That is, according to the present calculations, stability of Au@Pt will be enhanced by ~180 mV with respect to monolithic Pt catalysts. However, stability of Co@Pt, Ni@Pt, and Cu@Pt will be decreased by ~500 mV, ~520 mV, and ~400 mV, respectively. DFT calculations of Ramirez-Caballero et al. [34] show that for Au@Pt, the stability is increased by ~160 mV. By contrast, stabilities of Co@Pt, Ni@Pt, and Cu@Pt will be decreased by ~590 mV, ~600 mV, and ~84 mV, respectively. With the exception of the Cu@Pt, the results of present calculations based on a thermodynamic analysis are in good agreement with DFT calculations of Ramirez-Caballero et al. [34]. It is to be noted that the

thermodynamic analysis presented here can only address the effect of stress. It cannot, however, address possible chemical/electronic interactions between the shell and the core, which are included in the DFT calculations [34]. The comparison between the present work and the results of Ramirez-Caballero et al. [34] shows the probably the stress effect is more dominant. These results also show that thermodynamic modeling based on continuum modeling is useful for the design of materials and catalysts in the nanoscale range.

One of the factors which could affect the stability of core-shell catalysts with very thin shells is the possible diffusion of core atoms through the shell and reacting with the medium (e.g., water). This is an important factor in the possible degradation of most of the core-shell catalysts. An accurate estimate of the time required for diffusion through the shell is difficult to obtain for lack of diffusion data at the low operating temperatures of a typical PEMFC. However, a crude estimate may be made using high temperature data extrapolated to the PEMFC operating temperature of ~80°C. Rein et al. [59] have given self diffusion coefficients of Pt and of Au in Pt at relatively low temperatures. According to Rein et al. [59], the diffusion coefficients are given by $D^{Pt} = 0.05 \times \exp\left[-\frac{2.67eV}{k_B T}\right]$ cm^2s^{-1} and $D^{Au} = 0.13 \times \exp\left[-\frac{2.61eV}{k_B T}\right]$ cm^2s^{-1}. At 80°C, the estimated values of the diffusion coefficients are $D^{Pt} = 3.9 \times 10^{-40}\,\text{cm}^2\text{s}^{-1}$ and $D^{Au} = 7.2 \times 10^{-39}$ cm^2s^{-1}. These are exceptionally small values. Assuming parabolic dependence between diffusion distance, x, and time ($x^2 \approx Dt$), the estimated time for diffusion to occur through a shell of 1 nm thickness is very long indeed. Thus, if the shell fully covers the core, it appears unlikely that core-shell catalysts will degrade due to diffusion of metals through the shell. It is possible, however, that often the shell may not

completely cover the core or the core may dissolve. Under such conditions, degradation would be likely. If, however, Au is the core, degradation will likely not occur even when exposed to the liquid environment due to the stability of gold.

In the present work, a simple relation for the pressure generated due to surface energy, $2\gamma / r$, was assumed for nanosize particles. Many recent studies have used equations of state which incorporate crystallographic orientation dependence of surface energies. This is especially important for very small atom clusters, which display various shapes depending upon the number of atoms in the cluster [60-62]. However, there are also numerous studies on nanosize particles which assume an isotropic surface energy. This simple assumption is found to be quite reasonable for particles 2 nm and larger, as evidenced by their near spherical shape, typical of PEMFC catalysts. A more refined estimate, while still assuming isotropic surface energy, is the inclusion of the size dependence of the surface energy itself. For example, several studies have shown that for very small particles, γ itself is a function of the particle size , r, that is $\gamma(r)$ [63-65]. Then, the pressure created by the surface energy term is $2\gamma(r)/r$.

5.6. Summary

The effect of applied stress on the chemical potential of Pt was measured using an electrochemical cell. Two platinum wires/foils were immersed in a $PtCl_4$+DMSO solution. One of the wires/foils was subjected to a tensile stress while the other one was left load-free. It was observed that the wire/foil subjected to a tensile stress developed a positive electric potential compared to the unstressed one, indicating that the application of a tensile stress decreases the chemical potential of platinum. This result is in accord with the thermodynamic theory of Gibbs and the analysis given by Flood [52]. The

measured voltage coefficient per unit stress increased with increasing wire diameter. For wires of the smallest diameter used, the voltage coefficient per unit stress corresponded to the state of plane stress. The voltage developed per unit stress increased with increasing wire diameter. Increasing voltage coefficient per unit stress with increasing diameter is in accord with the predictions of linear elasticity that a transition from plane stress to plane strain should occur when using rods of a sufficiently large diameter. When the wires/foils were connected externally, the diameter/thickness of the one under tensile stress grew while the diameter/thickness of the unstressed one shrank.

These results suggest an approach for the development of stable cathode catalysts for PEMFC [66]. The present work shows that core-shell catalysts consisting of a core and Pt shell having the same crystal structures, the Pt shell having a smaller lattice parameter than the core, and the Pt shell epitaxially matched to the core will result in a tensile stress (or reduced compression) in the Pt shell. Such core-shell catalysts should be inherently more stable as the tensile stress in the Pt shell will lower its chemical potential and decrease its tendency for dissolution. The predictions of the stability of Ag@Pt core-shell catalysts based on the effect of tensile stress in the shell in the present work are consistent with DFT calculations reported in the literature [34]. Both the DFT calculations [34] and the present thermodynamic analysis predict a stability of Ag@Pt against dissolution by about ~190 mV. These results thus also show the usefulness of continuum thermodynamic modeling in the design of nanoscale materials.

5.7 Acknowledgements

This work was supported by the National Science Foundation under Grant Number CBET-0931080.

5.8 References

1. Y. Xu, A. V. Ruban and M. Mavrikakis, *J. Am. Chem. Soc.*, **126** (14) 4717 (2004).

2. R. Srivastava, P. Mani, N. Hanh, and P. Strasser, *Angewandte Chemie Int. Edition*, **46**(47), 8988 (2007).

3. T. Toda, H. Igarashi, M. Watnabe, *J. Electroanal. Chem.*, **460**(1,2) 258 (1999).

4. S. Mukerjee, S. Srinivasan, M. P. Soriaga, J. McBreen, *J. Electrochem. Soc.*, **142**(5) 1409 (1995).

5. K. Kinoshita, *Electrochemical Oxygen Technology*, p. 133, Wiley, New York (1992).

6. V. Jalan and E. J. Taylor, *J. Electrochem. Soc.*, **130**(11) 2299 (1983).

7. U. Koponen, H. Kumpulainen, M. Bergelin, J. Keskinen, T. Peltonen, M. Valkianen, and M. Wasberg, *J. Power Sources*, **118**(1-2) 325 (2003).

8. B. Gurau, R. Viswanathan, R. Liu, T. J. Lafrenz, K. L. Ley, E. S. Smotkin, E. Reddington, A. Sapienza, B. C. Chan, T. E. Mallouk, S. Sarangpani, *J. Phys. Chem. B*, **102**(49) 9997 (1998).

9. J. Zhang, F. Lima, M. Shao, K. Sasaki, J. Wang, J. Hanson, and R. Adzic, *J. Phys. Chem. B*, **109** 22701 (2005).

10. J. Zhai, M. Huang and S. Dong, *Electroanalysis* **19**(4), 506 (2007).

11. 'Electrode Catalyst for fuel cell and method for production thereof', S. Yamamoto, US Patent 7205255, Date of Issue: April 17, 2007.

12. W. Zhou and J. Y. Lee, *Electrochem. Comm.*, **9**(7), 1725 (2007).

13. P. Strasser, 'Platinum-rich shell, platinum poor core' Public release date: October 23, 2007, http://www.rsc.org/chemistryworld/News/2007/October/30100701.asp.

14. Z. D. Wei, Y. C. feng, L. Li, M. J. Liao, Y. Fu, C. X. Sun, Z. G. Shao, and P. K. Shen, *J. Power Sources*, **180**, 84 (2008).

15. S. Ball, S. L. Burton, E. Christian, A. Davies, R. O'Malley, S. Passot, B. Tessier, B. R. C. Theobald, and D. Thompsett, *ECS Trans.*, **25**(1) 1011 (2009).

16. R. R. Adzic, J. Zhang, K. Sasaki, M. B. Vukmirovic, M. Shao, J. X. Wang, A. U. Nilekar, M. Mavrikakis, J. A. Valerio, and F. Uribe, *Top Catal.*, **46**, 249 (2007).

17. W. Zhou and J. Y. Lee, *Electrochem. Comm.*, **9** 1725 (2007).

18. B. Fang, B. N. Wanjala, X. Hu, J. last, R. Loukrapam, J. Yin, J. Luo, and C-J. Zhong, *J. Power Sources*, **196**, 659 (2011).

19. P. Hirunsit and P. B. Balbuena, *J. Phys. Chem. C*, **114**, 13055 (2010).

20. J. K. Norskov, T. Bligaard, J. Rossmeisl, and C. H. Christensen, *Nature Chem.*, **1** 37 (2009).

21. J. Zhai, M. Huang and S. Dong, *Electroanal.*, **19**, 506 (2007).

22. Y. Ma and P. B. Balbuena, *J. Electrochem. Soc.*, **157**(6), B959 (2010).

23. S. Zhou, G. S. Jackson, and B. Eichhorn, *Adv. Funct. Mater.*, **17**, 3099 (2007).

24. Z. Peng and H. Yang, *Nano Res* **2**, 406 (2009).

25. Y. Xing, Y. Cai, M. B. Vukmirovic, W-P. Zhou, H. Karan, J. X. Wang and R. A. Adzic, *J. Phys. Chem. Lett.*, **1**, 3238 (2010).

26. Y. Chen, F. Yang, Y. Dai, W. Wang, and S. Chen, *J. Phys. Chem. C*, **112**, 1645 (2008).

27. Z. Yang, J. Y. Yang, Q. Zhang, W. Zhou, and Z. Liu, *J. Electrochem. Soc.*, **155**(7), B776 (2008).

28. R. Srivastava, P. Mani, N. Hahn, and P. Strasser, *Angew. Chem. Int. Ed.*, **46**, 8988 (2007).

29. Y. Ma, H. Zhang, H. Zhing, T. Xu, H. Jin and X. Geng, *Catal. Comm.*, **11**, 434 (2010).

30. B. C. Tessier, A. E. Russell, B. Theobald, and D. Thompsett, *ECS Trans.*, **16**(37), 1 (2009).

31. P. P. Wells, E. M. Crabb, C. R. King, R. Wiltshire, B. Billsborrow, D. Thompsett, and A. E. Russell, *Phys. Chem. Chem. Phys.*, **11**, 5773 (2009).

32. Z. Liu, G. S. Jackson, and B. W. Eichhorn, *Angew. Chem.* **122**, 3241 (2010).

33. S. Koh, J. Leisch, M. F. Toney and P. Strasser, *J. Phys. Chem. C*, **111**, 3744 (2007).

34. G. E. Ramirez-Caballero, Y. Ma, R. Callejas-Tovar, and P. B. Balbuena, *Phys. Chem. Chem. Phys.*, **12**, 2209 (2010).

35. M. S. Wilson, F. H. Garzon, K. E. Sickhaus and S. Gottesfeld, *J. Electrochem. Soc.*, **140**(10), 2872 (1993)

36. R. Ornelas, A. Stassi, E. Modica, A. S. Arico, and V. Antonucci, *ECS Trans.*, **3**(1), 633 (2006).

37. X. Wang, R. Kumar, and D. Meyers, *J. Electrochem. Solid State Lett.* **9**(5), A225 (2006).

38. J. Xie, D. L. Wood, III, K. L. More, P. Atanassov, and R. L. Borup, *J. Electrochem. Soc.*, **152**(5), A1011 (2005).

39. P. J. Ferreira, G. J. Lao, Y. Shao-Horn, D. Morgan, R. Makharia, S. Kocha and H. A. Gasteiger, *J. Electrochem. Soc.*, **152**(11), A2256 (2005).

40. W. Bi, G. E. Gray and T. F. Fuller, *Electrochem and Solid-State Lett.*, **10**(5), B101 (2007).

41. K. Yasuda, A. Taniguchi, T. Akita, and Z. Siroma, *Phys. Chem. Chem. Phys.*, **8**, 746 (2006).

42. A. Ohma, S. Suga, S. Yamamoto, and K. Shinohara, ECS Trans., **3**(1), 519 (2006).

43. H. Liu, J. Zhang, F. D. Coms, W. Gu, B. Litteer, and H. A. Gasteiger, *ECS Trans.*, **3**(1), 493 (2006).

44. A. Laconti, H. Liu, C. Mittelsteadt, and R. McDonald, ECS Trans., **1**(8), 199 (2005).

45. B. Merzougui and S. Swathirajan, *J. Electrochem. Soc.*, **153**(12), A2220 (2006).

46. K. L. More, R. Borup, and K. S. Reeves, *ECS Trans.*, **3**(1), 717 (2006).

47. R. Darling and J. Meyers, *J. Electrochem. Soc.*, **150**(11), A1523 (2003).

48. A. V. Virkar and Y. Zhou, *J. Electrochem. Soc.*, **154**(6), B540 (2007).

49. O. F. Devereux, *Topics in Metallurgical Thermodynamics*, John Wiley-Interscience, New York (1983).

50. R. E. Fryxell and N. H. Nachtrieb, *J. Electrochem. Soc.*, **99**, 495 (1952).

51. S. Tan and K. Nobe, *Can. J. Chem.*, **41**, 495 (1963).

52. E. A. Flood, *Can J. Chem.*, **36**, 1332 (1958).

53. I. Barin, *Thermochemical Data of Pure Substances. Part II*, VCH Publication, Germany (1993).

54. S. P. Timoshenko and J. N. Goodier, *Theory of Elasticity*, McGraw-Hill, New York (1970).

55. A. Horvath and R. Schiller, *Phys. Chem. Chem. Phys.*, **3**, 2662 (2001).

56. S. Yamamoto, 'Electrode Catalyst for fuel cell and method for production thereof', US Patent 7205255, Date of Issue: April 17, 2007.

57. S. Yamamoto, 'Electrode Catalyst for fuel cell and method for production thereof', US Patent 7205255, Date of Issue: April 17, 2007.

58. J-H. Koh, R. Abbaraju, N. Dasgupta, and A. V. Virkar, unpublished work (2009).

59. G. Rein, H. Mehrer, *Mater, Phys. Sta. Sol.*, **45**, 253 (1978).

60. R. V. Chepulski and S. Curtarolo, *ACS Nano*, **5**(1), 247 (2011).

61. S-P. Huang and P. B. Balbuena, *Molecular Physics*, **100**(13), 2165 (2002).

62. X. Shao, X. Wu, and W. Cai, *J. Phys. Chem. A*, **114**, 12813 (2010).

63. A. N. Goldstein, C. M. Echer, and A. P. Alivisatos, *Science*, **256**, 1425 (1992).

64. H. Hofmeister, S. Thiel, M. Dubiel and E. Schurig, *Appl. Phys. Lett.*, **70,** 1694 (1997).

65. K.K. Nanda, A. Maisels, F. E. Kruis, H. Fissan and S. Stappert, *Phys. Rev. Letters*, **91**(10), 106102-1 (2003).

66. A. V. Virkar, 'Core-Shell Patent', US. Patent Application No. 20100062929 (filed 2008).

CHAPTER 6

SPECIFIC SURFACE ENERGY AND SHAPE STABILITY OF FACE CENTERED CUBIC METALS AS A FUNCTION OF SIZE

6.1 Introduction

Many properties of materials are known to depend upon the size for particles in the sub-nano to nano size range. Beyond some sizes, properties approach those corresponding to bulk materials. One such property of materials which depends on size in the sub-nano to nano size range is the specific surface energy (γ), which represents the work done in breaking bonds and creating new surfaces. Thus, specific surface energy depends on the number of unsatisfied bonds/unit area on the surface of a particle. For sufficiently large particles, specific surface energy is a constant and is considered a material property. The specific surface energy of a metal can be estimated from the bond energy and the lattice constants. This approach is known as the broken-bond model or the cleaved–bond model of specific surface energy [1]. This method has been used for many years for estimating surface energies of solids from atomization (sublimation) energies. Such an approach is considered reasonably accurate as long as bonding can be adequately described in terms of the nearest neighbor interactions. Experimental measurement of specific surface energies of solids is generally difficult. The typical approach consists of conducting experiments at a high temperature in which the surface tension of a liquid is

measured and is extrapolated to 0K [2, 3]. Both theoretical and experimental approaches have been used over the years to estimate specific surface energies of solids [4-8].

Considerable research is underway on the calculation of specific surface energies of metals using either ab initio techniques [9-12] or empirical methods [13]. These calculations have primarily been conducted for body centered cubic and face centered cubic metals. Methfessel et al. [9] studied transition metals using the full-potential (FP) linear muffin-tin orbital (LMTO) method, taking into account the local spin density. Another technique employed is the Density Functional Theory (DFT) using Green's function within the LMTO method [10, 11, 14, 15]. More recent studies have been conducted using a DFT technique in the Generalized Gradient Approximation (GGA). This technique has been used for large sets of data and has been applied to about 60 elements in the periodic table [16-23]. Many researchers have also estimated specific surface energies of several crystallographic facets of transition metals and noble metals using the traditional broken-bond model [24-27]. Galanakis et al. have shown that precise ab initio calculations lead to the conclusion that specific surface energies of noble metals can be accurately described in terms of the broken-bond model [26]. Specifically, these authors have shown that the anisotropy ratio (ratio of specific surface energies of crystallographically different planes such as (111) and (100)) depends upon the number of unsatisfied bonds on the surfaces.

Even though atomistic modeling or first principles methods are used to investigate structure, surface properties, and thermodynamics of various systems, often the calculations are restricted to a small cluster of atoms to minimize computational times. Additionally, in most studies, reliance on experimental parameters has been necessary in ab initio calculations. For example, Galanakis [26] used the experimentally measured

lattice parameters. Recent work by Chepulskii and Curtarolo [28] examined stability of very small clusters of Pt. In their work, ab initio calculations were performed on very small atom clusters and a variational, continuum approach was used for larger particles. Some particle shapes, e.g., tetrahexahedron with {730} facets, were not amenable to ab initio calculations as even the smallest tetrahexahedral particle contains more atoms than can be treated by the ab initio method [28]. The variational approach used by Chepulskii and Curtarolo [28] for large crystals was also extended down in the very small size range to afford a comparison between the ab initio and the variational approaches. In the study by Chepulskii and Curtarolo [28], entropy effects as well as zero point vibration energy were ignored in their ab initio calculations. Also, in their variational approach, edges and corners were ignored.

The observation in the study by Galanakis et al. [26] that ab initio calculations confirm the validity of the simple broken-bond model has important implications concerning the study of specific surface energies of small particles and their shape stability. It suggests that the traditional broken-bond model may in fact be applicable over a very wide range of particle sizes – from very small all the way up to very large (bulk) crystals. The experimentally measured parameters that can be used in the broken-bond model are the enthalpy of sublimation and the lattice parameter.

The objective of the present work was to explore the applicability of the broken-bond model to the investigation of the effect of size on the specific surface energy of face centered cubic metals. Using the broken-bond model, various particle shapes are investigated from the smallest possible size to infinitely large size (bulk materials). The shapes investigated in the present work are: cube, cubo-octahedron, tetrahedron, octahedron, and truncated octahedron. Thus, all shapes examined here have {111} and/or

{100} planes as the crystal facets. Based on these calculations, relative stabilities of various shapes as a function of size are examined. The results of the present calculations are then compared with recent literature in which ab initio and variational approaches were used [28]. The present results are also compared with computational work by Vitos et al. [16].

In all cases (but one), calculations are made for particles of any given complete shape. Thus, in the very small size range, a direct comparison between specific surface energies of two different shapes cannot be made due to differing numbers of atoms necessary to form the corresponding complete shapes. For example, the smallest octahedron contains 6 atoms, but the smallest cube requires 14 atoms. In one case, specific surface energy is evaluated between two successive sizes of particles of a given shape by sequentially adding atoms on the smaller sized particle. These calculations give insight into the variation of specific surface energy as a function of size when the particles do not form complete shapes, such as would be expected during growth.

On the basis of a continuum thermodynamic model, Tolman [29] had predicted the existence of a critical length above which surface tension is a constant. Below this critical radius, it was predicted that surface tension varies with size. On the basis of the number of unsatisfied bonds/unit surface area, one would expect specific surface energy to increase with decreasing size, in accord with the considerable literature on this topic. There is also literature which suggests a decrease in surface energy with decreasing size [30]. Koga et al. [31] have examined the validity of Tolman's critical length using DFT. However, as indicated by Koga et al. [31], the sign of the critical length has not been unequivocally determined. Reference to Tolman's work is made here for completeness. The present calculations are based on the broken-bond model (with the possible

redistribution of bonding electrons ignored) and thus the expectation is that for very small particles, the specific surface energy should be greater than for large particles.

6.2 Theory

In the broken-bond model discussed here, only the nearest neighbor interactions are taken into account. The model assumes an elemental solid of a face centered cubic structure. Thus, each atom is assumed to have 12 bonds (coordination number – 12). An atom in the bulk has all 12 bonds satisfied. An atom on {100} surfaces of a particle has 4 unsatisfied bonds.

The smallest cube-shaped crystal has the size of a unit cell and contains 14 atoms arranged in a face centered cubic structure (Figure 6.1) having a lattice parameter 'a'. All schematics of crystals shown in this work were drawn using the Crystal Maker Software. An important assumption in the broken-bond model is the assignment of discrete bonds with the nearest neighbors; for example, 12 for a bulk atom in an f.c.c. metal. Atoms on surfaces, edges, and corners have a number of bonds unsatisfied. This number is approximately related to the solid angle subtended by the surrounding unfilled sites (vacuum). The present calculations also ignore the possible redistribution of electrons that may occur when particles are small. If a redistribution of electrons does occur at small sizes, one would also expect redistribution of bonds. Recent calculations by Methfessel et al. [32], however, have shown that electron density distribution is slightly different only in the exposed part of the first layer of a crystal. Below the first layer, the electron density distribution is essentially the same as in the bulk of the crystal. Thus, it is the expectation that the effect related to redistribution of electrons is likely to be rather small. Let ε be the bond energy of one unsatisfied bond. As-defined, when a bond forms

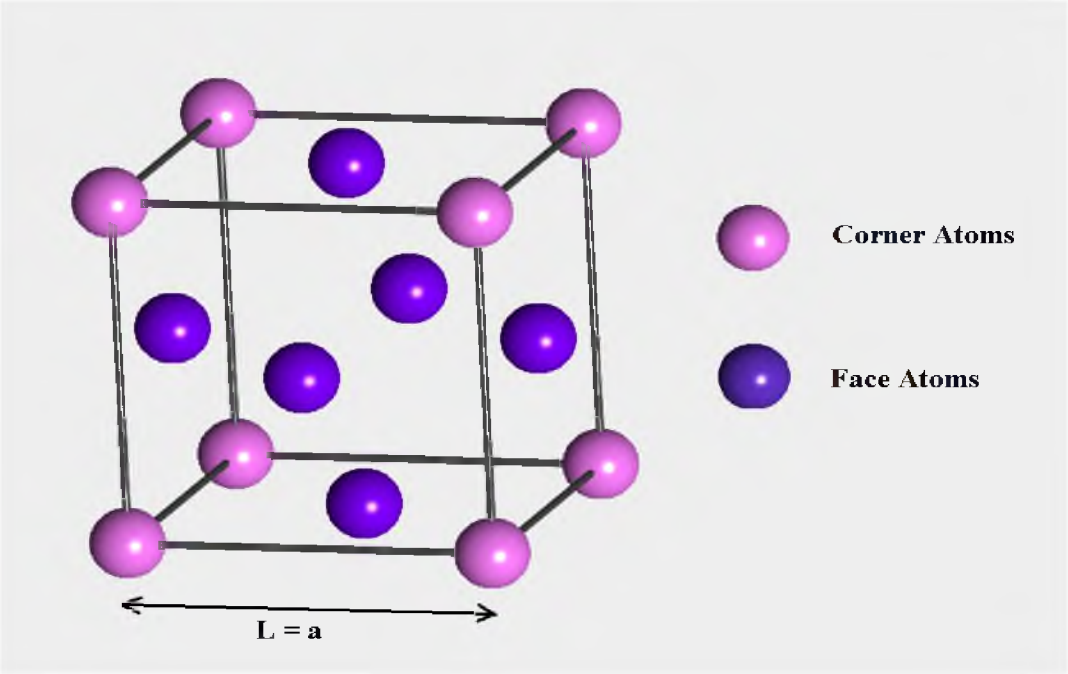

Figure 6.1: The smallest crystal of the size of a unit cell with a face centered cubic structure and lattice parameter, 'a'

between two atoms, the corresponding energy released in bond formation is 2ε. Each atom in the bulk forms 12 bonds with its neighbors. Thus, in this notation, the molar heat of sublimation is given by

$\Delta H_{subl} = 12 N_A \varepsilon$ where N_A is the Avogadro number.

The total number of unsatisfied bonds on a cube-shaped crystal of the size of a unit cell as shown in Figure 6.1 is 96.

Total energy of unsatisfied bonds = 96ε

The total surface area of the cube = $6a^2$

Thus, the specific surface energy of a cube of the size of a unit cell is given by

$$"\gamma = \frac{96\varepsilon}{6a^2} = 16\frac{\varepsilon}{a^2} = \frac{16}{a^2}\frac{\Delta H_{subl}}{12N_A} = \frac{4}{3}\frac{\Delta H_{subl}}{N_A a^2} \qquad (6.1)$$

All final results are given in terms of the molar heat of sublimation, ΔH_{subl}. In what follows, we present general expressions for the number of unsatisfied bonds on the surfaces of particles of various shapes. Atoms on the surface are listed in three categories; surface atoms, edge atoms, and corner atoms. The number of unsatisfied bonds on the surfaces, along the edges, and on the corners depends upon on the shape (Miller indices of the surfaces, Miller indices of the two intersecting planes forming edges, and Miller indices of the three intersecting planes forming corners). For very large particles, there is little effect of edges and corners and the specific surface energy is dictated by crystal facets. However, for very small particles, edge and corner atoms play an important role, and in fact, in some cases, the dominant role. Thus, for very small particles, edges and corners cannot be neglected.

6.2.1. General Expression for a Cube-shaped Particle

We consider a cube-shaped particle with side length, $L = Na$, where N is the number of unit cells on a side of the cube. The number of unsatisfied bonds/atom for {100} surface atoms is 4, that for <100> edge atoms is 7, and that for corner atoms is 9. Figure 6.2 shows a cube-shaped particle of length $L = 2a$.

The regression relation for the number of atoms on the surface of a cube-shaped particle is $6\left(2N^2 - 2N + 1\right)$ and that for edge atoms is $12\left(N - 1\right)$. There are eight corner atoms for a cube-shaped particle. The net surface area is $6N^2a^2$.

Specific surface energy is thus given by the total energy corresponding to the unsatisfied bonds on the surfaces, the edges, and the corners divided by the surface area, which is given by

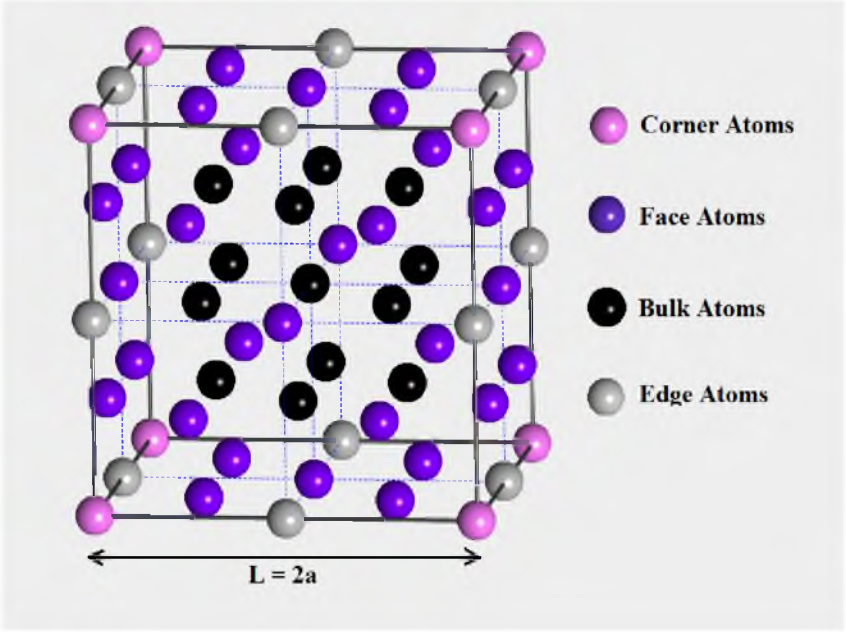

Figure 6.2: A cube-shaped particle of side length L = 2a

$$\gamma(N)=\frac{12\{4N^2+3N+1\}\varepsilon}{6N^2a^2}=\frac{2\varepsilon}{a^2}\left\{4+\frac{3}{N}+\frac{1}{N^2}\right\}=\frac{2\Delta H_{subl}}{3N_Aa^2}\left\{1+\frac{3}{4N}+\frac{1}{4N^2}\right\}^{1} \tag{6.2}$$

For very large particles ($N\to\infty$), the specific surface energy is given by

$$\gamma=\frac{2\Delta H_{subl}}{3N_Aa^2}=0.6667\frac{\Delta H_{subl}}{N_Aa^2} \tag{6.3}$$

Thus, the specific surface energy decreases as the particle size increases. The largest value of the specific surface energy is 1.33 $\frac{\Delta H_{subl}}{N_Aa^2}$, corresponding to a cube containing 14 atoms, while the smallest value is 0.667 $\frac{\Delta H_{subl}}{N_Aa^2}$. That is, γ of the smallest cube-shaped particle is two times the specific surface energy of very large cube-shaped crystals.

[1] Details of calculations are given in the Appendix.

6.2.2 General Expression for a Cubo-octahedron Shaped Particle

We consider a particle in the shape of a cubo-octahedron, which is a truncated cube. Figure 6.3 shows a cubo-octahedron formed by truncating a cube of length $L = 2a$.

Note that this is the smallest possible cubo-octahedron. Also note that N must be an even number. In this case, there are four different types of surface atoms: atoms on square {100} surfaces with 4 unsatisfied bonds/atom, atoms on triangular {111} surfaces with 3 unsatisfied bonds/atom, $<1\bar{1}0>$ edge atoms with 5 unsatisfied bonds/atom, and finally, corner atoms with 7 unsatisfied bonds/atom. The volume of a cubo-octahedron carved out of a cube of edge length L is $(5/6)L^3$. Following the same procedure as before (Appendix), the specific surface energy is given by

$$\gamma(N) = \frac{12\varepsilon}{a^2}\left\{\frac{3N^2 + 3N + 1}{\left(3+\sqrt{3}\right)N^2}\right\} \tag{6.4}$$

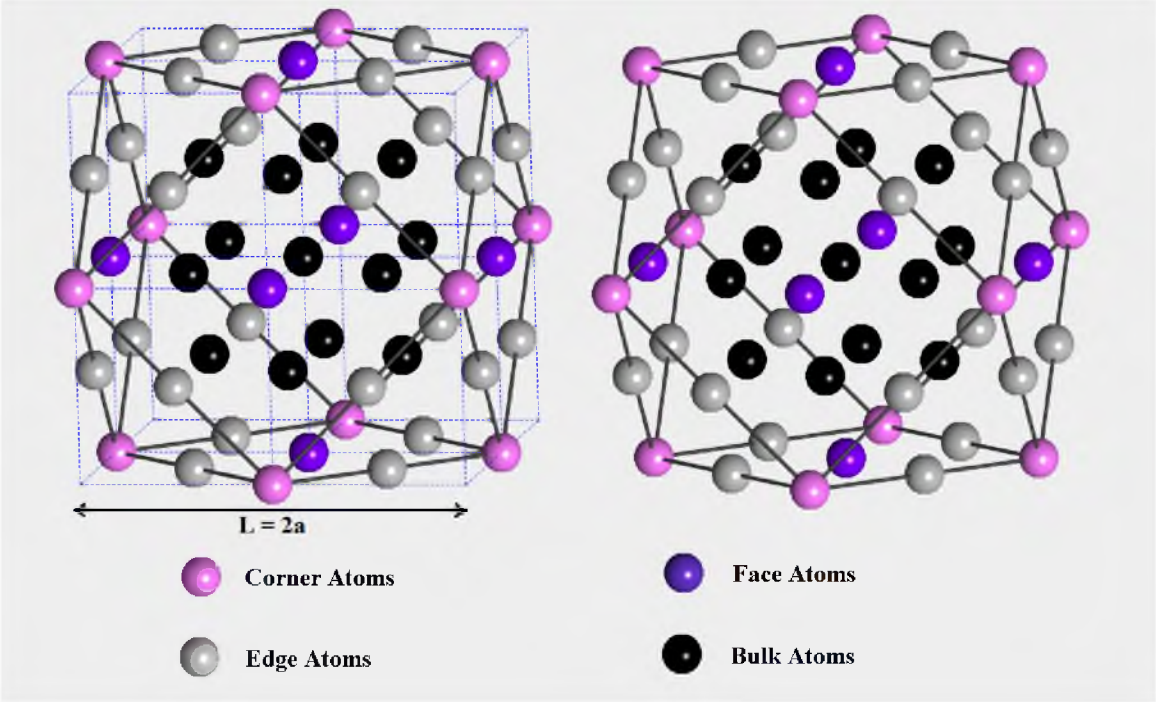

Figure 6.3: A cubo-octahedron of side length L = 2a

$$= \frac{12\varepsilon}{\left(3+\sqrt{3}\right)a^2}\left\{3+\frac{3}{N}+\frac{1}{N^2}\right\} = \frac{3\Delta H_{subl}}{\left(3+\sqrt{3}\right)N_A a^2}\left\{1+\frac{1}{N}+\frac{1}{3N^2}\right\} \tag{6.5}$$

The smallest value of N is 2. The corresponding smallest number of atoms is 55. Thus, the specific surface energy of a cubo-octahedron of the smallest possible size is

$$\gamma(N=2) = \frac{3\Delta H_{subl}}{\left(3+\sqrt{3}\right)N_A a^2}\left\{\frac{19}{12}\right\} \tag{6.6}$$

The specific surface energy of a cubo-octahedron of a very large size ($N \to \infty$) is given by

$$\gamma = \frac{3\Delta H_{subl}}{\left(3+\sqrt{3}\right)N_A a^2} = 0.634\frac{\Delta H_{subl}}{N_A a^2} \tag{6.7}$$

Thus, the ratio of the specific surface energy of a cubo-octahedron of the smallest size to that of a very large particle is 19/12. A comparison of equations (6.3) and (6.7) shows that we expect a cubo-octahedron to be more stable than a cube when the particle size is sufficiently large. In fact, this is true over the entire range. However, if a cluster contains fewer than 55 atoms, a comparison of particles of incomplete shapes with other shapes will need to be made to determine stability, since a complete cubo-octahedron cannot be formed with fewer than 55 atoms.

6.2.3 General Expression for a Tetrahedron-shaped Particle

We consider a particle in the shape of a tetrahedron cut out of a cube. Figure 6.4 shows a tetrahedron cut out of a cube of length $L = 2a$. The smallest tetrahedron can be

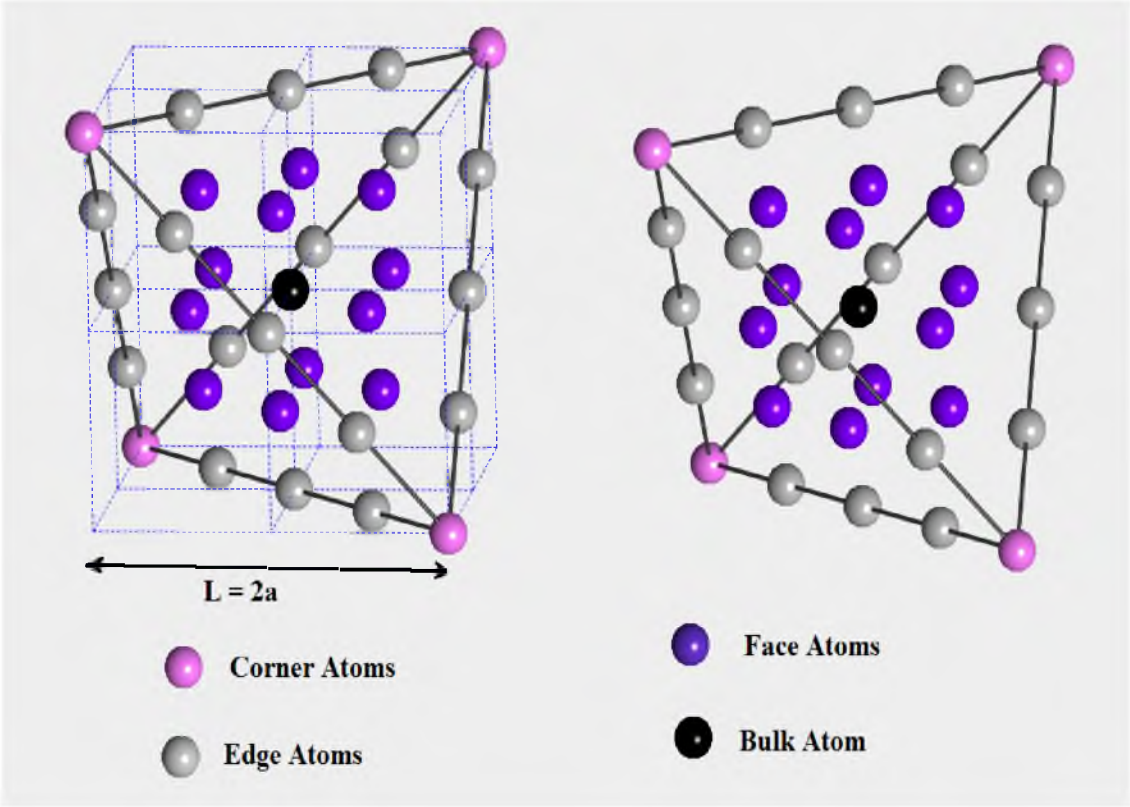

Figure 6.4: A tetrahedron of side length L = 2a

created with $L = 1a$. A tetrahedron is formed by four {111} triangular faces having 3 unsatisfied bonds/atom, edge atoms with 6 unsatisfied bonds/atom, and corner atoms with 9 unsatisfied bonds/atom. The volume of a tetrahedron of length L is $\frac{L^3}{3}$.

Following the same procedure as before (Appendix), the specific surface energy is given by

$$\gamma(N) = \frac{\varepsilon}{a^2}\left\{\frac{24N^2 + 36N + 12}{2(\sqrt{3})N^2}\right\} \tag{6.8}$$

$$= \frac{6\varepsilon}{(\sqrt{3})a^2}\left\{2 + \frac{3}{N} + \frac{1}{N^2}\right\} = \frac{\Delta H_{subl}}{\sqrt{3}N_A a^2}\left\{1 + \frac{3}{2N} + \frac{1}{2N^2}\right\} \tag{6.9}$$

For very large particles, $N \to \infty$, the specific surface energy is given by

$$\gamma = \frac{\Delta H_{subl}}{\sqrt{3} N_A a^2} = 0.5774 \frac{\Delta H_{subl}}{N_A a^2} \tag{6.10}$$

which is the specific surface energy of a large tetrahedron. The smallest value of $N = 1$. The corresponding number of atoms is 10. Thus, according to equation (6.9)

$$\gamma(N = 1) = 3 \frac{\Delta H_{subl}}{\sqrt{3} N_A a^2} = \frac{\sqrt{3} \Delta H_{subl}}{N_A a^2} \tag{6.11}$$

That is, the smallest tetrahedron has 3 times the specific surface energy of a large tetrahedron. A comparison of equations (6.7) and (6.10) shows that for large particles, the stable shape is a tetrahedron and the intuitively expected cubo-octahedron (which is closer to a spherical shape) exhibits higher specific surface energy.

6.2.4 General Expression for an Octahedron-shaped Particle

We consider a particle in the shape of an octahedron cut out of a cube. Figure 6.5 shows an octahedron cut out of a cube of length $L = a$, and an octahedron cut out of a cube of $L = 2a$. An octahedron is formed by eight {111} triangular faces with 3 unsatisfied bonds/atom, edge atoms with 5 unsatisfied bonds/atom, and corner atoms with 8 unsatisfied bonds/atom. The volume of an octahedron of length L is $\frac{L^3}{6}$.

Following the same procedure as before (Appendix), the specific surface energy of an octahedron is given by

$$\gamma(N) = \frac{\varepsilon}{a^2} \left\{ \frac{12N^2 + 4N + 32}{\left(\sqrt{3}\right) N^2} \right\} \tag{6.12}$$

$$= \frac{\varepsilon}{\left(\sqrt{3}\right) a^2} \left\{ 12 + \frac{4}{N} + \frac{32}{N^2} \right\} = \frac{\Delta H_{subl}}{\sqrt{3} N_A a^2} \left\{ 1 + \frac{1}{3N} + \frac{8}{3N^2} \right\} \tag{6.13}$$

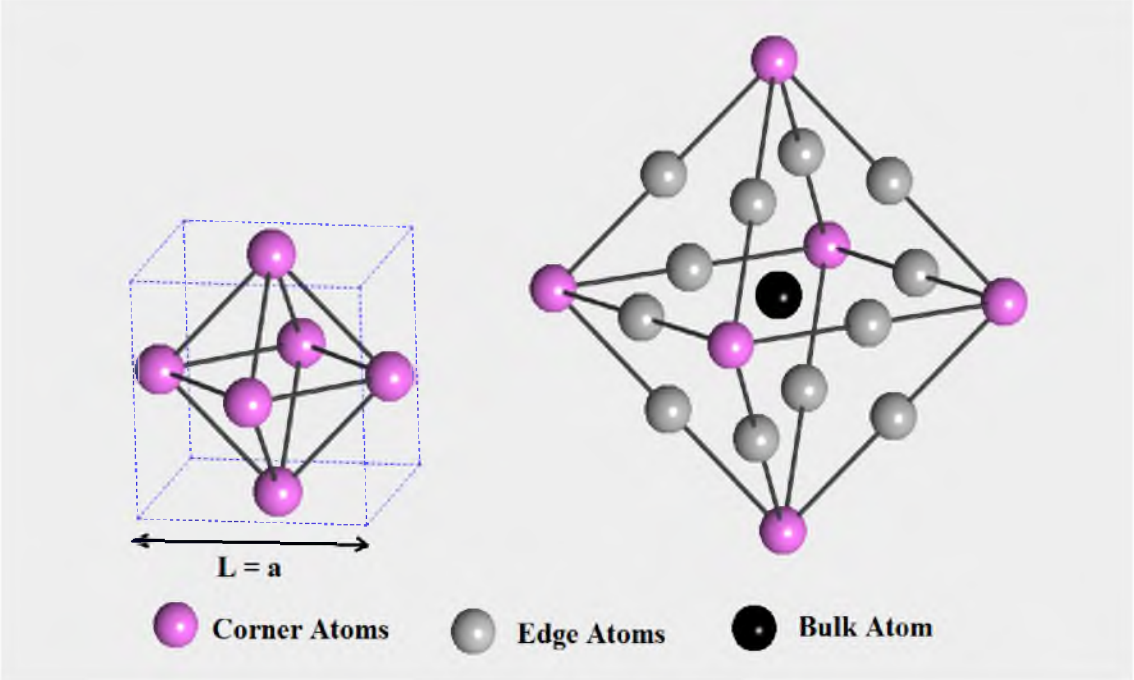

Figure 6.5: Octahedra of side lengths L = a, and L = 2a

For very large particles, $N \to \infty$, the specific surface energy is given by

$$\gamma = \frac{\Delta H_{subl}}{\sqrt{3} N_A a^2} = 0.5774 \frac{\Delta H_{subl}}{N_A a^2} \tag{6.14}$$

which is the same as for particles of a tetrahedral shape. This is to be expected since both particles are bounded by {111} faces, and for large particles, there is negligible contribution from edges and corners. For the smallest value of $N = 1$, the specific surface energy is given by

$$\gamma(N=1) = \frac{4\Delta H_{subl}}{\sqrt{3} N_A a^2} = 2.3094 \frac{\Delta H_{subl}}{N_A a^2} \tag{6.15}$$

Note that the specific surface energy of the smallest octahedron is 4 times that of a large octahedron. The smallest octahedron has 6 atoms, all of which are at the corners.

6.2.5 General Expression for a Truncated Octahedron-shaped Particle for $N = 3m$ (Where m Is a Positive Integer with the Smallest Value of 1)

We consider a particle in the shape of a truncated octahedron. Figure 6.6 shows truncated octahedra of length $L = 3a$ and $L = 6a$. In this case, there are four different types of surface atoms: atoms on square {100} surfaces with 4 unsatisfied bonds/atom, atoms on hexagonal {111} surfaces with 3 unsatisfied bonds/atom, edge atoms with 5 unsatisfied bonds/atom, and corner atoms with 7 unsatisfied bonds/atom. The volume of a truncated-octahedron of length L is $\frac{4L^3}{27}$.

Following the same procedure as before (Appendix), the specific surface energy is given by

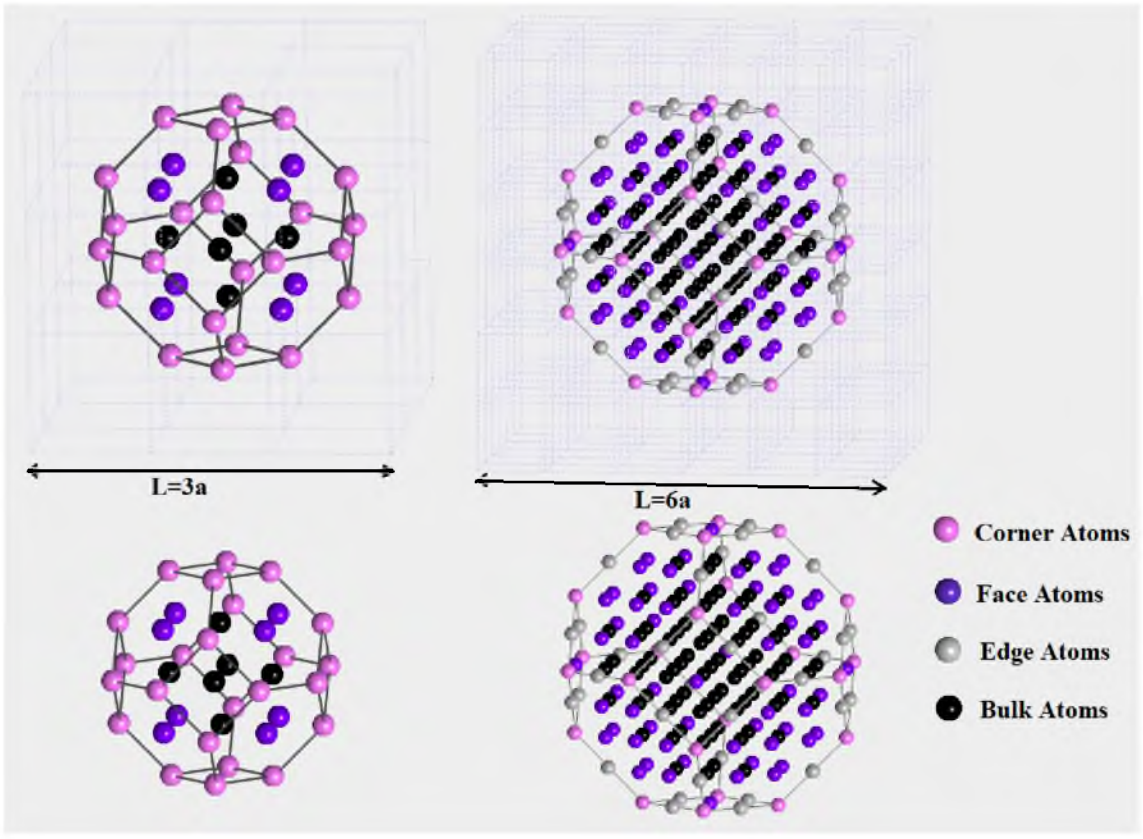

Figure 6.6: Truncated-octahedra of side lengths L = 3a and L = 6a

$$\gamma(N) = \frac{\varepsilon}{a^2}\left\{\frac{32N^2 + 60N + 36}{\left(1+2\sqrt{3}\right)N^2}\right\} \tag{6.16}$$

$$= \frac{4\varepsilon}{\left(1+2\sqrt{3}\right)a^2}\left\{8 + \frac{15}{N} + \frac{9}{N^2}\right\} = \frac{8\Delta H_{subl}}{3\left(1+2\sqrt{3}\right)N_A a^2}\left\{1 + \frac{15}{8N} + \frac{9}{8N^2}\right\} \tag{6.17}$$

For very large particles, $N \to \infty$, the specific surface energy is given by

$$\gamma = \frac{8\Delta H_{subl}}{3\left(1+2\sqrt{3}\right)N_A a^2} = 0.5974\frac{\Delta H_{subl}}{N_A a^2} \tag{6.18}$$

For the smallest complete truncated octahedron ($N = 3$), the specific surface energy is

$$\gamma(N=3) = \frac{14\Delta H_{subl}}{3\left(1+2\sqrt{3}\right)N_A a^2} = 1.0454\frac{\Delta H_{subl}}{N_A a^2} \tag{6.19}$$

The smallest truncated octahedron contains 38 atoms. Calculations were conducted for five different shapes in this work; cube, cubo-octahedron, tetrahedron, octahedron, and truncated octahedron. Many other shapes can be easily examined.

Table 6.1 shows the specific surface energies of particles of various shapes in the two size limits: the smallest cluster size for a complete given shape and infinitely large ($N \to \infty$) size. Figure 6.7 shows the calculated specific surface energies for particles of various shapes as a function of size (equivalent sphere diameter, d, given by Particle Volume $= \frac{4\pi}{3}\left(\frac{d}{2}\right)^3$). The points shown in the figure thus represent discrete points corresponding to particles of any given complete shape. In the bulk limit ($N \to \infty$), note that the most stable shapes are tetrahedron and octahedron, and the least

Table 6.1: Specific surface energies of f.c.c. metal particles of various shapes as a function of size: (a) The smallest possible cluster, (b) Very large crystals (asymptotic limit).

Shape of an f.c.c. cluster	γ(N) in terms of $\frac{\Delta H_{subl}}{N_A a^2}$ for the smallest possible cluster	γ(N) in terms of $\frac{\Delta H_{subl}}{N_A a^2}$ for large (bulk) clusters
Cube	1.33	0.667
Cubo-octahedron	1.04	0.634
Tetrahedron	1.73	0.577
Octahedron	2.31	0.577
Truncated Octahedron	1.05	0.597

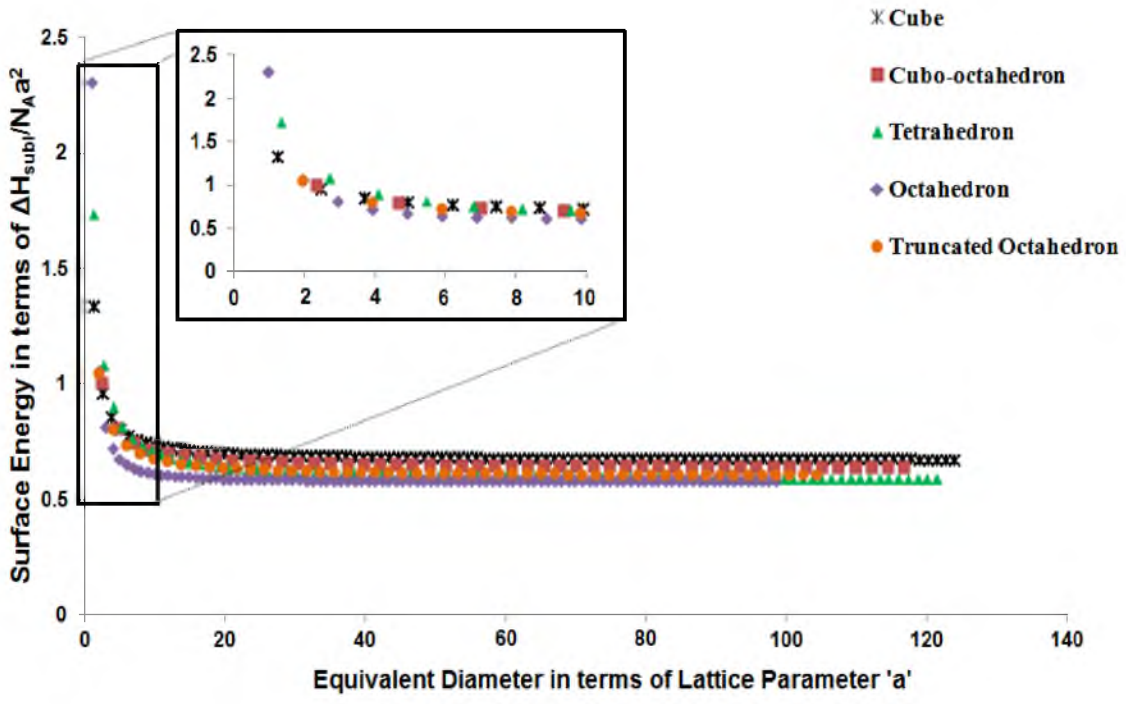

Figure 6.7: Specific surface energy as a function of equivalent diameter for a f.c.c. structure of different shapes: cube, cubo-octahedron, tetrahedron, octahedron, and truncated octahedron. The inset shows the variation of specific surface energy with equivalent diameter below ~10a, where a is the lattice parameter.

stable shape is a cube. The largest relative difference between the two specific energies is ~15.6%. The small difference in surface energies of various crystal shapes thus also suggests that growth conditions (kinetics) in most cases dictate the observed shape. Thus, it is not surprising that particles of various shapes are often observed and they cannot be predicted by energy minimization schemes. Also, calculations given here assume no additional materials are present (e.g., surrounding environment from which different species may selectively adsorb thus changing surface conditions). Figure 6.7 shows that beyond an equivalent diameter of ~$10a$, specific surface energy may be regarded as a constant, and the particle may be considered as a large (bulk) particle. The 'nano effect' insofar as specific surface energy is concerned exists for particles of diameter below 5 nm (assuming lattice parameter a ~0.5 nm). Beyond this, the nano effect is negligible but the effect of particle size on certain properties/functions continues: for example, the chemical potential.

6.3 Discussion

Figure 6.8 shows the calculated values of specific surface energies for particles of octahedral shape for various f.c.c. metals (Ag, Cu, Ni, Au, Pt, Ir, and Rh) as a function of particle size. The calculations were made using the reported experimental values of the enthalpies of sublimation, ΔH_{subl} [33, 34] and lattice parameters [35]. Table 6.2 lists the values of ΔH_{subl} and a used in the calculations [35]. Specific surface energies are difficult to measure. Thus, a comparison with experimental results is often not possible. However, the estimated values in the present work are in accord with other calculations (ab initio or empirical) reported in the literature [7, 8, 16, 28, 36]. The specific surface energies (octahedral shape) in the large particle limit of Ag, Cu, Ni, Au, Pt, Ir, and Rh are

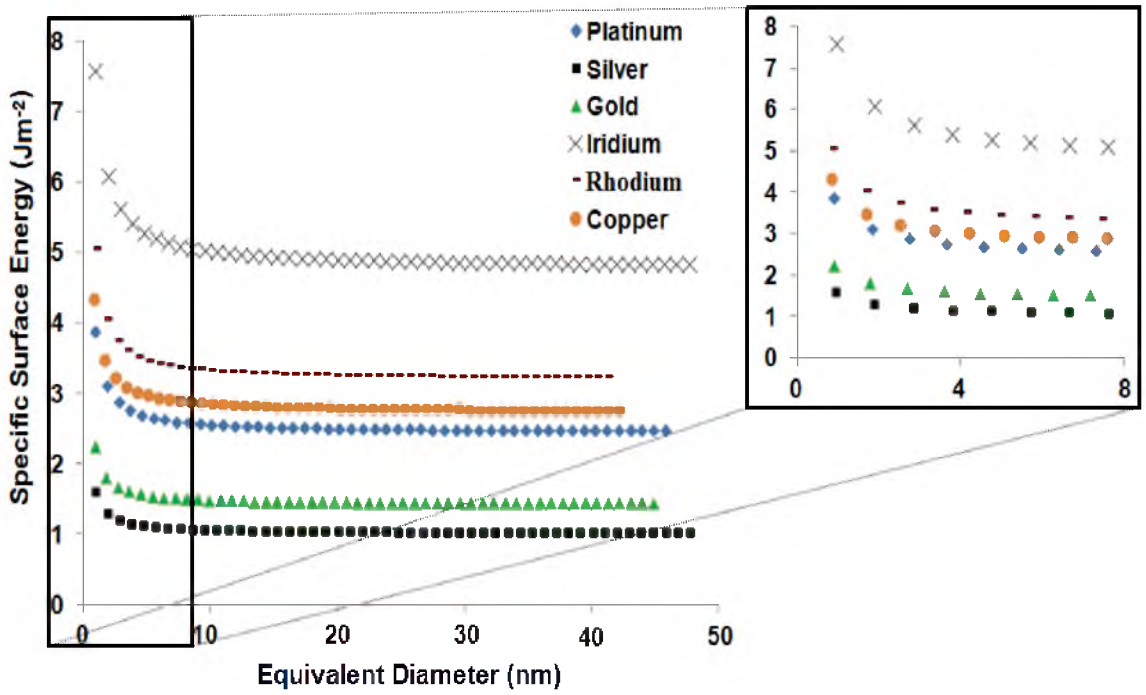

Figure 6.8: Specific surface energy of octahedral particles as a function of equivalent diameter for various f.c.c. metals. The inset shows the variation of surface energy with equivalent diameter below 8nm.

Table 6.2: Lattice parameters, heats of sublimation, and calculated (asymptotic) values of specific surface energies for (111) surfaces of various f.c.c. metals.

f.c.c. Metals	Lattice Parameter [35] in nm	Heat of Sublimation, ΔH_{subl} in kJmol^{-1}	Asymptotic values of specific surface energy in Jm^{-2}
Silver (Ag)	0.409	160.31[33]	0.919
Gold (Au)	0.408	224.7[33]	1.29
Copper (Cu)	0.361	338.9[34]	2.49
Iridium (Ir)	0.384	671.0[34]	4.36
Nickel (Ni)	0.352	377.5[34]	2.92
Platinum (Pt)	0.392	357.3[33]	2.23
Rhodium (Rh)	0.380	495.0[34]	3.29

determined to be, respectively,0.919 Jm^{-2}, 2.49 Jm^{-2}, 2.92 Jm^{-2}, 1.29 Jm^{-2}, 2.23 Jm^{-2}, 4.36 Jm^{-2}, and 3.29 Jm^{-2}. These are comparable to the values reported in the literature [7, 8, 16, 36]. For example, Eberhart et al. [7] used the broken-bond model to calculate the specific surface energies of b.c.c., f.c.c., and h.c.p structures.

The calculations given in the present work agree well with those in the work by Eberhart et al. [7]. For instance, the specific surface energy of f.c.c. Cu was determined by Eberhart et al. [7] to be 2.46 Jm^{-2} as compared to the specific surface energy of 2.49 Jm^{-2} presented in Figure 6.8. The slight difference is related to different values of ΔH_{subl} used in the two studies. Using the full charge density model, Vitos et al. [16] estimated specific surface energies for (111) planes for Ag (1.21 Jm^{-2}), Cu (1.94 Jm^{-2}), Ni (2.01 Jm^{-2}), Au (1.283 Jm^{-2}), Pt (2.299 Jm^{-2}), Ir (2.971 Jm^{-2}), and Rh (2.43 Jm^{-2}). The values estimated in the present work are generally comparable to those given by Vitos et al. [16]. It is to be noted, however, that for the estimation of accurate values of specific surface energies, reliable values of sublimation energies are required.

An indirect method to assess the validity of any theoretical model is to measure properties which directly depend on the values of the specific surface energies. One such property is the lattice parameter as a function of particle size. For very small particles, because of the pressure caused by the specific surface energy (Gibbs-Thompson effect), the lattice parameter is smaller than for large (bulk) particles. Thus, the measurement of the lattice parameter as a function of particle size affords an indirect method of model validation (assuming there is no redistribution of electrons). An approximate estimate of the effect of pressure on lattice parameter is given below. The calculation is approximate as it does not account for relaxation (redistribution).

For a spherical particle of a diameter d, the pressure within the particle is given by

$$p = \frac{4\gamma(d)}{d} \tag{6.20}$$

At small particle sizes, the specific surface energy itself is a function of particle size, where d is the equivalent diameter. Thus, $\gamma(d)$ is a function of particle size. The change in volume is given by

$$\frac{\Delta v}{v_{bulk}} = -\frac{p}{B} \tag{6.21}$$

where B is the bulk modulus. Now,

$$\frac{\Delta v}{v_{bulk}} \cong \frac{3\Delta a}{a_{bulk}} \tag{6.22}$$

Thus, the lattice contraction is given by

$$\frac{\Delta a}{a_{bulk}} = -\frac{p}{3B} = -\frac{4\gamma(d)}{3Bd} \tag{6.23}$$

Figure 6.9 shows the dependence of the calculated lattice parameter contraction of platinum on particle size for various crystal shapes: cube, cubo-octahedron, tetrahedron, octahedron, and truncated octahedron. The lattice parameter contraction was calculated from the experimental value of bulk modulus of platinum, which is ~278 GPa [37]. The x-axis in Figure 6.9 is the inverse equivalent diameter, d^{-1}, for any given shape. Note

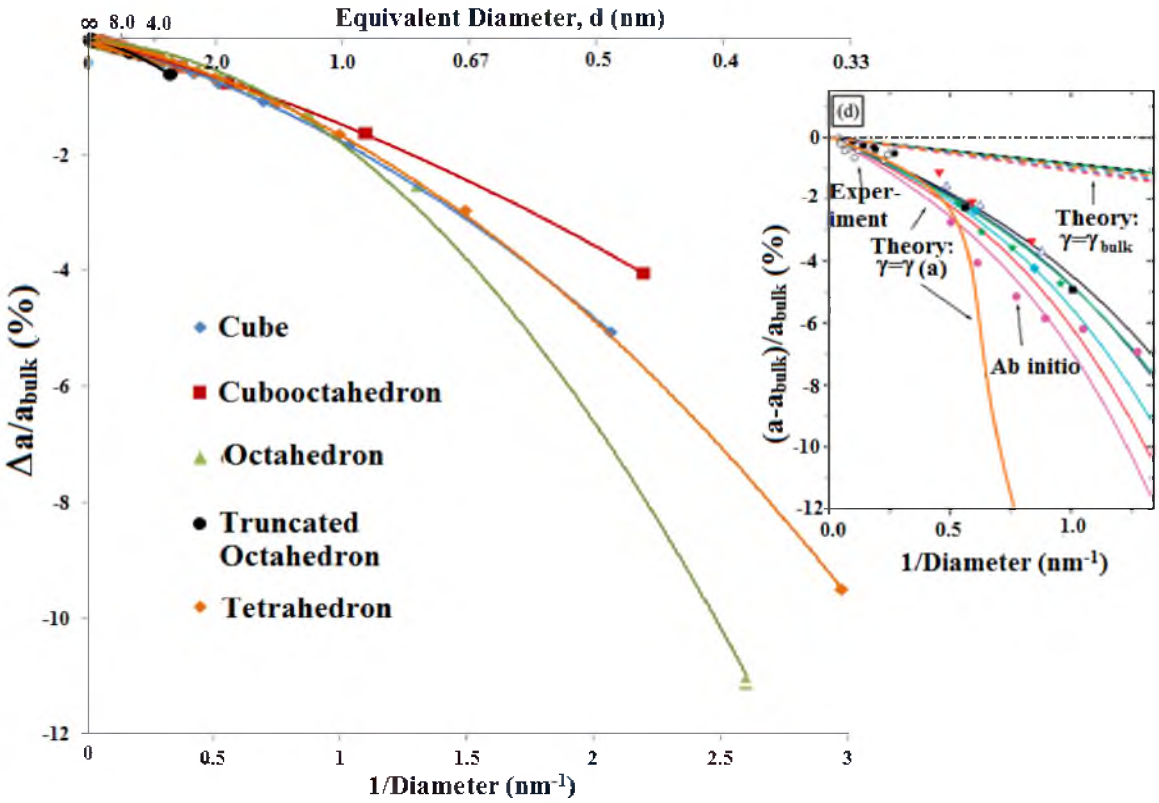

Figure 6.9: Lattice parameter contraction as a function of particle size for various crystal shapes for platinum (f.c.c.). Figure in the inset shows the lattice parameter contraction as a function of particle size studied by Chepulskii [28]. In their study, the dependence of lattice contraction on particle size is greater than the dependence showed by broken-bond model.

that the lattice parameter for a given equivalent diameter is a function of particle shape since the specific surface energy is a function of the particle shape. For very small particles of an octahedral shape of diameter about 0.5 nm, the lattice parameter contraction was calculated to be about 6%. For a particle of 1 nm in diameter, the estimated lattice contraction is ~1.8%.

The estimated lattice contraction for a 1 nm diameter particle in the work by Chepulskii and Curtarolo [28] ranged between ~4% and ~6%, depending upon the particle shape. Solliard et al. [38] experimentally determined lattice parameter contractions for platinum and gold at 300K using (220) and (422) reflections. For a

platinum particle of diameter ~4 nm, the lattice parameter measured by Solliard et al. [38] was 3.902 nm, whereas the calculated lattice parameter based on the present work is 3.909 nm. Within the experimental errors and the assumptions made in the model, this agreement is quite reasonable. However, in order to validate this model, or others in the literature, it would be necessary to obtain experimental measurements on much smaller particles, on the order of ~0.5 nm in diameter.

Figure 6.9 shows that the lattice contraction exhibits a convex up curvature when plotted as an inverse function of the particle diameter. This is due to increasing specific surface energy with decreasing size. In the work by Chepulskii and Curtarolo [28] also, the estimated lattice contraction exhibits a convex up curvature, suggesting that in their work too, specific surface energy increased with decreasing particle size in the sub-nano to nanosize range.

Chepulskii and Curtarolo [28] also examined the shape stability of nanosize Pt particles. In the small cluster size range (below 300-400 atoms in the cluster), Chepulskii and Curtarolo [28] used ab initio calculations. For larger sizes, due to the large computational time required, Chepulskii and Curtarolo [28] used a variational approach, which was extended down to the very small size range as well. Many interesting results from their study will be compared with the present results. Chepulskii and Curtarolo [28] observed that shape stability depends on the size of the particles. For relatively large clusters (139 atoms or more), truncated octahedron was determined to be the most stable shape, with cube-shaped particles being the least stable. In the present work also, cube-shaped particles were found to be the least stable. In the work by Chepulskii and Curtarolo [28], an octahedron was determined to be almost as stable as a truncated octahedron. At larger sizes, a truncated octahedron became more stable. Chepulskii and

Curtarolo [28] in their ab initio calculations determined that for very small clusters less than ~1 nm, a tetrahedron is more stable than an octahedron. When the particle diameter lies between 1 nm and 2 nm, the trend calculated in the present work generally follows the same trend as discussed by Chepulskii and Curtarolo [28].

In the work by Chepulskii and Curtarolo [28], the most stable shape at the smallest size (below ~100 atoms) was determined to be a tetrahexahedron with {730} facets. Chepulskii and Curtarolo [28] were unable to make ab initio calculations on crystals of a tetrahexahedral shape as the number of atoms was too large, making computational time too long. Their ab initio calculations were limited to clusters containing about 300 to 400 atoms. However, extrapolations of the variational calculations were made down to tetrahexahedral clusters containing as few as 15 atoms. On the basis of these extrapolations, Chepulskii and Curtarolo [28] determined that for clusters containing fewer than 139 atoms, tetrahexahedron is the most stable shape. The extrapolations made down to 15 atoms also indicated that the most stable shape is a tetrahexahedron. It is to be noted, however, that since even the smallest tetrahexahedron contains far more than 15 atoms, extrapolations made in their study down to such a small size are not physically realizable. Yu-Hua et al. [39] have examined specific surface energies of crystals of tetrahexahedral shapes formed by various crystal facets ({210}, {310}, {410}, {520}, and {730}) as a function of particle size using molecular static computational methods. It was observed that the specific surface energy decreases with increasing size and eventually reaches asymptotic limits. These authors investigated stability of various tetrahexhedral shapes, but did not compare them with any other crystal shapes. However, Yu-Hua et al. [39] found that within the tetrahexhedral shapes they examined, {730} planes exhibited higher specific surface energy than {310}, {410},

and {510} planes, demonstrating that even within the tetrahexahedral shapes, a tetrahexahedron with {730} is not the most stable shape.

We have not examined the tetrahexahedral shape. Of the shapes examined in the present work, an octahedron was determined to be the most stable shape over the entire size range – from the smallest to very large (bulk) sizes. At the large size range, a tetrahedron was also found to be as stable as an octahedron. This is not surprising since both shapes are bounded by {111} planes. However, at the small size range, an octahedron was found to be more stable than a tetrahedron. This is consistent with expectations since both corner and edge atoms of a tetrahedron have more unsatisfied bonds (6 and 9) compared to an octahedron (5 and 8). When particles are small, edge and corner atoms make larger contribution to the specific surface energy than face atoms. In the work by Chepulskii and Curtarolo [28], however, calculations made using the variational approach did not account for edge and corner atoms. As stated earlier, in the very small size range, based on ab initio calculations, Chepulskii and Curtarolo [28] found a tetrahedron to be more stable than an octahedron. Our results do not agree with this result of Chepulskii and Curtarolo [28].

According to the present calculations, an octahedron and a tetrahedron are more stable than any of the other shapes. In most experimental studies, however, various shapes are observed, including near spherical. There are several reasons for this. First, the present calculations (and most other calculations reported in the literature) assume that particles are surrounded by vacuum. In almost all experiments, many other species are typically present (in solution or in gas phase from which the particles are formed). Second, the calculations presented here are equilibrium calculations (and also in the reported studies). In most experimental work, however, kinetic factors determine the

observed shapes. Thus, equilibrium calculations (energy minimization) cannot be compared with experimentally observed shapes, as in most experimental studies, growth conditions determine shape. For example, any given shape observed in a low temperature synthesis process is 'frozen in', as solid state diffusion is much too slow, which prevents particles from achieving their true equilibrium shapes in a reasonable period of time.

One possible method of determining if indeed even large single crystal particles exhibit tetrahedral or octahedral as the most stable shapes would be to thermally treat isolated particles in vacuum (or in an inert atmosphere such as Ar) in a suspended state (without contact with furnace walls). At high temperatures in an inert atmosphere, surfaces would likely be clean (without any adsorbed species). Also, at high temperatures, single crystal particles will tend to achieve thermodynamically stable equilibrium shapes regardless of the starting shapes, as long as particles are sufficiently far apart so that there is little interparticle flux of atoms, which can cause Ostwald ripening. The approximate time necessary for a particle to achieve the most stable shape will be on the order of $t \sim \frac{d^2}{4D_s}$ where D_s is the self diffusion coefficient. The self diffusion coefficient of silver at 900°C is ~10^{-9} cm^2s^{-1}[40]. For a single crystal particle of silver of diameter of 0.2 micron (200 nm) at 900°C, the estimated time will be ~0.1 s and thus should be easily achievable (for example in a free fall through a furnace of sufficient height). In principle, experimental procedures can be devised to test this on various f.c.c. metals, such as Ag, Au, Cu, Pt, etc. In all of these metals near the melting temperature, the self diffusion coefficient in the solid state is ~10^{-9} cm^2s^{-1}[40-42]. The prediction therefore is that at a sufficiently high temperature, single crystal particles on the order of 200 nm (which are rather large particles, Figure 6.8) will achieve equilibrium shapes

(octahedron or tetrahedron) in a reasonable time. Within the approximations of the broken-bond model, the equilibrium shape of particles should be independent of temperature, since the relative values of specific surface energies of various crystal facets determined using bond energies are weakly dependent of temperature. Also, all f.c.c. metals would be expected to exhibit similar shapes. In the computational work by Vitos et al. [16], it was determined that relative values of specific surface energies of different crystal facets (anisotropic ratios) were different for different metals, depending upon their electronic structures. If this is the case, one would expect different shapes for crystals of different metals after high temperature thermal treatments of the type described here. Equilibrium calculations such as those given here and in many other studies need to be compared with such experimental results. To the authors' knowledge, no such data are available.

Figure 6.10 shows a plot of the specific surface energy for particles of an octahedral shape as a function of size. In addition to full octahedra, calculations were also made for the intermediate range corresponding to $N = 2$ and $N = 3$. Over this range, calculations of specific surface energy were made by incrementally adding atoms on an octahedron with $N = 2$. Initially, atoms were added on $\{111\}$ surfaces and later on edges and corners, until ultimately, a full octahedron was again formed corresponding to $N = 3$. In the intermediate range, surfaces contain atoms with more unsatisfied bonds as compared to a complete octahedron.

Once these atoms are coordinated with other atoms while forming the next octahedral configuration, the specific surface energy decreases and reaches the value corresponding to the next larger complete octahedron. Thus, the specific surface energy initially increases as the size (equivalent diameter) increases and then decreases as the

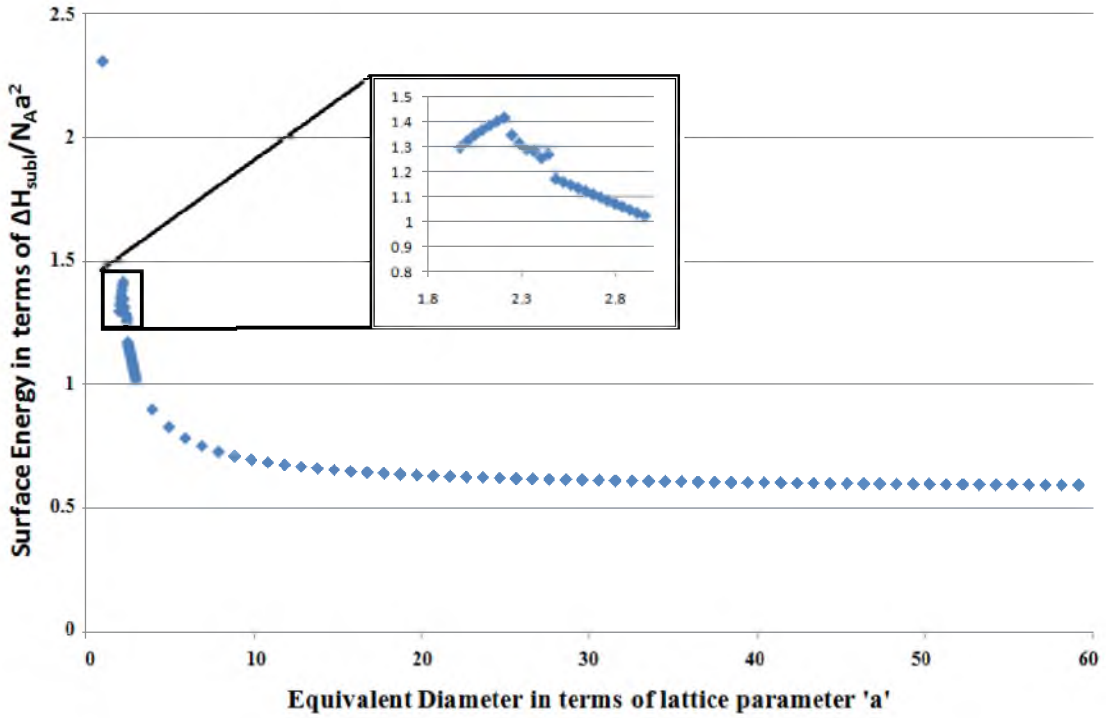

Figure 6.10: Specific surface energy as a function of equivalent diameter for clusters of an octahedral shape. The inset shows the variation of specific surface energy as a function of size when the number of atoms varies between one complete octahedron (N = 2) and the next complete octahedron (N = 3). The specific surface energy increases to a point and then decreases until it reaches that corresponding to the next complete octahedral structure.

shape approaches a full octahedron corresponding to $N = 3$.

It is thus expected that whenever clusters are formed that do not correspond to any complete shape, the specific surface energy will be higher due to the presence of more unsatisfied bonds. This would also suggest that catalytic activity will likely be higher for particles that do not form any complete shape. This of course is well known as catalytic activity is generally higher at atomic steps and ledges.

6.4. Summary

In the present work, the simple broken bond model was used to investigate the specific surface energy of f.c.c. metals as a function of shape and size. For all shapes

investigated, the specific surface energy decreased with increasing particle size. Higher specific surface energy of small particles is due to a greater proportion of atoms at edges and corners, which exhibit a greater number of unsatisfied bonds. Beyond an equivalent diameter of ~5 nm, the specific surface energy was nearly constant for each shape investigated. Thus, specific surface energy may be considered independent of size beyond ~5 nm. Beyond this critical size, octahedral and tetrahedral shapes were the most stable, truncated octahedron was the second most stable, cubo-octahedron was the third most stable, and cube was the least stable. Relative stability of a given shape is thus directly related to the relative areas of {111} faces and {100} faces; the higher the percent of {111} surfaces, the greater is the stability. At the smallest size, octahedron was found to be more stable than tetrahedron. This is attributed to a greater number of unsatisfied bonds on the corners and the edges of a tetrahedron compared to an octahedron.

6.5 Acknowledgements

This work was supported by the National Science Foundation under the Grant Number CBET-0931080.

6.6 References

1. G.A. Somorjai, *Introduction to Surface Chemistry and Catalysis*, John Wiley & Sons., New York (1994).

2. L.E. Murr, *Interfacial Phenomena in Metals and Alloys*, Addison – Wesley Publishing Co., Pennsylvania (1975).

3. I.S. Grigoriev, E.Z. Meilikhov, *Handbook of Physical Quantities*, CRC Press, Florida (1997).

4. J.M. Blakely, *Introduction to the Properties of Crystal Surfaces*, Pergamon, (1973).

5. R.G. Linford, *Chem.Soc.Rev.*, **1,** 445 (1972).

6. H. Mykura, *Solid Surfaces and Interfaces*, Dover, New York (1966).

7. J.G. Eberhart, S. Horner, *J. Chem. Ed.* **87**, 608 (2010).

8. W. R. Tyson, W. A. Miller, *Surf. Sci.*, **62**, 267 (1977).

9. M. Methfessel, C. O. Rodriguez, O. K. Andersen, Phys. Rev. B 1989, 40, 2009-2012.

10. H.L. Skriver, N.M. Rosengaard, *Phys. Rev. B,* **46**, 7157 (1992).

11. J. Koll´ar, J. Vitos, H.L. Skriver, *Phys. Rev. B*, **49**, 11288 (1994).

12. M.J. Mehl, D.A. Papaconstantopoulos, *Phys. Rev. B*, 54, 4519 (1996).

13. A.M. Rodr´ıguez, G. Bozzolo, J. Ferrante, *Surf. Sci.*, **289**, 100 (1993).

14. H.L. Skriver, N.M. Rosengaard, *Phys. Rev. B*, **43**, 9538 (1991).

15. M. Alden, H.L. Skriver, S. Mirbt, B. Johansson, *Phys. Rev. Lett.*, **69**, 2296 (1992).

16. L. Vitos, A.V. Ruban, H.L. Skriver, J. Koll´ar, *Surf. Sci.*, **411**, 186 (1998).

17. L. Vitos, J. Koll´ar, H.L. Skriver, *Phys. Rev. B*, **55**, 13521 (1997).

18. O.K. Andersen, O. Jepsen, *Phys. Rev. Lett.*, **53**, 2571 (1984).

19. W.R.L. Lambrecht, O.K. Andersen, *Phys. Rev. B.,* **34**, 2439 (1986).

20. J.P. Perdew, K. Burke, M. Ernzerhof, *Phys. Rev. Lett.*, **77**, 3865 (1996).

21. L. Vitos, J. Koll´ar, H.L. Skriver, *Phys. Rev. B.,* **49**, 16694 (1994).

22. J.A. Moriarty, R. Phillips, *Phys. Rev. Lett.*, **66**, 3036 (1991).

23. L. Vitos, H.L. Skriver, J. Koll´ar, *Surf. Sci.*, **425**, 212 (1999).

24. I. Galanakis, N. Papanikolaou, P.H. Dederichs, *Surf. Sci.*, **511**, 1 (2002).

25. M.C. Desjonqu`eres, D. Spanjaard, *Concepts in Surface Physics, Springer Series in Surface*, Springer Berlin (1993).

26. I. Galanakis, G. Bihlmayer, V. Bellini, N. Papanikolaou, R. Zeller, S. Blugel, P.H. Dederichs, *Europhys.Lett.*, **58**, 751 (2002).

27. V.M. Samsonov, N.Y. Sdobnyakov, A.N. Bazulev, *Colloids and Surfaces A: Physicochem. Eng. Aspects*, **239**, 113 (2004).

28. R.V. Chepulskii, S. Curtarolo, *ACS Nano*, **5**, 247 (2011).

29. R. C. Tolman, *J. Chem. Phys.*, **17**, 333 (1949).

30. H. M. Lu, Q. Jiang, *J. Phys. Chem. B*, **108**, 5617 (2004).

31. K. Koga, X. C. Zeng, A. K. Shchekin, *J. Chem. Phys.*, **109**, 4063 (1998).

32. M. Methfessel, D. Hennig, M. Scheffler, *Phys. Rev. B*, **46**, 4816 (1992).

33. J. A. Kerr, *CRC Handbook of Chemistry and Physics 1999-2000: A Ready-Reference Book of Chemical and Physical Data (CRC Handbook of Chemistry and Physics),* 81st ed. CRC Press, Florida (2000).

34. A. M. James, M. P. Lord, *Macmillan's Chemical and Physical Data,* Macmillan: London (1992).

35. D. Lange, *Lange's Handbook of Chemistry,* 8th ed.; Handbook Publishers Inc.: 1952.

36. A.R. Miedema, *Philips tech. Rev.*, **38**, 257 (1978).

37. N. C. Holmes, J. A. Moriarty, G. R. Gathers, W. J. Nellis, *J. App. Phys.*, **66**, 2962 (1989).

38. C. Solliard, M. Flueli, *Surf Sci.*, **156**, 487 (1985).

39. C. T. Tomizuka, E. Sonder, *Phys. Rev.*, **103**, 1182 (1956).

40. B. Okkerse, *Phys. Rev.*, **103**, 1246 (1956).

41. A. Kuper, H. Letaw, Jr., L. Slifkin, E. Sonder, C. T. Tomizuka, *Phys. Rev.*, **96**, 1224 (1954).

CHAPTER 7

CONCLUSIONS

The focus of this thesis was on the study of coupled transport and its effect on different electrochemical systems and the implications in sodium metal chloride batteries and Proton Exchange Membrane Fuel Cells.

7.1 Sodium β"-Alumina Solid Electrolyte

A sodium zinc chloride battery was designed using sodium β"-alumina (BASE) as the solid electrolyte and sodium and $ZnCl_2$ as the electrode materials. Several electrochemical tubular and planar cells of configuration, Na/BASE/$ZnCl_2$, were constructed and tested. During charge-discharge and cycling experiments, there was no evidence of zinc ion exchange found in BASE. This implies that zinc chloride is a viable cathode. Several freeze-thaw cycles were conducted on the planar cell with a stable performance output. A three-cell stack was designed, constructed, and electrochemically tested. During the electrochemical testing, one of the cells became inoperable due to the misalignment of the electrolyte. As the electrode materials are highly conductive due to the presence of metallic Zn in cathode, the cell got short circuited with low resistance. The whole stack was tested as a two-cell stack. The stack gave a stable charging voltage of ~ 4.0 V. A five-cell stack was designed and constructed.

The kinetics of conversion of α-alumina+YSZ to Na β"-alumina+YSZ was studied. A patented vapor phase method was used to fabricate Na β"- alumina samples.

In order to expedite the diffusion of Na_2O through the samples, an oxygen ion conductor was incorporated in the starting α-alumina samples. This provided a rapid parallel path for the transport of O^{2-} ions as β"-alumina is a poor conductor of oxygen ions. A theoretical model was proposed and a general kinetic equation for conversion was formulated with diffusion and interfacial parameters. Several samples of various grain sizes from 0.53 μm to 4.15 μm were fabricated. These samples were converted to β"-alumina at several temperatures and for various times ranging from 1250°C to 1450°C and 1 hour to 15 hours. The effective diffusion and interfacial rate constants were determined from the experimental data and the proposed theoretical model. It showed that when the thickness converted is small, the kinetics is linear (interface controlled) and when the thickness converted is large, the kinetics is parabolic (diffusion controlled). The results also indicated that the smaller the grain size, the faster the rate of conversion. Arrhenius plots of interfacial and diffusion reactions showed that interfacial reactions at the three-phase boundaries and reaction front depended more on grain size than the actual diffusion of Na_2O through the sample (Na^+ through β"-alumina and O^{2-} through YSZ).

7.2 Coarsening of Copper Particles in Aqueous Media

Experiments on the growth of copper particles in aqueous media containing various concentrations of copper ions (by dissolving copper nitrate) were conducted. The samples were placed in test tubes in stagnant conditions. Experiments were conducted at room temperature and at 80°C. In order to obtain as low a concentration of copper ions as possible, experiments were also conducted in DI water with hydrogen bubbling. For determining the kinetics of particle growth, experiments were conducted for different time periods, varying between 12 h and 144 h at room temperature in DI water, in DI

water with hydrogen bubbling, and in 0.01 M $Cu(NO3)_2$ solution. Negligible growth occurred in samples treated at room temperature with hydrogen bubbling, which was attributed to very low copper ion concentration. It was also observed that the kinetics was faster at higher temperature. Since electron concentration in an aqueous medium is negligible, it is expected that no growth would have occurred in isolated particles. However, as particles were placed in test tubes, the vast majority of particles were not isolated (were in contact with the neighboring particles). The growth of particles occurred by a coupled transport – that of copper ions through the liquid and that of electrons through direct contact. Solid state transport is all but ruled out given the very low diffusion coefficient of copper in the solid state at such a low temperature. Indeed, a comparison of the present results with Ostwald ripening in metallic alloys shows orders of magnitude difference in kinetics. Since the diffusion coefficient of ions through aqueous media is typically 10^{-6} to 10^{-5} cm^2s^{-1}, which is several orders of magnitude higher than that in the solid-state, the kinetics of electrochemical Ostwald ripening/agglomeration is expected to be much faster compared to solid state Ostwald ripening, as observed in the present work.

The kinetics of particle growth exhibited linear dependence. For physically separated particles in most studies, kinetics of growth is typically cubic (diffusion-controlled) or parabolic (interface-controlled). The observation that the kinetics is linear is attributed to interface-controlled growth with the additional feature of increased driving force due to decreased transport (diffusion) distance as the center-to-center distance between particles decreases with the occurrence of growth. Since negligible solid state transport is expected, the difference between Ostwald ripening of physically separate particles (yet sitting on an electronically conducting support) and those in direct

contact with each other (often referred to as agglomeration) is only the relative difference in diffusion distances. Agglomeration in such a case may be referred to as electrochemical agglomeration. Since the diffusion distance is shorter in electrochemical agglomeration, its kinetics is expected to be much faster than Ostwald ripening of physically separate (yet sitting on an electronically conducting support) particles. This has important implications to catalyst growth in PEMFC. The present work suggests that catalyst growth of particles in direct physical contact (agglomerated) may be much faster than physically separate (yet sitting on carbon) particles. Thus, special care should be taken to avoid agglomeration in PEMFC electrodes, especially the cathode.

7.3 Electrochemical Coarsening due to Applied Stress

The effect of applied stress on the chemical potential of Pt was measured using an electrochemical cell. Two platinum wires/foils were immersed in a $PtCl_4$+DMSO solution. One of the wires/foils was subjected to a tensile stress while the other one was left load-free. It was observed that the wire/foil subjected to a tensile stress developed a positive electric potential compared to the unstressed one, indicating that the application of a tensile stress decreases the chemical potential of platinum. The measured voltage coefficient per unit stress increased with increasing wire diameter. For wires of the smallest diameter used, the voltage coefficient per unit stress corresponded to the state of plane stress. The voltage developed per unit stress increased with increasing wire diameter. Increasing voltage coefficient per unit stress with increasing diameter is in accord with the predictions of linear elasticity that a transition from plane stress to plane strain should occur when using rods of a sufficiently large diameter. When the wires/foils were connected externally, the diameter/thickness of the one under tensile stress grew

while the diameter/thickness of the unstressed one shrank.

7.3.1 Core Shell Catalysts

The results obtained from the study of stress effect on the chemical potential of materials suggest an approach for the development of stable cathode catalysts for PEMFC. This work shows that core-shell catalysts consisting of a core and Pt shell having the same crystal structures, the Pt shell having a smaller lattice parameter than the core, and the Pt shell epitaxially matched to the core will result in a tensile stress (or reduced compression) in the Pt shell. Such core-shell catalysts should be inherently more stable as the tensile stress in the Pt shell will lower its chemical potential and decrease its tendency for dissolution. The predictions of the stability of Ag@Pt core-shell catalysts based on the effect of tensile stress in the shell in the present work are consistent with DFT calculations reported in the literature. Both the DFT calculations and the present thermodynamic analysis predict a stability of Ag@Pt against dissolution by about ~190 mV. These results thus also show the usefulness of continuum thermodynamic modeling in the design of nanoscale materials.

7.4 Surface Energy and Shape Stability of Metals

A simple broken-bond model was used to investigate the specific surface energy of f.c.c. metals as a function of shape and size. For all shapes investigated, the specific surface energy decreased with increasing particle size. Higher specific surface energy of small particles is due to a greater proportion of atoms at edges and corners, which exhibit a greater number of unsatisfied bonds. Beyond an equivalent diameter of ~5 nm, the specific surface energy was nearly constant for each shape investigated. Thus, specific surface energy may be considered independent of size beyond ~5 nm. Beyond this critical

size, octahedral and tetrahedral shapes were the most stable, truncated octahedron was the second most stable, cubo-octahedron was the third most stable, and cube was the least stable. Relative stability of a given shape is thus directly related to the relative areas of {111} faces and {100} faces; the higher the percent of {111} surfaces, the greater is the stability. At the smallest size, octahedron was found to be more stable than tetrahedron. This is attributed to a greater number of unsatisfied bonds on the corners and the edges of a tetrahedron compared to an octahedron.

APPENDIX

A.1 General Expression for Specific Surface Energy of a Cube-shaped Particle Valid for $N \geq 1$

Energy of unsatisfied bonds

$$= 6\left(2N^2 - 2N + 1\right) \times 4\varepsilon + 12\left(N - 1\right) \times 7\varepsilon + 8 \times 9\varepsilon \tag{A.1}$$

$$\begin{aligned} &= \left\{48N^2 - 48N + 24 + 84N - 84 + 72\right\}\varepsilon \\ &= \left\{48N^2 + 36N + 12\right\}\varepsilon \\ &= 12\left\{4N^2 + 3N + 1\right\}\varepsilon = \left\{4N^2 + 3N + 1\right\}\frac{\Delta H_{subl}}{N_A} \end{aligned} \tag{A.2}$$

Surface area of each face = $L^2 = N^2 a^2$ (A.3)

$$\therefore \gamma(N) = \frac{\left\{4N^2 + 3N + 1\right\}}{6N^2 a^2}\frac{\Delta H_{subl}}{N_A} = \frac{2\Delta H_{subl}}{3N_A a^2}\left\{1 + \frac{3}{4N} + \frac{1}{4N^2}\right\} \tag{A.4}$$

$$\text{As} \quad N \to \infty, \gamma(N) \to \frac{2\Delta H_{subl}}{3N_A a^2} = 0.667\frac{\Delta H_{subl}}{N_A a^2} \tag{A.5}$$

A.2 General Expression for Specific Surface Energy of a Cubo-octahedron Shaped Particle Valid for $N/2 \geq 1$

In order to form a complete cubo-octahedron, N must be an even, positive integer. Let us write $n = N/2$

$\therefore$ Number of atoms on the triangular $\{111\}$ faces of a cubo-octahedron = $(2n-1)(n-1)$

Number of atoms on the square {100} faces of a cubo-octahedron = $4n^2 - 4n + 1$

Number of atoms per edge = $(2n-1)$

Number of atoms at the corners = 12

For a cubo-octahedron, there are 6 square {100} faces, 8 triangular {111} faces, 24 edges, and 12 corners.

Energy of unsatisfied bonds

$$
\begin{aligned}
&= 6(4n^2 - 4n + 1) \times 4\varepsilon + 8(n-1)(2n-1) \times 3\varepsilon + 24(2n-1) \times 5\varepsilon + 12 \times 7\varepsilon \\
&= \left\{96n^2 - 96n + 24 + 48n^2 - 72n + 24 + 240n - 120 + 84\right\}\varepsilon \\
&= \left\{144n^2 + 72n + 12\right\}\varepsilon \\
&= \left\{144 \times \frac{N^2}{4} + 72 \times \frac{N}{2} + 12\right\}\varepsilon \\
&= \left\{36N^2 + 36N + 12\right\}\varepsilon \\
&= 12\varepsilon\left\{3N^2 + 3N + 1\right\}
\end{aligned}
\tag{A.6}
$$

Surface area of each square =

$$\left(\frac{Na}{\sqrt{2}}\right)^2 = \frac{N^2a^2}{2} \tag{A.7}$$

Surface area of each triangle =

$$\frac{\sqrt{3}}{4}\left(\frac{Na}{\sqrt{2}}\right)^2 = \frac{\sqrt{3}}{8}N^2a^2 \tag{A.8}$$

Total surface area

$$
\begin{aligned}
&= 6 \times \frac{N^2a^2}{2} + 8 \times \frac{\sqrt{3}}{8}N^2a^2 \\
&= 3N^2a^2 + \sqrt{3}N^2a^2 \\
&= (3 + \sqrt{3})N^2a^2
\end{aligned}
\tag{A.9}
$$

Specific surface energy

$$\gamma(N) = \frac{12\varepsilon}{a^2}\left\{\frac{3N^2+3N+1}{\left(3+\sqrt{3}\right)N^2}\right\} \tag{A.10}$$

$$= \frac{12\varepsilon}{\left(3+\sqrt{3}\right)a^2}\left\{3+\frac{3}{N}+\frac{1}{N^2}\right\} = \frac{3\Delta H_{subl}}{\left(3+\sqrt{3}\right)N_A a^2}\left\{1+\frac{1}{N}+\frac{1}{3N^2}\right\} \tag{A.11}$$

As $N \to \infty, \gamma(N) \to \dfrac{3\Delta H_{subl}}{\left(3+\sqrt{3}\right)N_A a^2} = 0.634\dfrac{\Delta H_{subl}}{N_A a^2}$ (A.12)

A.3 General Expression for Specific Surface Energy of a Tetrahedron-shaped Particle Valid for $N \geq 1$

Number of atoms on the triangular {111} faces of a tetrahedron = $(2N-1)(N-1)$

Number of atoms per edge = $(2N-1)$

Number of atoms at the corners = 4

For a tetrahedron, there are 4 triangular {111} faces, 6 edges, and 4 corners.

Energy of unsatisfied bonds

$$\begin{aligned} &= 4(2N^2-3N+1)\times 3\varepsilon + 6(2N-1)\times 6\varepsilon + 4\times 9\varepsilon \\ &= \left\{24N^2-36N+12+72N-36+36\right\}\varepsilon \\ &= \left\{24N^2+36N+12\right\}\varepsilon \\ &= 12\left\{2N^2+3N+1\right\}\varepsilon \end{aligned} \tag{A.13}$$

Total surface area = $2\sqrt{3}N^2a^2$ (A.14)

Specific surface energy

$$\gamma(N) = \frac{\varepsilon}{a^2}\left\{\frac{24N^2+36N+12}{2\left(\sqrt{3}\right)N^2}\right\} \tag{A.15}$$

$$= \frac{6\varepsilon}{\left(\sqrt{3}\right)a^2}\left\{2+\frac{3}{N}+\frac{1}{N^2}\right\} = \frac{\Delta H_{subl}}{\sqrt{3}N_A a^2}\left\{1+\frac{3}{2N}+\frac{1}{2N^2}\right\} \quad \text{(A.16)}$$

As

$$N \to \infty, \gamma(N) \to \frac{\Delta H_{subl}}{\sqrt{3}N_A a^2} = 0.5774\frac{\Delta H_{subl}}{N_A a^2} \quad \text{(A.17)}$$

A.4 General Expression for Specific Surface Energy of an Octahedron-shaped Particle Valid for $N \geq 1$

Number of atoms on the triangular {111} faces of an octahedron = $\frac{1}{2}(N-2)(N-1)$

Number of atoms per edge = $(N-1)$

Number of atoms at the corners = 6

For an octahedron, there are 8 triangular {111} faces, 12 edges, and 6 corners.

Energy of unsatisfied bonds

$$\begin{aligned} &= 4(N^2-3N+2)\times 3\varepsilon + 12(N-1)\times 5\varepsilon + 6\times 8\varepsilon \\ &= \left\{12N^2-36N+24+60N-60+48\right\}\varepsilon \\ &= \left\{12N^2+24N+12\right\}\varepsilon \end{aligned} \quad \text{(A.18)}$$

Total surface area = $\sqrt{3}N^2a^2$ (A.19)

Specific surface energy is given by

$$\gamma(N) = \frac{\varepsilon}{a^2}\left\{\frac{12N^2+24N+12}{\left(\sqrt{3}\right)N^2}\right\} \quad \text{(A.20)}$$

$$= \frac{12\varepsilon}{\left(\sqrt{3}\right)a^2}\left\{1+\frac{2}{N}+\frac{1}{N^2}\right\} = \frac{\Delta H_{subl}}{\sqrt{3}N_A a^2}\left\{1+\frac{2}{N}+\frac{1}{N^2}\right\} \quad \text{(A.21)}$$

As

$$N \to \infty, \gamma(N) \to \frac{\Delta H_{subl}}{\sqrt{3} N_A a^2} = 0.5774 \frac{\Delta H_{subl}}{N_A a^2} \tag{A.22}$$

A.5 General Expression for Specific Surface Energy of a Truncated Octahedron-shaped Particle Valid for $N/3 \geq 1$

To form a complete truncated octahedron from a cube, we must have N be a multiple of 3.

Let $m = N/3$

Number of atoms on the $\{111\}$ hexagonal faces of a truncated-octahedron = $3m^2 - 3m + 1$

Number of atoms on the $\{100\}$ square faces of a truncated-octahedron = $(m-1)^2$

Number of atoms per edge = $(m-1)$

Number of atoms at the corners = 24

For a truncated-octahedron, there are 6 square faces, 8 hexagonal faces, 36 edges, and 24 corners.

Energy of unsatisfied bonds

$$\begin{aligned} &= 8(3m^2 - 3m + 1) \times 3\varepsilon + 6(m-1)^2 \times 4\varepsilon + 36(m-1) \times 5\varepsilon + 24 \times 6\varepsilon \\ &= \left\{72m^2 - 72m + 24 + 24m^2 - 48m + 24 + 180m - 180 + 144\right\}\varepsilon \\ &= \left\{96m^2 + 60m + 12\right\}\varepsilon \\ &= \left\{32 \times \frac{N^2}{3} + 60 \times \frac{N}{3} + 12\right\}\varepsilon \\ &= \left\{\frac{32}{3}N^2 + 20N + 12\right\}\varepsilon \end{aligned} \tag{A.23}$$

Surface area of each square = $\frac{m^2 a^2}{2} = \frac{N^2 a^2}{18}$ (A.24)

Surface area of each hexagon = $\frac{3\sqrt{3}}{4}(ma)^2 = \frac{\sqrt{3}}{12} N^2 a^2$ (A.25)

Total surface area

$$= 6 \times \frac{N^2 a^2}{18} + 8 \times \frac{\sqrt{3}}{12} N^2 a^2$$
$$= \frac{N^2 a^2}{3} + \frac{2\sqrt{3}}{3} N^2 a^2 \qquad \text{(A.26)}$$
$$= \left(\frac{1 + 2\sqrt{3}}{3} \right) N^2 a^2$$

Specific surface energy is given by

$$\gamma(N) = \frac{\varepsilon}{a^2} \left\{ \frac{32N^2 + 60N + 36}{\left(1 + 2\sqrt{3}\right) N^2} \right\} \qquad \text{(A.27)}$$

$$= \frac{4\varepsilon}{\left(1 + 2\sqrt{3}\right) a^2} \left\{ 8 + \frac{15}{N} + \frac{9}{N^2} \right\} = \frac{8\Delta H_{subl}}{3\left(1 + 2\sqrt{3}\right) N_A a^2} \left\{ 1 + \frac{15}{8N} + \frac{9}{8N^2} \right\} \qquad \text{(A.28)}$$

As $$N \to \infty, \gamma(N) \to \frac{8\Delta H_{subl}}{3\left(1 + 2\sqrt{3}\right) N_A a^2} = 0.5974 \frac{\Delta H_{subl}}{N_A a^2} \qquad \text{(A.29)}$$

Table A.1: Dependence of specific surface energy with the equivalent particle size for a cube-shaped particle in f.c.c

N	N_{cube}	$V = N^3a^3$	$S = 6N^2a^2$	**Equivalent Radius**	**γ(N) in terms of $\frac{\Delta H_{subl}}{N_A a^2}$**
1	14	a^3	$6a^2$	**0.62 a**	**1.33**
2	63	8 a^3	24 a^2	**1.24 a**	**0.958**
3	172	27 a^3	54 a^2	**1.86 a**	**0.852**
4	365	64 a^3	96 a^2	**2.48 a**	**0.802**
5	666	125 a^3	150 a^2	**3.1 a**	**0.773**
6	1099	216 a^3	216 a^2	**3.72 a**	**0.755**
7	1688	343 a^3	294 a^2	**4.34 a**	**0.741**
8	2457	512 a^3	384 a^2	**4.96 a**	**0.732**
9	3430	729 a^3	486 a^2	**5.58 a**	**0.724**
10	4631	1000 a^3	600 a^2	**6.2 a**	**0.718**
11	6084	1331 a^3	726 a^2	**6.83 a**	**0.713**
12	7813	1728 a^3	864 a^2	**7.45 a**	**0.71**
13	9842	2197 a^3	1014 a^2	**8.07 a**	**0.706**
14	12195	2744 a^3	1176 a^2	**8.69 a**	**0.703**
15	14896	3375 a^3	1350 a^2	**9.31 a**	**0.701**
16	17969	4096 a^3	1536 a^2	**9.93 a**	**0.699**
17	21438	4913 a^3	1734 a^2	**10.55 a**	**0.697**
18	25327	5832 a^3	1944 a^2	**11.17 a**	**0.695**
19	29660	6859 a^3	2166 a^2	**11.79 a**	**0.693**
20	34461	8000 a^3	2400 a^2	**12.41 a**	**0.692**
50	515151	125000 a^3	15000 a^2	**31.02 a**	**0.677**
100	4060301	1000000 a^3	60000 a^2	**62.05 a**	**0.672**
∞					

Table A.2: Dependence of specific surface energy and energy density with the equivalent particle size for a cubo-octahedron shaped particle in f.c.c

N	$N_{cubo\text{-}octahedron}$	Volume	Surface area	**Equivalent Radius**	**γ(N) in terms of $\frac{\Delta H_{subl}}{N_A a^2}$**
2	55	6.67 a^3	18.93 a^2	**1.17 a**	**1.003793**
4	309	53.33 a^3	75.71 a^2	**2.34 a**	**0.805676**
6	923	180 a^3	170.35a^2	**3.5 a**	**0.745507**
8	2057	426.67 a^3	302.85 a^2	**4.67 a**	**0.716523**
10	3871	833.33 a^3	473.21 a^2	**5.84 a**	**0.699485**
12	6525	1440 a^3	681.42 a^2	**7 a**	**0.688273**
14	10179	2286.67 a^3	927.48 a^2	**8.17 a**	**0.680337**
16	14993	3413.33 a^3	1211.41 a^2	**9.34 a**	**0.674423**
18	21127	4860 a^3	1533.18 a^2	**10.51 a**	**0.669848**
20	28741	6666.67 a^3	1892.82 a^2	**11.68a**	**0.666202**
50	429351	104166.7 a^3	11830.13 a^2	**29.19 a**	**0.646739**
100	3383701	833333.3 a^3	47320.51 a^2	**58.39 a**	**0.640335**
∞					

Table A.3: Dependence of specific surface energy with the equivalent particle size for a tetrahedron-shaped particle in f.c.c

N	$N_{tetrahedron}$	Volume	Surface Area	**Equivalent Radius**	**γ(N) in terms of $\frac{\Delta H_{subl}}{N_A a^2}$**
1	10	0.33 a^3	3.464 a^2	**0.6828 a**	**1.732**
2	35	2.67 a^3	13.86 a^2	**1.3656 a**	**1.082**
3	96	9 a^3	31.177 a^2	**2.0484 a**	**0.898**
4	217	21.33 a^3	55.426 a^2	**2.7312 a**	**0.811**
5	422	41.67 a^3	86.603 a^2	**3.414 a**	**0.762**
6	735	72 a^3	124.71 a^2	**4.0968 a**	**0.729**
7	1180	114.33 a^3	169.74 a^2	**4.7796 a**	**0.706**
8	1781	170.67 a^3	221.70 a^2	**5.4624 a**	**0.690**
9	2562	243 a^3	280.59 a^2	**6.1452 a**	**0.677**
10	3547	333.33 a^3	346.41 a^2	**6.828 a**	**0.666**
11	4760	443.67 a^3	419.16 a^2	**7.5108 a**	**0.658**
12	6225	576 a^3	498.83 a^2	**8.1936 a**	**0.651**
13	7966	732.33 a^3	585.43 a^2	**8.8764 a**	**0.645**
14	10007	914.67 a^3	678.96 a^2	**9.5592 a**	**0.640**
15	12372	1125 a^3	779.42 a^2	**10.242 a**	**0.636**
16	15085	1365.33 a^3	886.81 a^2	**10.9248 a**	**0.632**
17	18170	1637.67 a^3	1001.1 a^2	**11.6076 a**	**0.629**
18	21651	1944 a^3	1122.4 a^2	**12.2904 a**	**0.626**
19	25552	2286.33 a^3	1250.5 a^2	**12.9732 a**	**0.623**
20	29897	2666.67 a^3	1385.6 a^2	**13.656 a**	**0.621**
50	485747	41666.67 a^3	8660.3 a^2	**34.14 a**	**0.594**
100	3941497	333333.3 a^3	34641 a^2	**68.28 a**	**0.586**
∞					

Table A.4: Dependence of specific surface energy with the equivalent particle size for an octahedron-shaped particle in f.c.c

N	$N_{octahedron}$	Volume	Surface Area	**Equivalent Radius**	**γ(N) in terms of $\frac{\Delta H_{subl}}{N_A a^2}$**
1	6	0.166667 a^3	1.732051 a^2	**0.492377 a**	**2.3094**
2	19	1.333333 a^3	6.928203 a^2	**0.984755 a**	**1.05848**
3	44	4.5 a^3	15.58846 a^2	**1.477132 a**	**0.81257**
4	85	10.66667 a^3	27.71281 a^2	**1.969509 a**	**0.72169**
5	146	20.83333 a^3	43.30127 a^2	**2.461887 a**	**0.67742**
6	231	36 a^3	62.35383 a^2	**2.954264 a**	**0.65219**
7	344	57.16667 a^3	84.87049 a^2	**3.446641 a**	**0.63626**
8	489	85.33333 a^3	110.8513 a^2	**3.939019 a**	**0.62546**
9	670	121.5 a^3	140.2961 a^2	**4.431396 a**	**0.61774**
10	891	166.6667 a^3	173.2051 a^2	**4.923774 a**	**0.61199**
11	1156	221.8333 a^3	209.5781 a^2	**5.416151 a**	**0.60757**
12	1469	288 a^3	249.4153 a^2	**5.908528 a**	**0.60408**
13	1834	366.1667 a^3	292.7166 a^2	**6.400906 a**	**0.60126**
14	2255	457.3333 a^3	339.482 a^2	**6.893283 a**	**0.59895**
15	2736	562.5 a^3	389.7114 a^2	**7.38566 a**	**0.59702**
16	3281	682.666 a^3	443.405 a^2	**7.878038 a**	**0.59539**
17	3894	818.8333 a^3	500.5627 a^2	**8.370415 a**	**0.594**
18	4579	972 a^3	561.1845 a^2	**8.862792 a**	**0.59279**
19	5340	1143.167 a^3	625.2703 a^2	**9.35517 a**	**0.59174**
20	6181	1333.333 a^3	692.8203 a^2	**9.847547 a**	**0.59082**
50	88451	20833.33 a^3	4330.127 a^2	**24.61887 a**	**0.58182**
100	686901	16666.7 a^3	17320.51 a^2	**49.23774 a**	**0.57943**
∞					

Table A.5: Dependence of specific surface energy with the equivalent particle size for a truncated octahedron-shaped particle in f.c.c

N	$N_{truncated\ octahedron}$	Volume	Surface Area	**Equivalent Radius**	**γ(N) in terms of $\frac{\Delta H_{subl}}{N_A a^2}$**
3	38	4	13.3923	**4.1778 a**	**1.04538**
6	201	32	53.56922	**8.3556 a**	**0.8027**
9	586	108	120.5307	**12.5334 a**	**0.7301**
12	1289	256	214.2769	**16.7112 a**	**0.69536**
15	2406	500	334.8076	**20.889 a**	**0.67501**
18	4033	864	482.123	**25.0668 a**	**0.66166**
21	6266	1372	656.2229	**29.2446 a**	**0.65222**
24	9201	2048	857.1075	**33.4224 a**	**0.64519**
27	12934	2916	1084.777	**37.6002 a**	**0.63976**
30	17561	4000	1339.23	**41.778 a**	**0.63544**
33	23178	5324	1620.469	**45.9558 a**	**0.63192**
36	29881	6912	1928.492	**50.1336 a**	**0.62899**
39	37766	8788	2263.3	**54.3114 a**	**0.62652**
42	46929	10976	2624.892	**58.4892 a**	**0.62441**
45	57466	13500	3013.269	**62.667 a**	**0.62258**
48	69473	16384	3428.43	**66.8448 a**	**0.62098**
51	83046	19652	3870.376	**71.0226 a**	**0.61958**
99	591526	143748	14584.22	**137.8674 a**	**0.6084**
∞					